

SOL-GEL DERIVED SILICA OPTICS

By
SHI-HO WANG

A DISSERTATION PRESENTED TO THE GRADUATE SCHOOL
OF THE UNIVERSITY OF FLORIDA IN PARTIAL FULFILLMENT
OF THE REQUIREMENTS FOR THE DEGREE OF
DOCTOR OF PHILOSOPHY

UNIVERSITY OF FLORIDA

1988

ACKNOWLEDGMENTS

I am deeply honored to acknowledge several persons who have helped me during the time of my research as a graduate student at the University of Florida and as a scientist at GelTech Inc., Alachua, Florida.

I am grateful to my advisor Professor Larry L. Hench who has shared my dream of creating a new method for manufacturing high-tech silica optical monoliths, including high power glass lasers for nuclear fusion which might contribute to freeing mankind from energy and pollution crises. This dream has been partially realized by this research and I greatly appreciate his guidance and support.

Dennis A. LeSage, Candace E. Campbell, and Grib Murphy of GelTech Inc., and Dr. Jon West, Guy LaTorre, and Martin Wilson of the Advanced Materials Research Center of University of Florida assisted me directly or indirectly in this work. I give each of them, my friends, sincere thanks. My appreciation is also extended to Linton E. Floyd, III, and the Glass Fab Inc. for arranging and performing the gel-silica optical property proving tests, and to Professor Stephen F. Jacobs in Optical Sciences Center of the University of Arizona for the low temperature gel-silica thermal expansion test.

Financial support from the U.S Air Force Office of Scientific Research through contract no. F49620-83-0072, GelTech Inc. and the Department of Materials Science and Engineering were very important to me and made the research and this manuscript possible. I am grateful to Dr. Donald R. Ulrich of the AFOSR for his understanding and contributions to my success.

Special thanks are given to Professor Gholamreza J. Abbaschian, Chairman of the Department of Materials Science and Engineering, and Professor John Staudhammer of the Department of Electrical Engineering for their unforgettable assistance and encouragement at a very critical moment in September 1987.

I greatly appreciate the members of my supervisory committee, Professors Vellayan Ramaswamy of the Department of Electrical Engineering, Joseph H. Simmons,

David E. Clark and Gholamreza J. Abbaschian of the Department of Materials Science and Engineering for their advice and recommendations regarding this dissertation. The responsibility for any remaining errors or shortcomings is, of course, mine.

Words are insufficient to express gratitude to my parents for their constant support and to my brothers and sisters for their consideration in Taiwan. I am also particularly indebted to my wife, Sue-Ling, not only for her great backup but also for her scientific discussions, and to my daughter, Jean, for understanding why we couldn't have much fun together while this work was being finished.

TABLE OF CONTENTS

	<u>Page</u>
ACKNOWLEDGMENTS	ii
ABSTRACT	vi
CHAPTERS	
1 INTRODUCTION TO SOL-GEL DERIVED SILICA GLASS TECHNOLOGY	1
2 SOL-GEL TRANSFORMATION AND EXPERIMENTAL PROCEDURES	12
Introduction	12
Literature Review of Sol-Gel Transformation Modeling	12
Experimental Procedure	48
Results	57
Conclusions	64
3 PHYSICAL PROPERTIES OF PARTIALLY DENSIFIED SILICA XEROGEL	67
Introduction	67
Review of the Literature	68
Experimental Procedure	73
Results and Discussions	81
Conclusions	126
4 DEHYDRATION OF SOL-GEL DERIVED SILICA OPTICS	128
Introduction	128
Review of the Literature Regarding Dehydration	130
Experimental Procedure	139
Results and Discussions	145
Conclusions	157
5 OPTICAL PROPERTIES OF FULLY DEHYDRATED SILICA GEL GLASS	160
Introduction	160
Literature Review Regarding Optical Properties of Silica Glass	161
Experimental Procedure	178
Results and Discussions	185
Conclusions	203
6 SILICA GEL OPTICAL FILTERS USING TRANSITION-METAL COMPOUNDS	206
Introduction	206
Review of the Literature	207

Experimental Procedure	229
Results and Discussions	230
Conclusions	238
7 CONCLUSIONS AND RECOMMENDATIONS	239
REFERENCES	244
BIOGRAPHICAL SKETCH	252

Abstract of Dissertation Presented to the Graduate School
of the University of Florida in Partial Fulfillment of the
Requirements for the Degree of Doctor of Philosophy

SOL-GEL DERIVED SILICA OPTICS

By

SHI-HO WANG

April 1988

Chairman: Dr. Larry L. Hench
Major Department: Materials Science and Engineering

Large monolithic xerogel silica glasses were successfully made from tetramethyl-orthosilicate and distilled water using the combination of an acidic drying control chemical additive (DCCA) and a specially designed drying chamber. The acidic DCCA increases the gel strength by formation of a fibrillar ultrastructure, and the drying chamber reduces the catastrophic capillary forces inside the wet gel body.

Partially densified monolithic gels up to 850°C were routinely made for physical property tests and compared to commercial fused silicas. Although the mechanical properties of the porous gel-silica monoliths such as microhardness, Young's modulus, toughness, flexural strength, density are relatively lower than fused silica, the optically transparent porous gel silica has a uv cut-off ranging from 250-300 nm. Such a porous gel with excellent optical transmission and a highly uniform pore radius of 10-50 Å offers a unique, chemically stable matrix for impregnation with a second phase of optically active organic or inorganic compounds.

The processing and properties of Types I and II fused quartz optics and Types III and IV synthetic fused silica optics are compared with the new organometallic sol-gel

derived gel-silica optics. Fully dehydrated and densified gel-silica has excellent transmission from 165 nm to 4400 nm with no OH absorption peaks. This optical transmission is equivalent to the best type IV fused silica. The other physical properties and structural characteristics of the dehydrated dense gel-silica are similar to fused quartz and fused silica. However, the dense gel-silica has a lower coefficient of thermal expansion of 2.0×10^{-7} cm/cm compared with 5.5×10^{-7} cm/cm for standard vitreous silicas. The CTE value is temperature independent from 80 K to 500 K. Sol-gel silica optics can be made as complex shapes by casting of the sol into inexpensive plastic molds.

Monolithic silica gel optical filters were produced by chemical doping with various transition-metal ions (e.g., cobalt, copper, nickel). Color changes occurred with various sintering temperature indicating a unique method to control light wavelength filtration in the visible range. For instance, the observed color or spectral (major peak of absorption) shifts for the 160°C, the 850°C, and the 900°C Co^{II} ion doped gels were reddish pink (505 nm), deep blue (660 nm), and greenish black (670 nm) respectively. The optical absorption spectra of the chemically doped-silica are interpreted in terms of ligand-field and molecular orbital theories.

CHAPTER 1 INTRODUCTION TO SOL-GEL DERIVED SILICA GLASS TECHNOLOGY

One of the world's most pervasive chemical compounds is silicon dioxide (SiO_2). This compound can exist in many forms — crystalline or amorphous, hydroxylated or dehydroxylated — but is most often called "silica" as a generic name.

Silica-based compounds have been fabricated and utilized by mankind for tens of thousands of years, although only in the past few decades have significant strides been made in understanding the variables that control silica chemistry [1-7].

Application of this knowledge has produced many useful materials worth billions of dollars per year; however, today's rapidly accelerating technology demands even greater performance of silicate materials as well as the need to create new materials. The objective of this study is to produce a number of new materials using sol-gel silica processing, including (1) ultraporous gel monoliths for optical and chemical matrices, (2) ultrapure monolithic gel-glasses with ultralow optical absorption, and (3) chemically doped gel glass monoliths for optical filters with low expansion coefficients and high softening points.

Traditional silica glasses are manufactured by melting natural quartz minerals or synthetic silica, or by flame or plasma vapor-deposition methods. Generally, four types of commercial vitreous silica are recognized and identified: Type I is obtained by electric melting of natural quartz in vacuum. Type II is made by flame fusion of quartz. Type III is made by vapor-phase hydrolysis of pure silicon tetrachloride carried out in a flame. Type IV is made by oxidation of pure silicon tetrachloride which is subsequently fused electrically or by means of a plasma. Types I and II are called fused quartz, whereas Types III and IV are called synthetic fused silica.

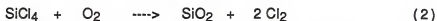
Fused quartz is melted at temperatures above its liquidus (1713°C) from crushed natural crystalline quartz powders of mixed particle size, well above micrometers in diameter [8]. The initial size of these particles, millions of times larger than a silica molecule, limits the control over the resulting structure and in part determines the temperature necessary for melting, homogenization, and fabrication. Glass products from this method have numerous deficiencies; impurities, inhomogeneities, seeds and bubbles, a high energy requirement for raw material crushing, melting and homogenization, as well as premature phase separation and crystallization.

Chemical reactions used to produce synthetic fused silica by flame hydrolysis of silica tetrachloride (type III) and by vacuum plasma oxidation of silica tetrachloride (type IV) are shown in equations #1 and #2:

Type III (hydrolysis)



Type IV (oxidation)



In fact, it is very difficult to have a complete reaction for either of these two equations. Consequently, water contents of several thousand ppm are present in type III silicas, and SiCl_4 in few hundred ppm is retained as an unreacted residual in both type III and IV silicas. In addition to these two intrinsic impurities, the resultant glasses from type III and IV processes have extrinsic impurities in the range of few parts per million (ppm) due to the contamination of raw materials and crucibles at high temperatures (about 1900°C).

Table 1-1 [9] lists the dominant characteristics of commercial brands of silica corresponding to these four types. Their transmission curves are summarized in Figure 1-1 and Table 1-2 [10]. Type I and II glasses have more impurities (Table 1-1) which make uv transmission curves cut off at higher wavelengths (curves 2 and 3 in Fig. 1-1) than that of type III and IV glasses (curve 1 in Fig. 1-1). The amount of water (Table 1-

Table 1-1
Preparation and characteristics of four types of vitreous silica

Type	I	II	III	IV
Process	Electromelted Quartz	Flame-fused Quartz	Hydrolyzed SiCl ₄	Oxidized SiCl ₄
Example	IR-Vitreosil ^a Infrasil ^b	Herasil ^b Homosil ^b	7940 ^c Dynasil ^d Spectrosil ^a Suprasil ^b	Spectrosil W ^a 7943 ^c Suprasil-W ^b

Impurity (ppm):

OH	<5	400-1500	~1000	~0(<0.4)
Al	30-100	<1	<0.2	<0.2
Sb	<0.3	<0.1	<0.1	<0.1
As	0	0	<0.02	<0.02
B	4	3	0.1	0.1
Ca	16	0.4	<0.1	<0.1
Cl	0	0	100	up to 200
Cr	0.1	0	0.03	0.03
Co	0	0	0.0001	0.0001
Cu	1	1	<1	<1
Ga	0	0	<0.02	<0.02
Au	0	0	<0.1	<0.1
Fe	7	1.5	<0.2	<0.2
Li	7	1	0	0
Mg	4	0	0	0
Mn	1	0.2	<0.02	<0.02
Hg	0	0	<0.1	<0.1
P	0.01	0.005	<0.001	<0.001
K	6	<1	0.1	0.1
Na	9	5	<0.1	<0.1
Ti	3	2	0	0
U	0	0.0006	0	0
Zn	0	0	<0.1	<0.1
Zr	3	0	0	0

a: Thermal Syndicate, England.

b: Heraeus Amersil, Heraeus, Sayreville, NJ.

c: Corning Glass Work, Corning, NY.

d: Dynasil; Berlin, NJ.

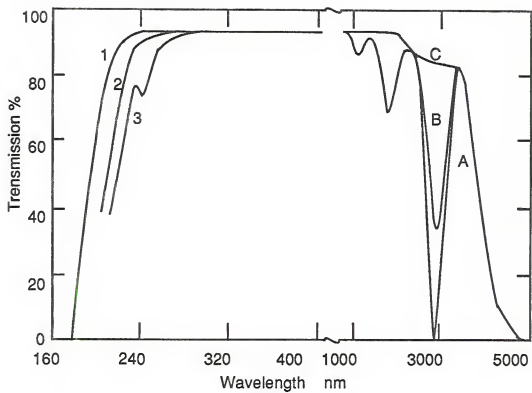


Figure 1-1 Transmission curves for commercial vitreous silica
10mm thick

Table 1-2
Identification of transmission curves of silica glasses

Manufacturer	Product name	Type	UV curve in Fig. 1-1	IR curve in Fig. 1-1
Amersil, Inc. (Heraeus)	Herasil	II	3	B
	Infrasil	I	2	C
	Homosil	II	3	B
	Suprasil	III	1	A
	Suprasil-W	IV	1	C
Corning Glass Works	Code 7940	III	1	A
	Code 7943	IV	3	C
Dynasil Corp. of America	Dynasil-1000	III	1	A
Thermal Syndicate Ltd.	Spectrosil	III	1	A
	Spectrosil WF	IV	1	C
	IR-vitreosil	I	3	C

1) in silica glass depends on which type of process is used. For example, Spectrosil WF (type IV) in Table 1-1 has a water content less than 0.4 ppm compare to 1200 ppm for Suprasil (type III). It is observed that there is no significant shift in the uv cut off between type III and IV silicas due to the increased water content if the other impurities are constant. However, in the infrared range, water (type III, curve A in Fig. 1-1) noticeably gives a strong absorption. These shortcomings can limit the use of glass products made by the traditional techniques described above, as summarized in Table 1-3.

Sol-gel processing has been used for many years, although the principal chemical and physical mechanisms are still not clearly understood [11-14]. In recent years special applications require silica optical components that meet very stringent requirements. The sol-gel method offers new hope in that structural manipulation is possible on an extremely fine scale, within the nanometer range, thereby allowing production of a new generation of silica materials. The outstanding features of these silicas include very high homogeneity, very high purity, potentially extremely low optical loss, ease of chemical doping, and near net shape casting. These features make sol-gel silicas potentially applicable to a wide range of optical products including lenses, mirrors, waveguides, optical fibers, integrated optoelectronics, and host materials for filters, lasers, and non-linear optical elements or compounds.

The sol-gel process as it relates to silicas is summarized briefly. A sol is defined as a dispersion of colloids in a solvent. Silica colloids are solid particles with diameters ranging from 1nm to 100 nm which depend upon the type and amount of drying control chemical additive (DCCA) in the solution [15-19]. In this study all colloidal particles are synthesized by the hydrolysis of tetramethylorthosilicate (TMOS) $[\text{Si}(\text{OCH}_3)_4]$ followed by the growth of the hydrolyzed species $[\text{Si}(\text{OCH}_3)_{4-n}(\text{OH})_n]$ with $0 \leq n \leq 4$ [14, 20].

Table 1-3
Limits for the four types of silica fabrication processes

Type	Fabrication Limits
Type I & II	<ul style="list-style-type: none"> (1) Bad homogeneity (granular microstructure and bubbles) (2) Noticeable water content -- few tens to hundreds ppm. (3) High impurities -- in the range of few ppm from nature quartz mineral. (4) Micrometer scale structural manipulation -- quartz is ground to few micrometers before sintering. (5) High sintering temperature (above 1700°C) -- <ul style="list-style-type: none"> (a) High energy cost; (b) React with crucible, thus impurities; (c) Possible initiate crystallization.
Type III	<ul style="list-style-type: none"> (1) High water content (above 1000 ppm). (2) High sintering temperature (above 2000°C) -- <ul style="list-style-type: none"> (a) High energy cost; (b) React with crucible, thus impurities; (c) Possible initiate crystallization.
Type IV	<ul style="list-style-type: none"> (1) Detectable water content (around 1 ppm). (2) High sintering temperature (above 2000°C) -- <ul style="list-style-type: none"> (a) High energy cost; (b) React with crucible, thus impurities; (c) Possible initiate crystallization.

This over-saturated sol is never chemically stable in the presence of the DCCA and/or under thermally activated conditions; however, after some time and with the addition of thermal energy a sufficient concentration of colloids that are within an appropriate size distribution is reached and a zero surface charge is obtained [21]. At this point the colloids become randomly linked together in fibrillar chains with thermally activated Brownian motion in the presence of a Van der Waals attractive force and a base catalyst [see p. 224 in ref. 4]. As the chains grow they form three-dimensional irregular structures throughout the liquid phase. A network develops with the liquid phase localized within the solid gel skeleton and microscopically confined by it. The "sol" has lost its freedom of movement and now becomes a "gel"; this is described as the gelation point.

Solids tend to decrease their interfacial area so as to minimize surface energy. Therefore, after the gelation point has been reached the weakly connected spherical-particle chains tend to minimize surface energy by particle rearrangement, thereby forming a strong fibrillar-shaped ultrastructure. This phenomenon continues during the aging process (also termed syneresis), in which liquid is expelled from the gel body and the weak gel shrinks and becomes stronger.

In this study the first goal, described in Chapter 2, is the production of silica-based monolithic dried xerogels composed of (a) pure silica and (b) doped with transition-metal elements. A xerogel is defined as a gel from which the liquid phase has been evacuated under ambient pressures. The net size and porosity of a xerogel is minimized, at least to some degree, by surface energy as the liquid is removed. However, without the help of the DCCA in controlling the colloidal particle size, this can not be realized because of cracking during drying.

In the amorphous form of silica, a tetrahedral arrangement is primarily favored by the radius ratios of the silicon to the oxygen ions and by the bonding of sp^3 hybrid orbitals in SiO_2 . X-ray diffraction studies by Mozzi, Warren and Uhlmann [22, 23]

have shown that silicon forms bonds with oxygen of variable bond angles that are 10% within the 144° maximum in the distribution of Si-O-Si angles. Various arrangements of these SiO_2 tetrahedra are possible in noncrystalline silica gels. Bonding oxygens at the corners of two silica tetrahedra can be easily disconnected in the presence of uneven hydrostatic stresses and water [24]. DCCA's can be used to minimize the particle size within the polymerized chain, thereby improving the strength of the gel structure so that during the critical drying process the gel can endure differential evaporation without initiating cracking.

The processing and physical properties of dried monolithic silica xerogels, heated from 150°C to 900°C , are discussed in Chapter 3. This ultraporous material has densities ranging from 0.7 g/cm^3 to 2.10 g/cm^3 depending on the initial conditions of the sol, such as the variation of DCCA and/or the amount of water used, as well as the aging and drying temperatures.

Two types of water exist within the dried xerogel structure — chemical water and physical water [25], which must be removed to achieve monolithic optical components. Water in solution can hydrolyze the silicon-oxygen-silicon bond. The hydroxyl ion's oxygen is covalently bonded to silicon, whereas the hydrogen ion forms an ionic bond to the oxygen. Consequently, chemical water results with hydroxyl groups strongly attached to the gel's surface. The physical water associated with hydrogen-bonding of surface hydroxyl groups exists within the ultraporous space of the gel body.

A major problem with monolithic silica xerogels, especially for high-transmittance optical components, is the removal of chemically bonded water, also called a silanol group. The chemically bonded silanols give rise to the fundamental vibration of hydroxyl ions occurring at a wavelength of 2669.4 nm . Also present are vibrational overtones and combinations of this ion and associated water occurring at the following wavelengths: 2919.7 nm , 2768.9 nm , 2698.3 nm , 2262.5 nm , 2207.5 nm , 1890.4 nm , 1459.9 nm , 1408.5 nm , 1366.1 nm , 1237.9 nm , 1131.2 nm , 939.0 nm , 704.2

nm. These IR absorptions are the result of electromagnetic vibrational interactions with the electrons, atoms, and molecules of the gel water. Selectively absorbed light energy, such as this, is mostly converted into heat. Consequently it is important to reduce the hydroxyl groups to nondetectable levels in order to minimize absorption loss, especially for optical lenses, optoelectronic signal processors, optical fiber, filters, and laser resonant host systems. Therefore, monitoring the IR absorption peaks is a primary method for determining the degree of dehydration achieved during densification [26, 27].

Consequently, the second goal of this study is to dehydrate and densify monolithic silica xerogels; this is described in Chapter 4. Two methods are investigated: (1) sintering samples in an air atmosphere and (2) chemical treatment and sintering in a controlled gas atmosphere (e.g., carbon tetrachloride). At sufficient temperatures these gases can react with the hydroxyl groups to form hydrogen chloride which escapes freely from the unclosed ultrapores [28]. The dehydrated xerogel samples are then exposed to a higher temperature for full sintering.

The third goal is to determine the physical properties of monolithic fully dehydrated gel-silica glasses. In Chapter 5 various physical properties of the dense gel-silica glasses are compared with commercial melt/cast vitreous silica glasses (fused quartz) and other high-quality optical silica glasses (synthetic fused silica).

The fourth goal of this study is to develop the technology for fabrication of transition-element doped xerogels. This is described in Chapter 6. Optical color filters that selectively transmit part of the visible spectrum can be made from xerogels doped with transition metal compounds. Transition elements, having unpaired electrons in their d-orbitals, can absorb light by ligand field-controlled transitions that do not involve variable valence states. The energy level scheme is controlled by the number and symmetry of the ligands and the strength of the ligand field [29]. The doped xerogels processed at different temperatures exhibit different densities and slight changes in

bonding strength which can produce a dramatic shift in their color response. For example, a 160°C silica xerogel containing 0.25% cobalt is a reddish-orange color, whereas the 850°C sample is a deep blue, and the 900°C sample has a greenish-black color.

Finally, a summary (Chapter 7) is presented which reviews the present state of sol-gel processing science as applied to gel-silica optical monoliths and the properties of these unique materials. Questions still to be answered by future investigations are also included in the summary chapter.

CHAPTER 2 SOL-GEL TRANSFORMATION AND EXPERIMENTAL PROCEDURES

Introduction

During recent years many researchers have attempted to produce large monolithic dried xerogels; however, a reliable process had not yet been established at the time this work began [30-36]. Difficulties associated with this sol-gel processing method arise during all phases of aging, drying, and densification, clearly indicating insufficient understanding of basic changes in the ultrastructure during the sol-gel transformation and in the chemical reactions of the solvents, precursors, and catalysts involved. In general, crack formation during drying is a result of strong hydrostatic stresses within a relatively weak gel structure. Catastrophic failure can be avoided by adjusting the mechanical strength of the gel structure to exceed that of the hydrostatic force and/or by decreasing the hydrostatic stress relative to the gel's strength.

The object of this chapter is to describe the principal mechanisms of the sol-gel method by which monolithic xerogels may be reliably produced. Four factors are used to describe the sol-gel transformation up to the gelation point: (1) the isoelectric point (iep), (2) the point of zero surface charge (pzc), (3) thermally activated particle movement (Brownian motion), and (4) Van der Waals force. Three kinds of dried monolithic gel samples were routinely prepared to aid in this study: pure silica, silica doped with transition elements, and silica doped with rare earth elements.

Literature Review of Sol-Gel Transformation Modeling

Dr. Ralph K. Iler's pioneering work in the investigation of silica chemistry is the foundation of many of the ideas discussed in this chapter. Iler found that silica gels can be

obtained from supersaturated aqueous solutions produced by one of the following methods:

- (i) Concentrating an unsaturated silica solution by evaporating its solvent.
- (ii) Cooling a hot saturated silica solution.
- (iii) Lowering the pH of an aqueous solution of a soluble silicate below 10.7.
- (iv) Hydrolyzing $\text{Si}(\text{OR})_4$ -- (where R is CH_3 , C_2H_5 , or C_3H_7).

In this study all of the monomers were produced by chemically hydrolyzing tetramethylorthosilicate (TMOS), as indicated in method (iv). The amount of monomer generated within a given period of time depends on temperature and the relative amounts of DCCA, water, and TMOS. When a solution of monomer, $\text{Si}(\text{OH})_4$, is formed at a concentration greater than the solubility of the solid phase of amorphous gel silica in water, and in the absence of a solid phase on which the soluble silica might be deposited, the monomers then polymerize by condensation to form dimers (two silicons), then tetramers (four silicons), then particles (eight or more silicons). For most alkoxide syntheses, a polymerization reaction occurs before hydrolysis is completed (as evidenced by ^{29}Si NMR studies [37, 38]). As shown in Figures 2-1 and 2-2, the particle's size at any moment of growth is controlled by the Ostwald ripening mechanism [see p. 175-220 in ref. 4] and essentially is determined by the pH of the DCCA/silicic acid solution.

Vysotskii and Strazhesko [39] describe that in the presence of a given acid, the growth of monomers is governed by the chemical equilibrium kinetics of the sol and is minimized at the isoelectric point (iep). This implies that the monomers grow to some certain size before the solution reaches its own iep. The iep occurs when the net electrical mobility of surface ions on the silica particles is zero and at a pH at which there is no charge outside the hydroelectric slip plane (outside this plane the liquid is free to move, inside the plane the liquid molecules are held too tightly to move) [see p.

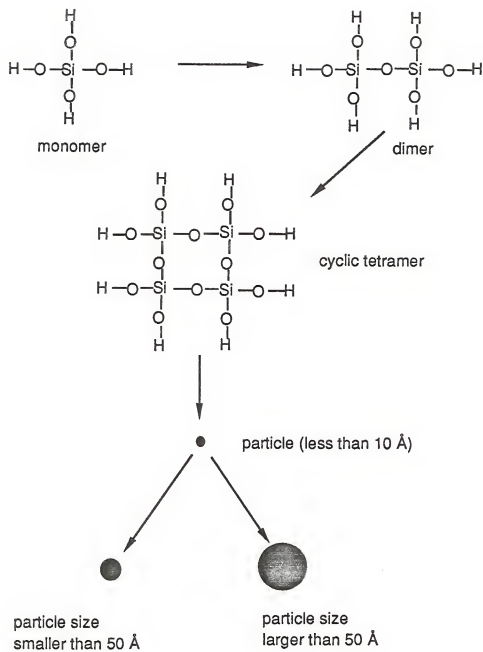


Figure 2-1 Particle growth in solution

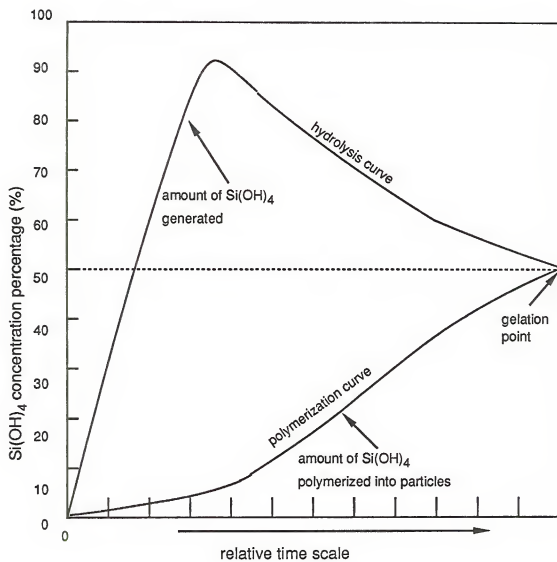


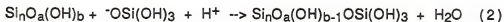
Figure 2-2 Polymerization reaction occurs before hydrolysis is completed

660 in ref. 4]. Below are equations related to particle growth under two different pH conditions, and will be described as two models in the following paragraph.

$0 < \text{pH} < 2$, $[\text{H}^+]$ as a catalyst



$2 < \text{pH} < 7$, $[\text{OH}^-]$ as a catalyst



$\text{Si}_n\text{O}_a(\text{OH})_b$ is a surface hydrolyzed silica particle, where "n" can be 2, 4, 8, 40, 311, 1438, etc. [see p. 8 in ref. 4]. The number of anhydrous oxygens within a particle is represented by "a"; "b" is the number of surface hydroxyl groups per particle.

In an extensive study of silica polymerization, Linsen, Okkerse, Vysotskii and Strazhesko [39, 40], found the iep to be between pH of 1.0 and 2.0. Condensation is slowest in this pH range, thereby producing a minimum gelation rate. Gelation occurring at the iep results in gel structures of maximum specific surface area and maximum strength. These structures occur because the rate of aggregation is minimal as is the growth rate of the ultimate particles from the monomer. Consequently, the ultimate particles are smallest when the gel is formed at the iep.

Strong Acid Model

Figure 2-3 represents experimental data of relative gelation time versus solution acidity found by many researchers [39, 41, 42]; the corresponding relative surface area curve is shown in Figure 2-4. These two figures show that the longest gelation time results in the highest surface area when the solution was prepared at pH=2. This is because the rate of polymerization reaction depends on a catalytic effect which is at a minimum at pH=2. From these data a model is developed describing the gelation phenomenon in a strongly acidic solution, in which the pH is less than 2.0.

The very high hydrogen ion concentration at pH<2.0 results in a rapid reaction among monomers to form dimers, cyclic tetramers, and very small particles, producing

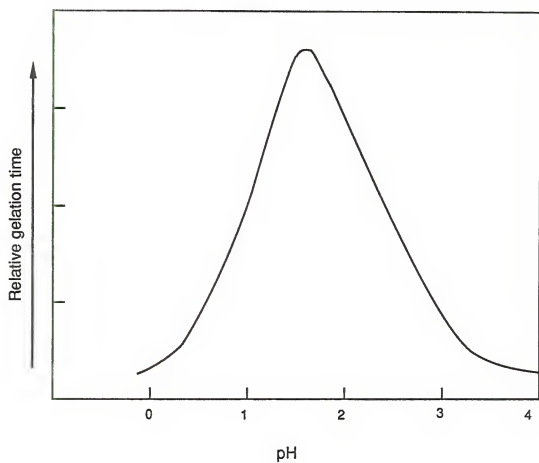


Figure 2-3 Relative gelation time versus solution acidity

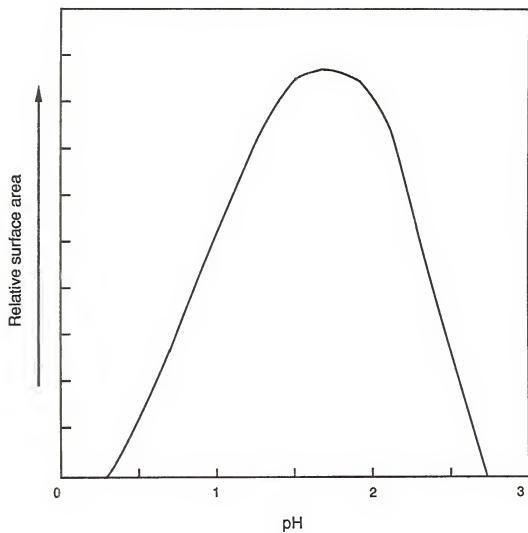


Figure 2-4 Relative surface area versus solution acidity

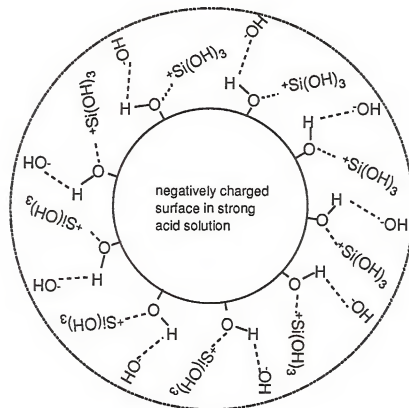
a significant amount of free water (equation #1) which dynamically reduces the hydrogen ion concentration. This dilution slows the reaction between monomer and the particle surface causing a build up of monomers around the particle while the total hydrogen concentration in solution is reduced. This causes the pH to be increased to the isoelectric point with a pH approximately equal to 2.0. This implies that the stronger initial acidic solution ($\text{pH} < 2$) allows the monomers to grow to relatively larger particles before the iep is achieved and results in a relatively smaller surface area, as measured. As soon as the iep is reached, the particle size is nearly determined, the slip plane of the electrical double layer is formed, no electric charge outside the slipping plane can be measured, and particles are then homogeneously distributed in the solution.

As shown in Figure 2-5, the particle surface has a slight negative charge in the presence of the positively charged monomer (equation #1). The monomers confined within the slip plane of the electrical double layer [see p. 358-378 in ref. 4] will gradually react with the particle surface under the influence of the hydrogen ion concentration and thermal energy, resulting in slight particle growth. Free water is released, diluting the hydrogen ion concentration while particle growth decreases. As the confined monomers are consumed, the electrical double layer and slip plane is eliminated. Formation of an electrically neutral particle surface, referred to as the point of zero surface charge (pzc), at $\text{pH} \approx 2.5$ [41] marks the beginning of gelation under the influence of thermally activated Brownian motion and Van der Waals attractive force from this strongly acidic sol.

Weak Acid Model

The mechanism for gelation in a weaker acid solution ($\text{pH} 2.0 - \text{pH} 7.0$) is somewhat different from that of a strong acid solution, as shown in Figure 2-6. The reduction in hydrogen ion concentration effectively weakens its strength as an acid catalyst preventing the hydrogen ion from attracting the hydroxyl group from the

monomers expose their positively charged electric cloud toward particle surface.



electrical double layer

Figure 2-5 Particles in strong acidic solution, $\text{pH} < \text{iep}$ (~ 2.0).

particles surface exposes positively charged electric cloud toward negatively charged monomer in the weak acid solution.

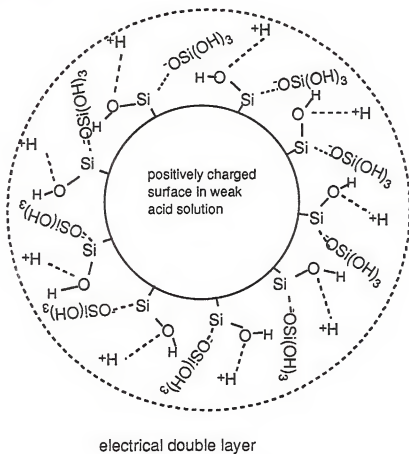


Figure 2-6 Particles in weak acidic solution. $\text{pH} > \text{iep}$ ($\text{pH} 2.0 - \text{pH} 7.0$).

monomers around the particle and exposing the negatively charged $^{-}\text{OSi}(\text{OH})_3$ molecules (equation #2) which can react with the particle's positively charged surface. Rather, the negatively charged oxygen of the hydroxyl ions in solution can attract a hydrogen from the monomer. This forms free water and leaves the negatively charged oxygen as a site now available to react with the positively charged silicon on the particle surface, thereby regenerating this basic catalyst as a hydroxyl ion is released. With the production of free water, the hydroxyl concentration is reduced, decreasing the pH as well as the hydroxyl ion's ability to act as catalyst which causes a build-up of monomers surrounding the particle surface. As the concentration of these monomers within the slip plane reaches a maximum, at about $\text{pH} = 2.0$, the isoelectric point (iep) is attained. At this pH the hydrogen ion acts as a catalyst promoting the reaction between the monomers and the surface hydroxyl groups which facilitates particle growth. Free water is a by-product of this reaction, reducing the hydrogen ion concentration and increasing the pH. This process continues until the monomer concentration inside the slip plane is exhausted and the electrical double layer eliminated. Thus, the point of zero surface charge (pzc) has been reached and gelation begins under the influences of thermally activated Brownian motion and Van der Waals attractive force.

Brownian Motion, Van der Waals, and Interparticle Bonding Models

When monomers come together to form very small ($10 \text{ \AA} - 50 \text{ \AA}$) [43], uniform, uncharged (pzc) particles, their motion is essentially governed by thermal diffusion as described by the diffusion equation below.

$$D = KT/(3\pi \eta d) \quad (3)$$

where

D is the diffusion coefficient

η is viscosity

d is the effective instantaneous diameter of the polymerized cluster

K is Boltzmann's constant

T is absolute temperature

The average displacement X of a particle from time zero (@ pzc) to any point in time t is:

$$X = (2Dt)^{1/2} \quad (4)$$

Prior to reaching the pzc, the viscosity of the sol increases only slightly, as shown in Figure 2-7 [44]. At the point (pzc) is achieved the small particles are homogeneously distributed throughout the solvent, as shown in Figure 2-8. Governed by Brownian motion (equation #4), these thermally activated, hydroxyl ion-catalyzed particles randomly collide under the aid of Van der Waals attractive forces and a base catalyst, as shown in Figure 2-9, to form long spherical-particle chains. As these chains continue to form, the viscosity increases until there exists a three dimensional network throughout the volume of the sol, as shown in Figure 2-10. This is described as the gelation point. A sol takes a specific time to reach its own gelation point.

Gelation time is then defined as at the moment the sol is prepared to the moment the sol loses its freedom to move. The length of gelation time is a function of the temperature and the relative amounts of acidic DCCA, water, and TMOS in a sol. Figures 2-11, 2-12, 2-13, and 2-14 show that the gelation time can be exponential curve fitted with one of the four variables (i.e. temperature, oxalic acid (DCCA), water, and TMOS) in which the other three are kept constants. Increasing the sol temperature promotes the thermally activated Brownian motion and thus decreases the gelation time as shown in Figure 2-11. A decreased amount of oxalic acid concentration weakens the catalytic effect among particles and therefore increases the gelation time as shown in Figure 2-12. An increased TMOS content in water results in an increased concentration of particles and a decreased distance between particles, which consequently, shortens the gelation time as shown in Figures 2-13 and 2-14.

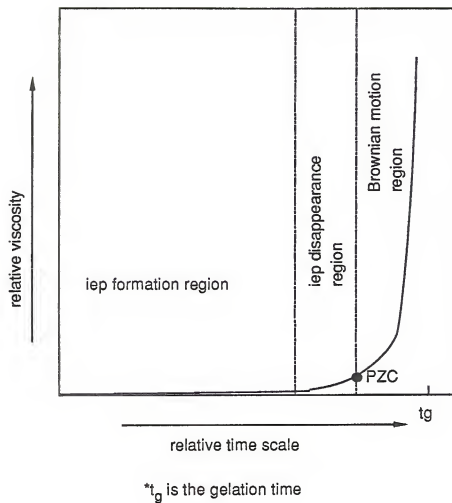


Figure 2-7 Relative viscosity versus time

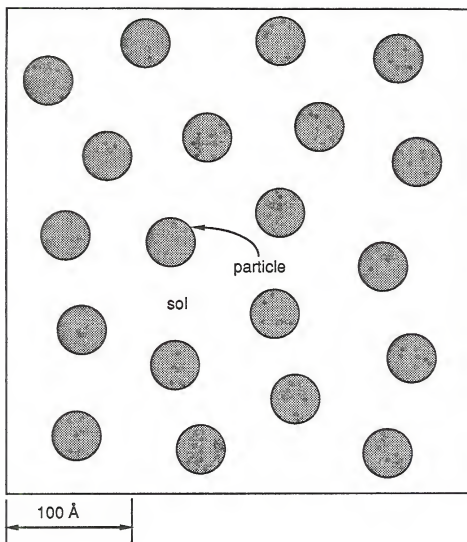


Figure 2-8 Homogeneous particle distribution throughout the solvent.

(a) Brownian motion and Van der Waals forces

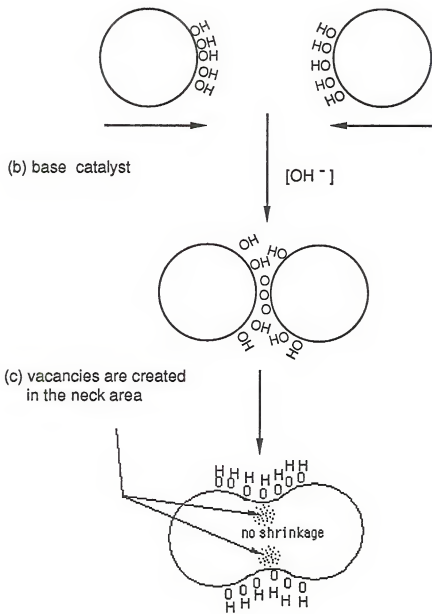


Figure 2-9 Particles collide randomly with the help of Van der Waals attractive forces, Brownian motion and base catalyst.

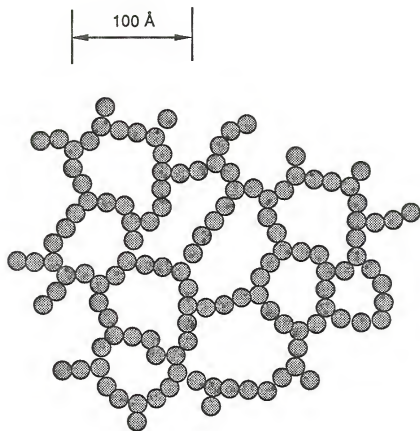


Figure 2-10 Acid catalyzed particles constitute fibrillar chains throughout the volume of sol.

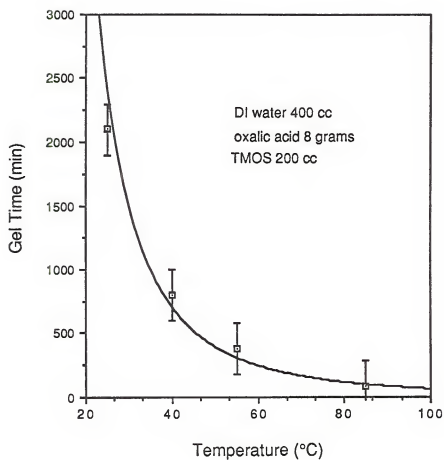


Figure 2-11 Gelation time versus temperature.

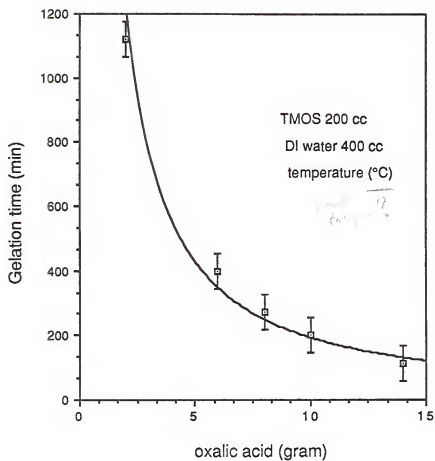


Figure 2-12 Gelation time versus oxalic acid content.

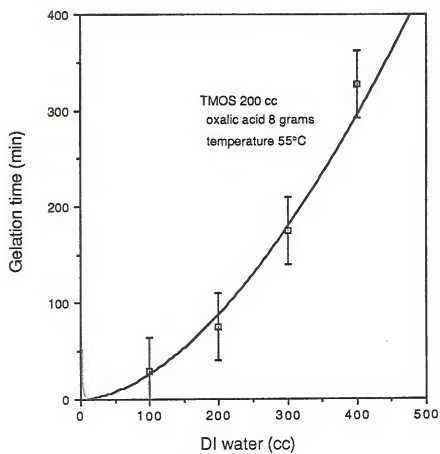


Figure 2-13 Gelation time versus water content.

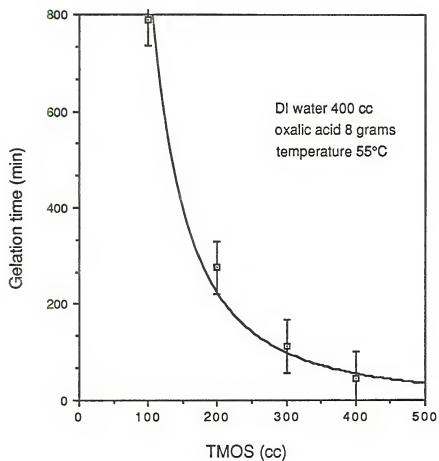


Figure 2-14 Gelation time versus TMOS content.

Characterization of Gelation

Professor Paul Flory's theory of gel formation [45, 46], with which Iler agrees [see p. 176 in ref. 4], notes that the silica monomer has four polymerization functional groups ($f=4$). The degree of polymerization (DP) obtainable in a system is therefore described by the equation:

$$DP = 1/(1-pf/2) \quad (5)$$

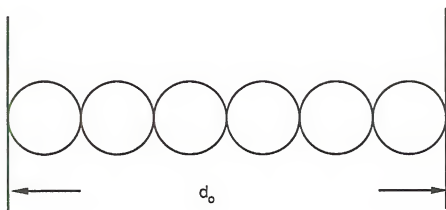
in which "p" is the percentage of reacting monomers (that is the fraction of the total concentration of monomer which is the reaction product from TMOS) and "f" is the number of polymerization functional groups. At the gelation point the degree of polymerization approaches infinity, therefore $(1-pf/2)$ must equal zero. For $f=4$ the percentage of total concentration of monomer going into gel phase must equal 50%. Since equal amounts of monomer exist in the liquid as well as in the gel, no refractive index change is observed at the gelation point. Consequently, the xerogel remain optically transparent throughout gelation.

Aging Mechanism

Aging is a process by which the gel structure is reinforced via surface area minimization of the spherical particle chains; this is shown in Figure 2-15. The surface area can be minimized by four possible mechanisms: (1) condensation of surface silanol groups (zipper effect) which creates stress and then results in vacancies in the neck area between particles, (2) thermally activated transportation of silica molecules from the volume or from the particle neck boundary to vacancies, (3) deposition of monomers from the liquid into the negative curvature area of two weakly connected spherical particles, and (4) dissolution of monomer from the particles' area of positive curvature into the pore liquid, as shown in Figure 2-16.

The first, third, and fourth mechanisms do not result in gel shrinkage; the second of these mechanisms does [47]. The particle rearrangement involved in the second

- (a) No surface area minimization at the time of gelation point.



- (b) surface minimized after aging.

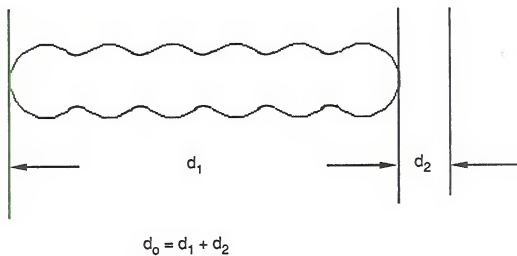
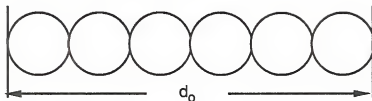
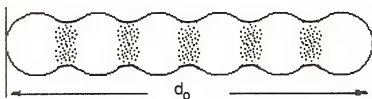


Figure 2-15 Surface minimization in the neck area.

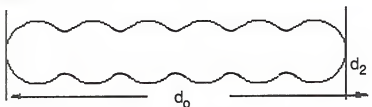
(a) at the time of gelation point ($t_g = 0$)



(b) the first mechanism: formation of vacancies in the necks of chain, the total length d_0 does not change



(c) the second mechanism: migration of vacancies from neck area out of gel body, the total length d_0 shrinks.



(d) silanol groups depart from the positive curvature area of particle's surface (the third mechanism) and deposit on the negative curvature area (the fourth mechanism).

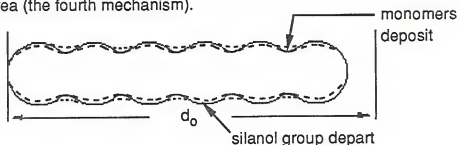
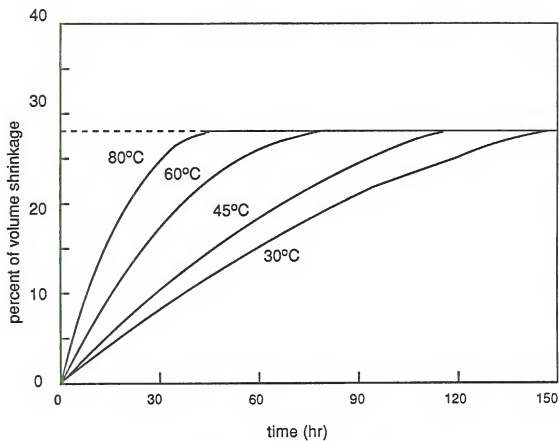


Figure 2-16 Surface minimization during aging.

mechanism is initiated by thermal energy. Therefore, the higher the aging temperature, the faster is the rate of matter migration to vacancies and the more rapid is gel shrinkage, as shown in Figure 2-17. About the same maximum shrinkage ($\approx 28\%$) is associated with each aging temperature. It is possible that the same amount of vacancies are quickly created inside the necks between particles during the first stage, mechanism No.1, for all identical gels. Subsequently, all of these vacancies are annealed out of the gel body in the second stage, mechanism No. 2, and then equal shrinkage is obtained. The same maximum shrinkage in the aging stage is probably predetermined by the processing characteristics of each gel (e.g. pH, water, DCCA, TMOS ratio). The gel shrinkage kinetics can also be monitored by the time at which 28% maximum gel shrinkage is observed at each temperature, as shown in Figure 2-18. Shrinkage improves gel strength; therefore, a relatively hard and dense gel can be obtained as a result of optimizing the aging process. Figure 2-19 shows the increase in gel microhardness with percentage of shrinkage. It is this increase in mechanical strength with aging that makes it possible to obtain dried monolithic xerogels.

Drying Modeling

Control of drying is critical; without a full understanding of the gel's drying mechanism and the development of a suitable method to deal with it achieving a dried xerogel without cracking is very difficult. Drying control involves both chemical and physical aspects. Chemically, the use of an acidic DCCA in the sol minimizes the particle size which results in an increased gel strength and a more homogeneous particle-size distribution, thereby diminishing uneven pore stresses. Physically, the use of a drying control chamber decreases the effect of differential pressures on the gel body which could lead to stress fracturing.



*time starts from the gelation point.

Figure 2-17 Shrinkage of silica gel inside 100 cc polystyrene cylinder as a function of aging time.

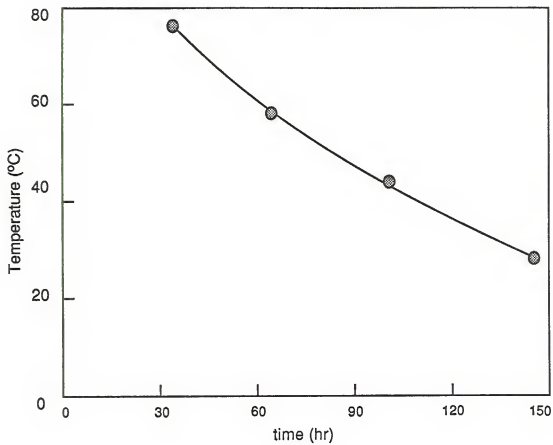


Figure 2-18 The time silica gels shrink to 72% of original volume versus aging temperatures inside 100 cc polystyrene cylinder.

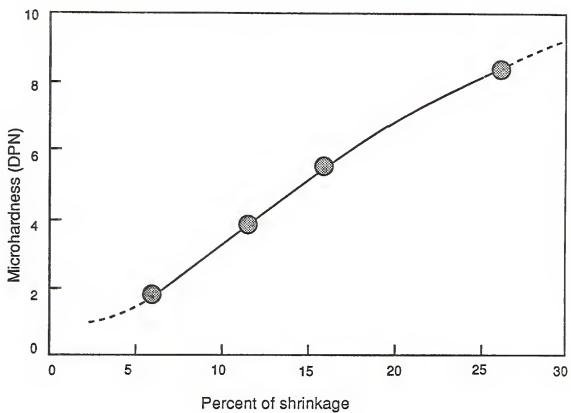


Figure 2-19 Microhardness of aged gel versus percentage of shrinkage.

A silica gel is defined as "dried" when the physically adsorbed water is completely evacuated and no significant weight loss is observed at increased temperatures.

Cracking during the drying process is essentially the result of differential evaporation of pore liquid, Figure 2-20, as discussed in detail by J. Zarzycki [48]. The Laplace equation is used:

$$\Delta P_{vl} = P_l - P_v = 2\gamma_{vl} \cos \theta / R \quad (6)$$

where ΔP_{vl} is the differential capillary vapor pressure between the surface of the vapor phase (in which vapor pressure = P_v) and the liquid phase (in which vapor pressure = P_l), within a very small pore of radius R . In equation (6) γ_{vl} is the specific surface energy, and θ is the contact angle.

Theoretically, to prevent shattering of the gel body during drying, the capillary vapor pressure in the liquid phase (which is transmitted to the wall of the pore channel) must be offset by the capillary vapor pressure in the vapor phase. For ΔP_{vl} to equal zero, the cosine of the contact angle must also equal zero (@ $\theta=90^\circ$), as the radius (R) and the surface energy (γ_{vl}) at the liquid-vapor interface will always have some value. Young's equation for the equilibrium of a solid (s) - liquid (l) - vapor (v) system is derived by balancing the horizontal components of the specific surface energies, γ_{sl} , γ_{sv} , γ_{vl} of the system. The equilibrium equation is given as:

$$\gamma_{sv} = \gamma_{sl} + \gamma_{vl} \cos \theta \quad (7)$$

As cosine θ becomes zero, this equation simplifies to $\gamma_{sv} = \gamma_{sl}$. This means that the work required of the liquid to act on the wall of the solid is the same as the work required of the vapor to act on the wall of the solid.

$$\cos \theta = 0$$

$$\gamma_{sv} = \gamma_{sl}$$

$$A_{sv} = A_{sl}$$

$$\gamma_{sv} dA_{sv} = \gamma_{sl} dA_{sl}$$

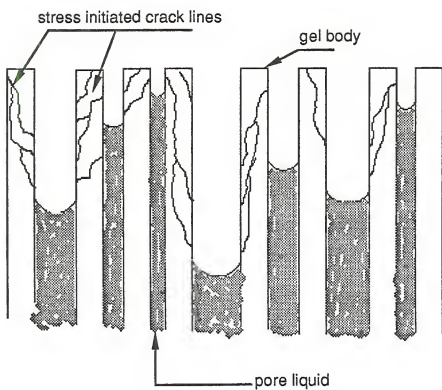


Figure 2-20 Differential evaporation.

$$P_{sv}dV_{sv} = dw_{sv} = \gamma_{sv}dA_{sv}$$

$$P_{sl}dV_{sl} = dw_{sl} = \gamma_{sl}dA_{sl}$$

$$\Delta P_{vl} = P_{sv} - P_{sl} = 0$$

$$PV = nRT \text{ (for ideal system)}$$

$$PV = W/M \cdot XT \text{ (for real system)}$$

$$P_{sv}dV_{sv} = XT_{sv}d(W/M) = P_{sl}dV_{sl} = XT_{sl}d(W/M)$$

where

W = weight of vaporized liquid

M = molecular weight of liquid

X = vapor constant

The actual pressure of the vapor phase per unit area of pore wall is the same as the actual pressure of the liquid phase per unit area of pore wall; this is called the saturation point or equilibrium vapor pressure [49]. When ΔP_{vl} is zero, there is no difference in the liquid level within the capillary pore channels regardless of the pore radius, as shown in Figure 2-21.

However, for the case of drying actual xerogels the differential pressure ΔP_{vl} can be minimized to zero with the use of a proprietary device. This device keeps the vapor pressure in the vapor phase, P_v , at a value the same as that of the vapor pressure in the liquid phase, P_l , in the gel. As a result, ΔP_{vl} is zero and gel remains intact. The vapor pressure within this device is controlled by the temperature which must be carefully maintained. At temperatures higher than the boiling point temperature of the gel pore liquid, the vapor pressure in the liquid phase, P_l , exceeds one atmosphere (P_v will never be higher than 1 atm in this device because it is not an autoclave system). Thus the system will equalize as gas escapes from the device, i.e., ΔP_{vl} is not zero, which would cause a differential vapor pressure ΔP_{vl} between the liquid and the vapor phases sufficient to shatter the gels, as shown in Figures 2-20 and 2-22(a).

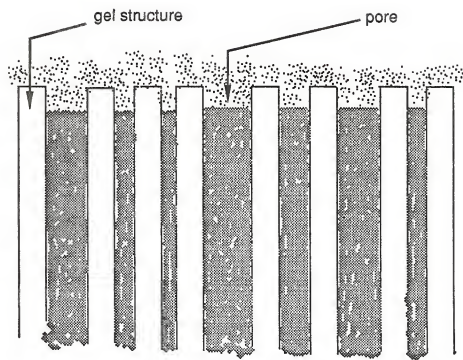
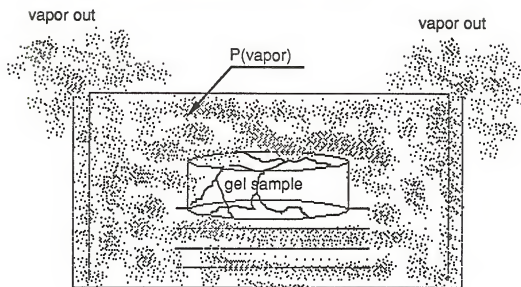


Figure 2-21 No differential evaporation.

(a)

 $P(\text{air}) = \text{one atmosphere (1 atm)}$  $P(\text{vapor}) > P(\text{air})$

(b)

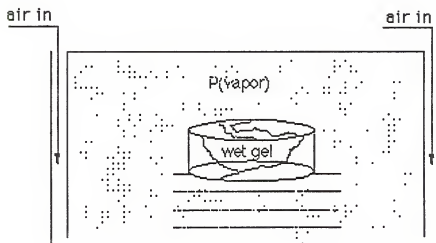
 $P(\text{air}) = \text{one atmosphere (1 atm)}$  $P(\text{air}) > P(\text{vapor})$

Figure 2-22 Gel cracks inside nonequivalent evaporation containers.

At temperatures lower than the boiling point of the gel pore liquid the vapor pressure in the liquid phase (P_l) is less than one atmosphere; therefore, air will enter the device to establish a vapor phase pressure (P_v) equal to 1 atm, resulting in a differential vapor pressure (ΔP_v) which is not zero (Figures 2-20 and 2-22(b)). However, by maintaining a zero differential pressure the capillary force is eliminated (Figure 2-23), thereby significantly removing the differential hydrostatic stresses within the gel body and retaining the gel's monolithic shape.

Structural Characterization

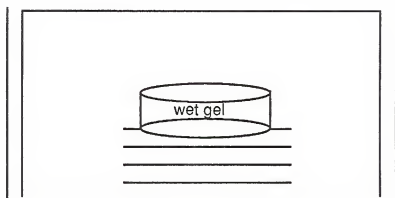
The gel consists of a three-dimensional network of silica particles rigidly linked together. If the structure of the gel is relatively coarse, the gel body is fragile and likely to shatter. If the structure of the gel is relatively fine, consisting of fibrillar chains of very tiny particles, and therefore somewhat flexible, the gel will be strong enough to shrink considerably without cracking. However, the shrinkage of a silica gel is irreversible. Shrinkage occurs as the gel dries due to the surface tension of the liquid within the pores. As drying occurs it is probable that certain bonds on the necks between particles break, which allows portions of this area to be dissolved into the pore liquid and transported to areas of negative curvature, as shown in Figure 2-24. This is because solids minimize surface area so as to reduce surface energy to a minimum.

An equation relating the solubility of a curved solid surface in water to the radius of curvature was derived by Ostwald and Freundlich [see p. 50-51 in ref. 4]:

$$\text{Log}(S_r/S_i) = KE/Tr \quad (8)$$

where S_r is the solubility of a particle having a radius of curvature r ; S_i is the solubility of a flat surface with a radius of curvature of infinity in that water; E is the surface energy of the solid; T is the temperature; and K is Boltzmann's constant. The meaning of this equation is schematically illustrated by Iler in Figure 2-25. As

$P(\text{air}) = \text{one atmosphere (1 atm)}$



$$P_{\text{atm}(\text{air})} = P_{\text{vapor}} = P_{\text{liquid}}$$

Figure 2-23 Situation to avoid cracking.

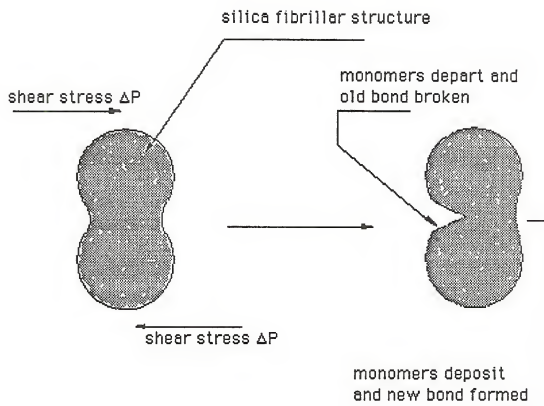


Figure 2-24 Redeposition of monomers from the broken neck area to the area of negative curvature.

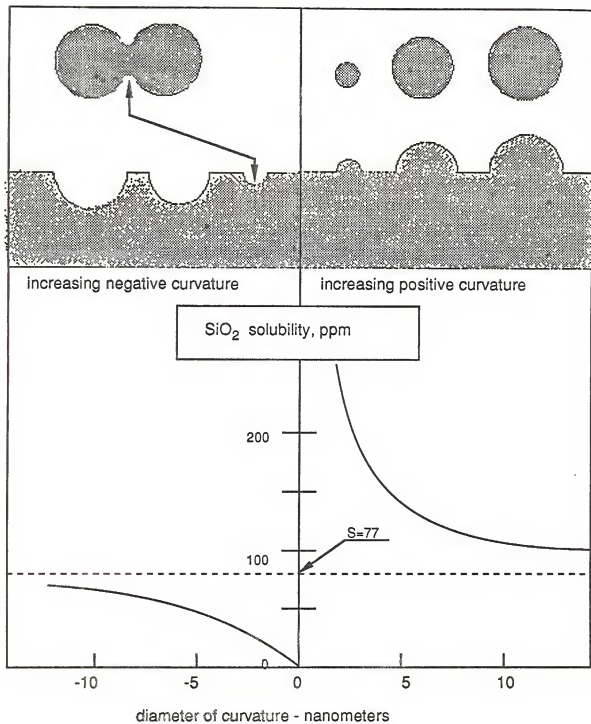


Figure 2-25 Solubility of silica in neutral water at 25°C varies with the radius of curvature of the surface according to the Ostwald-Freundlich equation.

shown, when an acidic silica gel is sufficiently dried to contain pores (negative curvature in left side of the figure) that are only a few nm in diameter a small decrease in pore size results in sudden elimination of the pores. Table 2-1 confirms that the remaining uniform pores stay unchanged in diameter but decrease in total volume and surface area as the sintering temperature increases.

A mechanism was suggested by Iler [47] that in a densification process, gel shrinkage is the results of sudden decomposition of pores into vacancies in the gel structure and traveling vacancies which migrate to the outside of the gel body along the surface of the pore network and do not remain in the pores to enlarge them [50].

Experimental Procedure

Large scale monolithic dried silica gel samples (up to 10 cm x 8 cm x 2 cm), as in Figure 2-26, have been routinely produced by applying the concepts and mechanisms stated in Section II of this chapter. Several kinds of standardized samples were made for characterization in this study including pure silica gels, cobalt- copper- and nickel-doped silica gels, neodymium- and erbium-doped silica gels. The two examples described below detail the procedure used to produce both pure silica and doped silica samples. Six steps are generally needed to produce the sol-gel derived monolithic silica gel-glass samples, as shown in Figure 2-27. The drying control chemical additive (DCCA) is introduced in Step 1; this makes it possible to control each of the five subsequent steps and prevent gel shattering.

Table 2-1
Oxalic acid (5.0 grams) as DCCA in 200 cc H₂O/100 cc TMOS

Temperature	200°C	450°C	750°C	800°C	830°C
Surface area (m ² /g)	651.12	612.10	413.25	385.47	335.40
Total pore volume (cc/g)	0.36	0.33	0.22	0.20	0.18
Average pore radius (Å)	11.02	11.03	11.06	11.03	11.05

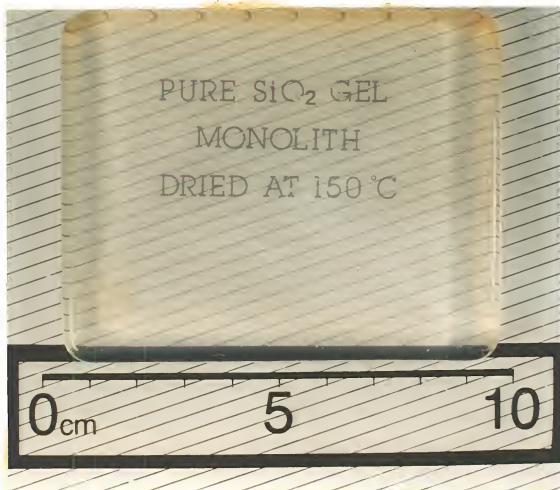


Figure 2-26 Picture of a large scale 160°C dried silica gel sample.

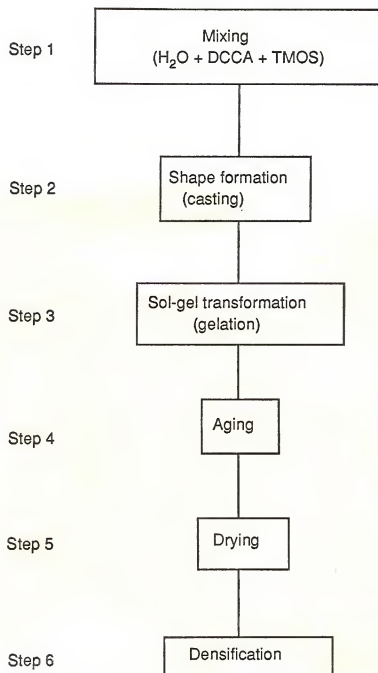


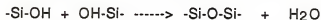
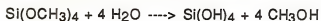
Figure 2-27 Procedure for producing pure silica gels and gel-glasses.

Example one:

Production of dried pure silica gel monolith from oxalic acid DCCA

Step 1: Mixing

Tetramethylorthosilicate (TMOS) is used as a precursor for silica monomers to form Si-O-Si bonds in the gel structure. The mixing of water with TMOS forms a silica sol via the following simplified hydrolysis and polymerization reactions:



The specific standard procedure followed in Step 1 is:

- (a) Pour 300 cc of water into a clean 800 cc beaker.
- (b) Place the beaker on a hot-stirring plate.
- (c) Mix 6 grams of oxalic acid with water using a PTFE coated magnetic bar; control via the hot-stirring plate.
- (d) Stir for 5 minutes to get a homogeneous solution.
- (e) Add 150 cc TMOS to the acid solution, while continuing to stir vigorously for approximately 50 minutes.
- (f) Immediately increase the temperature from 25°C to 85°C by raising the temperature on the hot-stirring plate to maximum.
- (g) If feasible, carefully place ice water in a three-layer polystyrene thin film on top of the beaker to condense the hot vapor and return it to its solution.
- (h) Continue stirring and heating for approximately 50 minutes before casting.

Step 2: Casting

(a) The intimately mixed sol is cast from its heated vessel into a mold (20 mm H x 100 mm D) that corresponds to the final desired shape. For best surface results, polystyrene is the selected mold material.

(b) The duration of the casting operation is not critical since gelation does not occur until after casting is completed.

Step 3: Gelation

Gelation occurs in the mold with the resulting solid object taking the shape and surface finish of the mold. Gelation times with oxalic acid are typically 20 hours at 25°C and 4 hours at 70°C, depending on the relative concentrations of water, TMOS, and DCCA, as shown in Figures 2-11, 2-12, 2-13, and 2-14.

Step 4: Aging

The solidified gel is then placed into an aging oven at a temperature ranging from 50°C to 80°C for a times ranging from 20 to 48 hours to achieve maximum shrinkage.

Step 5: Drying

Prior to Step 5, control of the gel ultrastructure is governed by the DCCA which allows removal of the pore liquid without cracking the gel. Typically this is done by first removing the excess liquid present after gel shrinkage in Step 4. The pore liquid is then removed, consistent with the theory stated in Section II of this chapter, by confined evaporation over a temperature range from 70°C to 160°C for times ranging from 18 to 90 hours. An example of a typical heating program is shown in Figure 2-28.

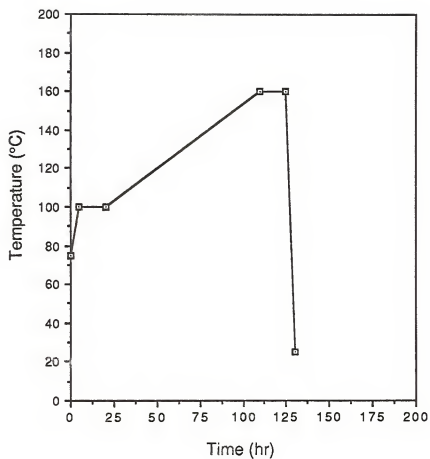


Figure 2-28 Drying program for wet gel.

Step 6: Densification

The ultraporous dried silica gels are converted to partially dense monoliths by heating from 150°C up to 900°C over a period of 3 to 6 days; samples are taken out of the furnace at the end of the heating program. An example is shown in Figure 2-29.

Example two:

Production of dried transition and rare earth element doped silica gels from nitric acid DCCA.

Step 1: Mixing

(a) Add 60 cc (1N) HNO_3 (nitric acid) to 340 cc of distilled water at room temperature and mix for 5 minutes with a magnetic stirrer.

(b) Add 200 cc TMOS to the nitric acid water solution while continuing to mix vigorously, increasing the solution temperature to 85°C for no more than 60 minutes.

Step 2: Casting

The intimately mixed sol (60 cc) is cast from its heated vessel into a polystyrene mold (20 mm H x 100 mm D) at room temperature. The length of time for casting should be no more than 110 minutes since gelation will take place during prolonged casting operation.

Step 3: Gelation

Gelation occurs in the mold at 55°C in 115 minutes with the resulting solid object taking the shape and surface finish of the mold.

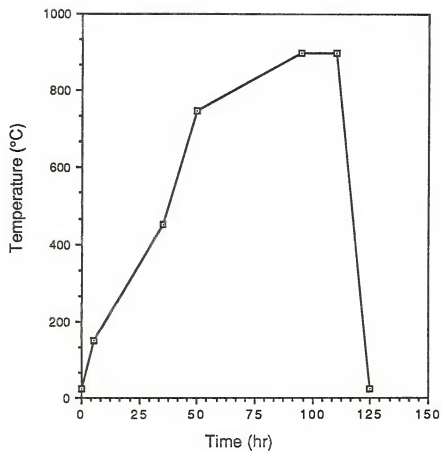


Figure 2-29 An example of a silica gel-glass densification program.

Step 4: Aging

The solid is aged in the mold initially at 55°C for 10 hours, followed by an increase to 80°C for 15 hours.

Step 5: Drying

The aged pure-silica gel is removed from the mold and dried with a controlled evaporation rate, as described in Section II of this chapter, initially at 70°C, gradually increasing the temperature to 160°C during a 90 hour period.

Step 6: Impregnation

(a) One gram-percent of transition metal element (i.e., cobalt nitrate, nickel nitrate, copper nitrate) or three gram-percent of rare earth element (i.e., neodymium nitrate, erbium nitrate) in deionized (DI) water is prepared for doping, or impregnating, the completely dried gel. The dried gel is immersed into the solution, whereby the interface between the liquid and the voids migrates from the exterior into the center of the gel body in the rate of 0.5 cm/hour, as shown in Figure 2-30.

(b) The doped gel is then placed in the drying oven at 200°C for 12 hours to remove the pore solvent.

Step 7: Densification

(a) The fully dried silica gel doped with transition metal or rare earth elements is heated to 400°C to eliminate any residual nitrates via conversion to its gaseous oxides.

(b) Additional densification can be achieved by heating from 400°C to 1000°C.

Results

Monolithic samples of pure silica gel, transition metal element doped silica gel, and rare earth element doped silica gel were routinely produced following these procedures; some are shown in Figures 2-31 to 2-35. The physical and optical properties of these samples will be discussed in succeeding chapters.

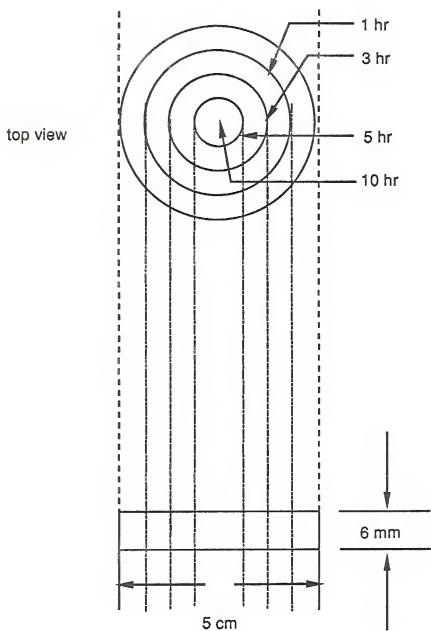


Figure 2-30 Sample immersion into transition metal or rare earth nitrate/water solution.

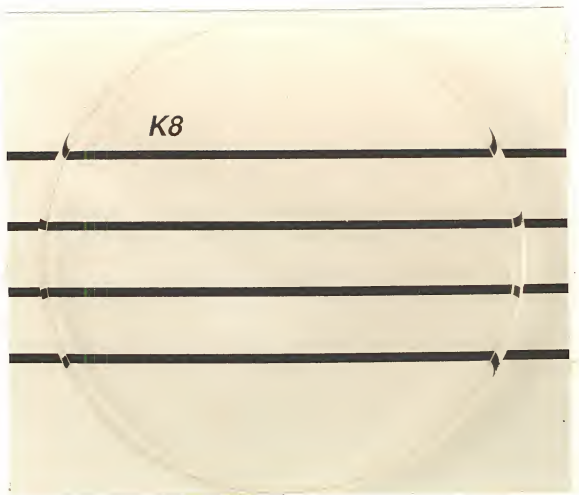


Figure 2-31 Picture of a 160°C dried silica gel.

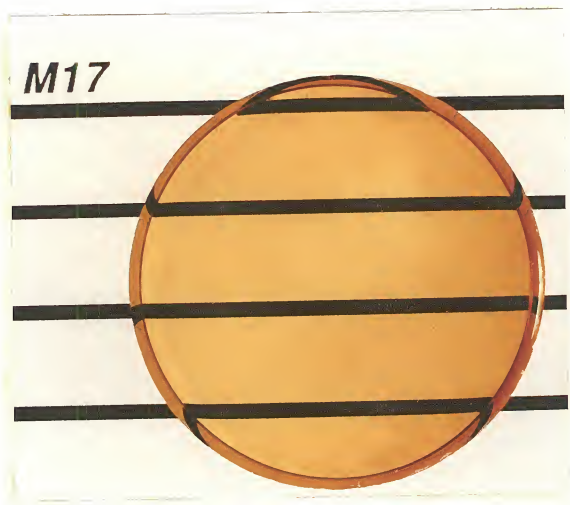


Figure 2-32 Picture of a cobalt nitrate-doped silica gel which was stabilized at 750°C and redried at 160°C.

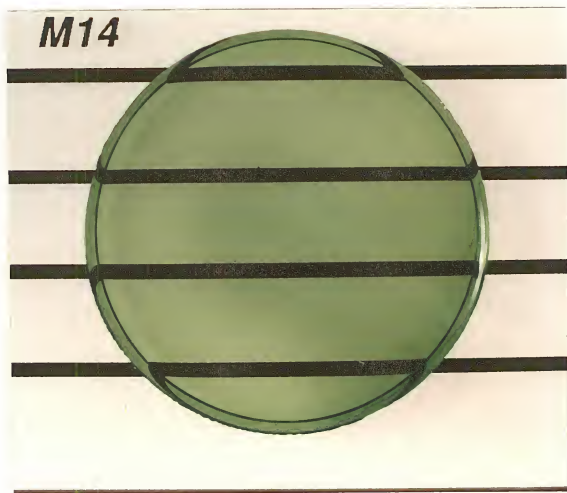


Figure 2-33 Picture of nickel nitrate-doped silica gel which was stabilized at 750°C and redried at 160°C.

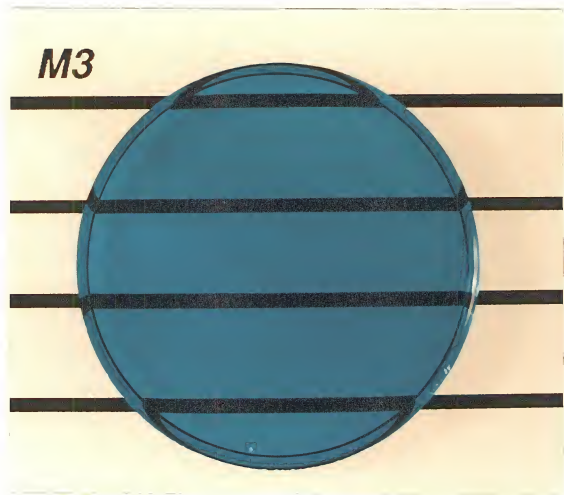


Figure 2-34 Picture of copper nitrate-doped silica gel which was stabilized at 750°C and redried at 160°C.

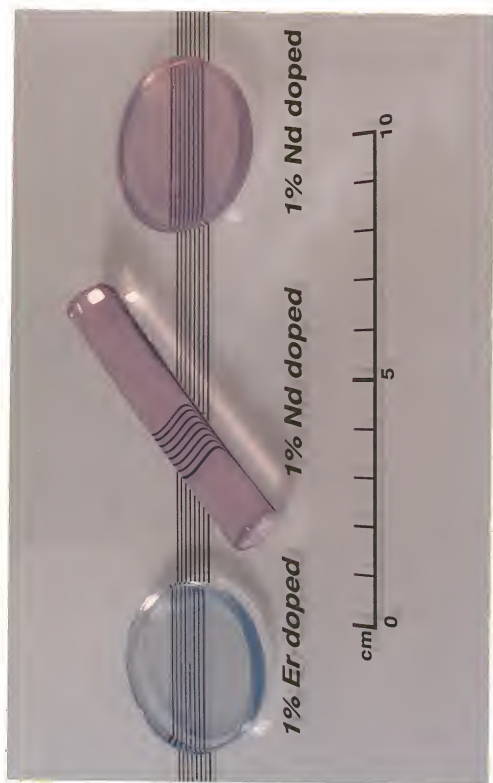


Figure 2-35 Picture of neodymium nitrate-doped and erbium nitrate-doped silica gels which were stabilized at 750°C and redried at 160°C.

Conclusions

It was not found necessary to add methanol to this xerogel system, though this is the practice of many researchers [51-56].

Addition of oxalic acid or nitric acid as DCCAs is necessary in the mixing step of both Examples #1 and #2 as an acidic DCCA controls the radius of the individual silica particles to a few nanometers that form during the early stage of monomer growth and the subsequent fiber-like polymerization.

The particles are made uniform due to Ostwald ripening at any moment of growth. As soon as particle growth stops at the pzc (point of zero surface charge), an electrically neutral particle surface forms; therefore, thermally activated Brownian motion, Van der Waals attractive forces and base catalytic effects among particles in the sol become the driving forces to form particle chains which reach the gelation point.

During aging, the reinforcement and the shrinkage of the fibrillar network of a gel proceeds as a result of growth of interparticle necks and migration of vacancies to the exterior of the gel. The rate of aging shrinkage is primarily determined by the rate of thermally activated vacancy migration.

After aging, the interparticle necks comprise a very large fraction of the gel fibrillar structure and become relatively flexible (like glass fibers are flexible). Consequently, the gel can endure certain hydrostatic stresses and shrink considerably in the drying stage without cracking, as illustrated in Figure 2-36.

Differential vapor pressure (ΔP_v) is the stress which shatters the relatively weak gel into pieces in the drying stage. A gel can be dried without cracking by using a drying device which eliminates the differential vapor pressure between vapor phase (P_v) and liquid phase (P_l) inside the capillary pores.

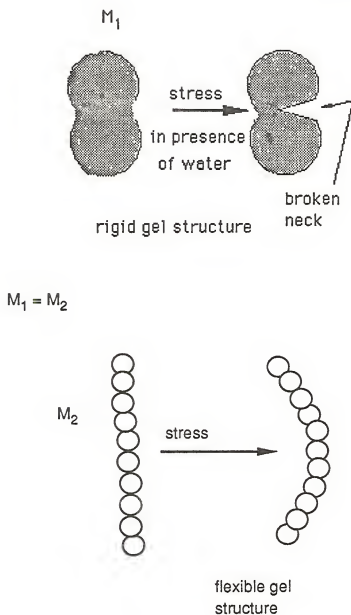


Figure 2-36 Fibrillar gel structure is relatively flexible compare to coarse gel structure.

Monolithic gels with an optimal ultrastructure and high resistance to drying stresses, which are chemically controlled (by adding acidic DCCA) and physically stabilized (by introducing a drying device), are identified by a change in visible light scattering during the drying process. The optical sequence for a drying gel is as follows: complete transparency with a very slight blue tone, followed by an opaque stage, followed by transparency. These changes in optical properties can be used to monitor the drying process and therefore offer the potential to be used in a feedback loop to optimize drying. Monitoring weight loss can also help to achieve the final stage of drying; when the theoretical molecular weight of silica is reached, drying is finished. This process can be automated and used with computer aided processing.

The fully dried gels can be modified by liquid phase impregnation of various chemical species (e.g., compounds of transition or rare earth elements) into the dried gel. Because of the extremely small size ($10 \text{ \AA} - 100 \text{ \AA}$) of the ultrapores in the gel, it is possible to introduce a very homogeneous ion distribution within the gel matrix. For measurements the physical properties presented in Chapter 3, the ultraporous dried silica gels are converted to partially dense monoliths by heating from 150°C to 900°C over times ranging from one day to one week.

CHAPTER 3 PHYSICAL PROPERTIES OF PARTIALLY DENSIFIED SILICA XEROGELS

Introduction

Monolithic, noncrystalline, dried xerogels of pure silica, hereafter simply called gels, have been made by the procedure stated in Example #1 of Chapter 2. These samples are heated to 150°C (the temperature at which the gels are free from physical water) to become standard dried gels.

The physical properties of the fully dried gel are a function of the internal structure which depends on the various chemical and physical conditions during every step of processing (i.e., the relative amounts of water/DCCA/TMOS, temperature, pressure, and time for aging and drying).

At sufficiently high temperatures thermal energy provides the driving force for ultrastructural rearrangement which decreases surface area and thereby minimizes surface tension inside the gel structure. This is the primary mechanism for densification [see p. 469-490 in ref. 23].

A large reduction in pore volume is accompanied by the decomposition of residual organic compounds into carbon dioxide (between 250° and 450°C) and also by the combining of surface hydroxyl groups resulting in some degree of dehydration. Both of these phenomena may cause thermally induced stress fracturing in the densification stage. However, by controlling the rates of these reactions silica gel monoliths that are crack-free, partially densified and shrunk, can be successfully made at various temperatures, ranging from 200°C to 850°C.

This chapter presents a study of the physical properties of partially dense silica-gel monoliths. Data were obtained from numerous measurements including structural, optical, thermal, and mechanical testing. Structural information was provided by

Fourier-transform-infrared (FTIR) spectroscopy, ultraviolet-visible-near-infrared spectroscopy (UV-VIS-NIR), N₂ adsorption-desorption isotherms interpreted using Brunauer, Emmett, Teller (BET) analysis which includes specific measurements of surface area, pore size distribution, pore volume, and pore radius, as well as large angle X-ray diffraction. Optical information was obtained solely using an index of refraction test. Thermal data were collected from differential scanning calorimetry (DSC), differential thermal analysis (DTA), thermogravimetric analysis (TGA), and thermomechanical analysis (TMA). Mechanical properties (gel strength) were determined using flexural strength, compressive strength, microhardness, fracture toughness and density measurements.

Review of the Literature

Three mechanisms of densification are summarized by Zarzycki, et al. and Brinker, et al. [25, 57]: (1) polymerization reactions which serve to crosslink the network and partially release the surface hydroxyl groups, thereby forming free water; (2) structural rearrangements that occurs when segments of interparticle necks are broken and other neck segments become connected; and (3) viscous sintering accompanied by the combination of surface hydroxyl groups. The first two mechanisms cause a slight density increase; the third mechanism is a result of high temperature viscous flow which eliminates the pores so that the bulk density approaches that of fused silica. No gel can be completely dehydrated and converted into a fully dense glass (i.e., without foaming) in an ordinary air-atmosphere furnace; but fortunately, the gel can be partially sintered to a desired temperature, below the foaming point, and cooled to room temperature while remaining intact.

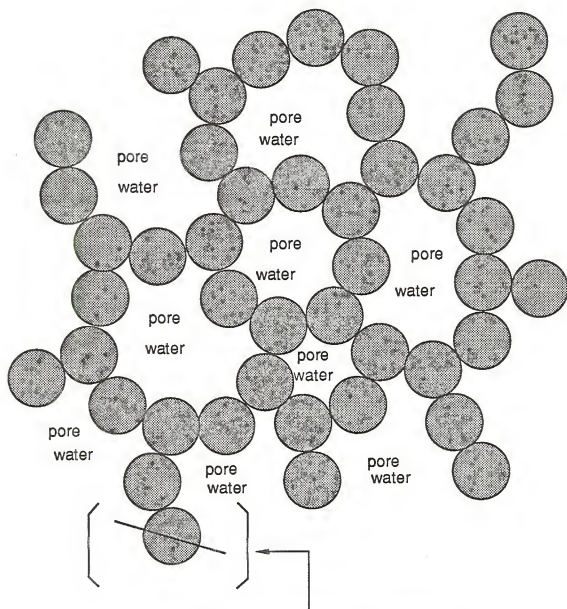
Any material can give rise to absorption or emission of radiation within the allowed transitional, vibrational, and/or rotational energy levels. Infrared spectroscopy

(FTIR) can provide vibrational information on changes occurring in the gel structure during sintering [58].

Water terminates the bridging silicon-oxygen-silicon bonds on the particle's surface inside the porous gel, as shown in Figures 3-1 and 3-2. Water's disruption of the Si-O-Si bridging bond is similar to that of sodium ions within a dense soda silicate glass. This gives rise to absorption in the ultraviolet (UV) region of the optical spectrum. The UV-VIS-NIR spectra technique is an easier and more sensitive tool than the infrared method for understanding the evolution of bonding and identifying the species inside the gel structure in the densification process [59].

The measured surface area, obtained from BET analysis, of a standard dried gel is about 750 m²/g at 200°C. The particle size is calculated from Havard, Wilson's model [60] where the diameter is equal to a constant (2750) divided by the surface area. The particle diameter for a gel made by Example #1 in Chapter 2 is 3.6 nm at 200°C. The measured surface area is somewhat less than actual since nitrogen molecules, used in the BET analysis, cannot completely penetrate the negative curvature area between all the connected particles. However, the BET surface area measurement also includes the surface hydroxyl groups which increases the particles' measured surface area value; this increase is less significant than the decrease resulting from incomplete nitrogen penetration.

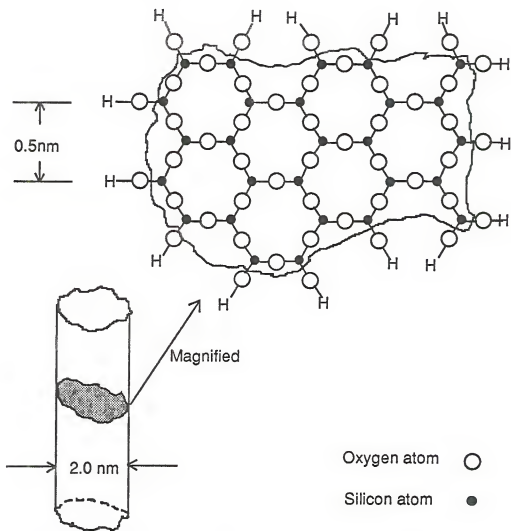
Silica gel is essentially a special form of porous glass. Previous x-ray diffraction studies by Mozzi, Warren, Uhlmann and Wicks [22, 23] have established in detail the tetrahedral bonding arrangements in vitreous silica. The maximum in the distribution of Si-O-Si angles in amorphous silica is at 144°, with most angles being within 10% of this maximum. There is no evidence for a preference in fused silica for edge-to-face sharing of tetrahedra, which is often found in crystalline silicates. X-ray diffraction patterns generally exhibit a relatively broad peak for gels indicating the absence of atomic periodicity or long-range structural ordering compare to that of quartz.



cut-off profile magnified in Figure 3-2

Figure 3-1 Random sampling profile of gel skeleton.

A profile of gel skeleton



Gel fibrillar structure cut off profile

Figure 3-2 Water terminates the Si-O-Si bridging bond on the particle's surface.

Consequently, a random edge-to-edge sharing of silica tetrahedra with variable Si-O-Si angles described above is proposed for silica gel fibrillar structures.

The magnitude of index of refraction (n) indicates the extent of change of the speed of light by the electromagnetic field of a transparent dense material. The index of refraction can be expressed by Snell's law $n_{\text{(glass)}}/n_{\text{(vacuum)}} = \sin \theta_{\text{(vacuum)}}/\sin \theta_{\text{(glass)}} = v_{\text{(vacuum)}}/v_{\text{(glass)}}$, where $n_{\text{(glass)}}$, $v_{\text{(glass)}}$, and $\theta_{\text{(glass)}}$ are the refractive index, the velocity, and the angle of refraction of glass respectively, $n_{\text{(vacuum)}}$, $v_{\text{(vacuum)}}$ are constants, and $\theta_{\text{(vacuum)}}$ is the angle of incidence of light in vacuum.

Index of refraction is a dependence of (1) the density, (2) the polarizability of the glass, and (3) the wavelength (λ) of monochromatic radiation [61]. In this chapter partially densified silica gels are discussed where the chemical compositions are essentially SiO_2 and chemical bonded surface $-\text{SiOH}$ groups. The nonbridging hydrogen ions (H^+ , a proton) of these silanol groups contribute very little effect on oncoming light [see p. 660 in ref. 23], thus, the polarizability of these partially densified silica gels can be assumed to be a constant. Consequently, the variation of refractive index with density described by the Lorentz-Lorenz equation [see p. 658 in ref. 23] can be simplified as will be discussed in the Results and Discussions Section of this chapter.

Differential scanning calorimetry (DSC) is used to measure the temperatures associated with transitions in materials, including boiling points, melting points, liquid-crystal transitions, heats of reaction, specific heat capacity, oxidative and thermal stability, purity, glass transitions, and reaction kinetics.

Differential thermal analysis (DTA) gives the same qualitative information as DSC, but is used primarily for studies involving high temperatures which exceed the range of the DSC cell (700°C).

Thermogravimetric analysis measures weight change as a function of temperature, and provides derivative TGA data used to quantify the chemical changes in a gel during thermal processing.

Thermomechanical analysis (TMA) measures the thermal expansion coefficient, glass transition temperature, softening temperature and provides data for gel shrinkage analysis [62].

Flexural (FLEX) and compressive (COMP) tests are performed to determine the material's strength under external mechanical loads.

A Vickers microhardness test, which yields a value for the diamond pyramid microhardness number (DPN), is used to measure the mechanical resistance of a gel and gel-glass to diamond pyramid plastic indentation in a microscopic area of the surface [63]. The fracture toughness is obtained directly from the crack length which extends outside the diagonal of diamond pyramid indentation during the Vickers microhardness measurement [64].

Bulk density measurements are used to monitor the change in gel structure during sintering; it also gives useful information for interpreting variations in refractive index.

Experimental Procedure

Samples, fabricated by the procedure stated in Example #1 of Chapter 2, were heated to various programmed temperatures in an ambient air furnace, as shown in Figure 3-3. The following tests, listed in Table 3-1, were performed on these samples.

The Infrared spectra were recorded on a Nicolet MX-1 FTIR spectrometer equipped with a diffusion reflection stage and a microcomputer for data storage. The diffusion reflection stage in which the infrared passes into the bulk (about 0.5 mm deep and 20 mm² area) of the gel, undergoes reflection, refraction, scattering and absorption in varying degrees before returning back at the sample surface. The radiation reflected out from the gel is distributed in all directions of the surrounding hemisphere and corrected to form spectra by a highly reflective semispherical mirror. Chemical species and bonding information can be interpreted in terms of the position and intensity of IR

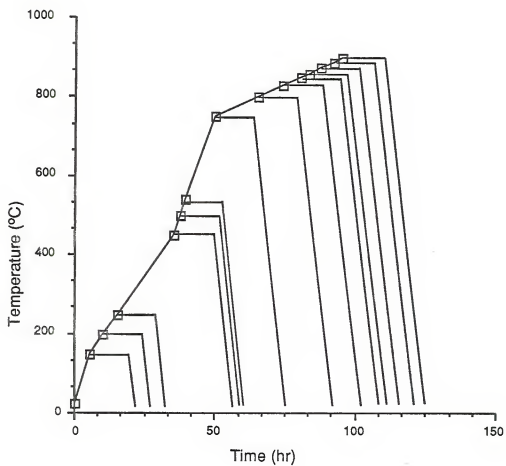


Figure 3-3 Heating programs for various samples

Table 3-1
Physical property measurements

TEST	SAMPLE SHAPE	HEATED TEMP. (°C)
Structural information tests:		
FTIR	flat piece (smooth surface)	150, 250, 500, 800
UV-VIS-NIR	flat piece (smooth surface)	150, 350, 500, 800
BET	powder (course ground)	200, 450, 750, 830, 860
X-Ray	powder (fine ground)	200, 450, 750, 800, 850
Optical information test:		
Index of refraction	polished flat piece	150, 450, 750, 800, 830
Thermal information tests:		
DSC	broken piece	150
DTA	broken piece	150
TGA	broken piece	150, 740
TMA	smooth cylinder's ends	150, 540
Mechanical information tests:		
FLEX	rectangular piece	150, 450, 750, 830
COMP	rectangular piece	150, 450, 750, 830
DPN	unpolished gel surface	150, 250, 450, 750, 800, 830
Toughness	unpolished gel surface	150, 250, 450, 750, 800, 830
Density	broken piece	150, 250, 450, 750, 800, 830

peaks in the sample's spectra. A dried gel was installed in a hot stage inside the FTIR sample chamber and heated to the temperatures designed in Table 3-1 for IR analysis. A heating rate of 3.3°C/min from room temperature to 800°C was used.

The ultraviolet-visible-near infrared spectra were obtained from a Perkin-Elmer Lambda 9 UV/VIS/NIR spectrophotometer. This instrument consists of a high performance double-beam, double-monochromator and a superior signal-to-noise energy optimized optical system [65] throughout the entire 185 to 3200 nm wavelength range; it is integrated with microcomputer electronics, video display, soft key operating system and printer. Gels heated to the temperatures designated in Table 3-1 and cooled to room temperature with heating programs shown in Figure 3-3 were taken out immediately from the furnace for testing. Subsequently, the thickness of the gels was measured and they were scanned at a rate of 120nm/min through a required wavelength range in either transmission or absorption mode after background correction had been made.

The surface area, total pore volume, average pore radius, and pore size distribution were determined by the nitrogen adsorption-desorption isotherm BET method, using an automatic Quantachrome Autosorb-6 sorption system [66].

Specific surface area (A) of the gels is obtained from a series of data management and calculations performed in the microcomputer of the Autosorb-6 system. The calculations involve: (1) a BET equation, $1/[W\{(P_0/P)-1\}] = 1/(W_m C) + [(C-1)/(W_m C)] \times (P/P_0)$ in which W is the weight of gas adsorbed at a relative pressure P/P_0 (pressure ratio of N_2 gas in He gas), W_m is the weight of adsorbate constituting a monolayer of N_2 on surface, and the constant C is related to the energy of adsorption in the first layer. (2) a linear plot of $1/[W\{(P_0/P)-1\}]$ vs P/P_0 to yield values of slope $s = (C-1)/(W_m C)$ and intercept $i = 1/(W_m C)$. (3) the weight of a monolayer W_m obtained by equation $W_m = 1/(s+i)$. (4) $A_t = (W_m N A_{cs})/M$ where A_t is total surface area of the sample measured and N is Avogadro's number. For N_2 at 77 °K, the cross-sectional area,

A_{cs} is 16.2 \AA^2 and M is the molecular weight of N_2 . (5) $A=A_s/W$ in which A is specific surface area of sample and W is the sample weight.

The total pore volume (V_{liq}) is derived from the amount of N_2 adsorbed at a relative pressure close to unity, by assuming that the pores are all filled with liquidized N_2 of a volume V_{liq} which can be calculated using equation $(V_{liq}/V_m)RT=P_a V_{ads}$ where V_m is the molar volume of the liquid N_2 , P_a is ambient pressure, and V_{ads} is vaporized pore liquid (N_2).

The average pore size can be estimated from the pore volume, by assuming cylindrical pore geometry; then the average pore radius r_p can be derived as $r_p = 2V_{liq}/A$. The pore size distribution is calculated using the method proposed by Barrett, Joyner and Halenda [67].

Samples heated to the temperatures designated in Table 3-1 and cooled to room temperature with the heating program shown in Figure 3-3 were ground into powder and weighed to around 0.6 gram in the pellet cells before installing in the Autosorb-6 system for outgassing and preheating to eliminate the water moisture. The outgassing and preheating was held for 15 hours at 200°C in N_2 gas atmosphere. Consequently, samples were transferred to the ports of the system for nitrogen adsorption-desorption isotherm measurements. Data were automatically accumulated in the microcomputer and the results printed out .

The X-ray diffraction analysis was obtained using a Philips diffractometer at room temperature with a 40Kv CuK_α radiation and a nickel filter. The samples heated to the temperatures designed in Table 3-1 and cooled to room temperature with heating programs shown in Figure 3-3 were ground and scanned at a rate of $6^\circ/\text{min}$ from 2θ angles of 10° up to 50° .

The index of refraction was obtained using a Pulfrich refractometer and a HeNe laser light source which wavelength is 632.8 nm. The principle of the refractometer is based on the measurement of the critical angle ϕ_c , which is the angle of the interface

between the unknown gel sample of index n and a prism of known index n' . Since n' is greater than n , the two must be interchanged in the standard equation, $\sin \phi_c = n/n'$ [68]. The beam is oriented such that some of its rays just graze the surface as shown in Figure 3-4, so that the transmitted light has a sharp boundary occurs which allows one to compute the value of ϕ_c and hence of n .

DSC, DTA, TGA, and TMA analyses were obtained with a DuPont 1090 thermal analysis system. In The DSC system, the gel sample and a reference were placed in pans which sat on a disk. Heat was transferred through the disk into the gel sample and reference. The differential heat flow to the sample and reference was monitored by the junction of a constantan disc and the chromel wafer which covers the underside of each platform. Chromel and alumel wires were connected to the underside of the chromel wafers, and the resultant wire-thermocouples were used to monitor the sample temperature. Therefore, heat transfer and temperature of the sample and reference could be recorded. The temperature range of the DSC cell is from room temperature to 600°C.

Differential thermal analysis (DTA) measures the temperatures at which heat-related phenomena occur in materials. DTA provides the same qualitative information as DSC, and can provide semiquantitative calorimetric measurements. The temperature range of the DTA cell is from ambient to 1200°C.

The high temperature 1200°C DTA cell consist of a platinum sample and reference cups resting on the tops of two insulated thermocouple pedestals. The sample and reference were located 6 mm apart surrounded by a programmable furnace. Thermocouples located in the pedestals measured both the presence of transitions and the temperatures at which they occur. DTA cells complement the DSC to offer appropriate measurements over a wide temperature range.

The thermogravimetric analyzer measures changes in weight as a function of temperature, and provides derivative TGA data. These data can be used to measure the

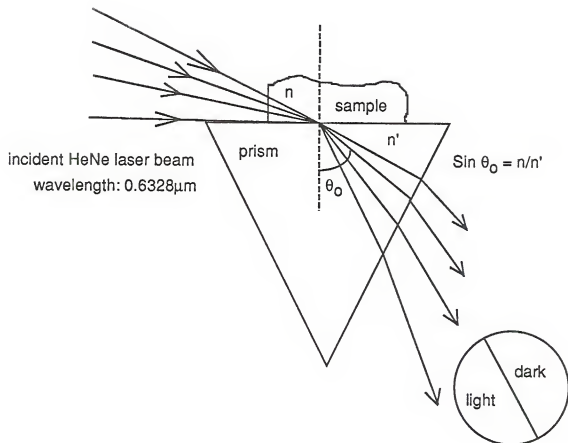


Figure 3-4 Refraction in the prism of a Pulfrich refractometer.

changing in moisture and volatiles (oxidation reaction) when gel is in the heating process.

A thermomechanical analyzer (TMA) can be used as a dilatometer to measure gel volume shrinkage, or glass expansion coefficient from room temperature to 800°C. The sample was installed in a programmable furnace in which a thermocouple in direct contact with the sample measured the sample temperature. A movable-core linear variable differential transformer (LVDT) whose output is proportional to the linear displacement of its core is used. The dimensional change of the sample with temperature can be monitored using this LVDT core displacement technique.

Flexural strength tests were performed under guidelines of the ASTM D 790M-84 standard [69]. Samples heated to the various temperatures (see Table 3-1) and cooled with the thermal schedule shown in Figure 3-3 were cut with a diamond wafering blade and polished carefully with 600 SiC grit paper into a size of length x width x thickness (46 mm x 10 mm x 5 mm). All samples were dried at 150°C for 3 hours immediately prior to measurements to eliminate absorbed moisture. Subsequently, the samples with a span : width : thickness ratio of about 7:2:1 were loaded in three-point bending in ambient conditions at a strain rate of $3.5 \times 10^{-3} \text{ s}^{-1}$ using an Instron model 1122. In this experiment a set of five identical samples were heated at same time in a furnace to each temperature.

The compressive strength tests were carried out under the guidelines of the ASTM C158-80 standard [70]. Samples heated to the designated temperatures (see Table 3-1) and cooled with heating programs shown in Figure 3-3 were cut into a rectangular shape of length x width x thickness (14 mm x 7.5 mm x 5 mm). All samples were dried at 150°C for 3 hours immediately prior to measurements to eliminate absorbed moisture. Subsequently, samples were loaded in an Instron model 1122 such that the length was parallel to the axis of the applied stress applied at a strain rate of $3 \times 10^{-4} \text{ s}^{-1}$. The

same number of samples and processing temperatures were used as that of flexural strength test.

Microhardness values were obtained using a 136° diamond pyramid indenter at a 50 gram load with the Micro Hardness Tester, model M-400 F (Leco Co. Japan). Samples were heated to the designated temperatures (see Table 3-1) and cooled with heating programs shown in Figure 3-3. Then, the samples were placed under the indenter and applied with the 50 gram load. Two diagonals of the indenter were produced on the surface of the sample. The DPN can be calculated by measuring the average length of two diagonals through the microscope on the instrument. In this test five indentations were performed on each sample to obtain the data.

Fracture toughness values were calculated using the extended crack lengths from the two stamped diagonals created by the diamond indenter on the surface of gel during the Vickers microhardness test. The calculations used to convert indentation length to fracture toughness are described by Anstis' relationship (Equation #16) [64] in the Results and Discussions of this chapter.

Density of the samples was determined using a simple mercury displacement technique. Samples followed the heat treatments shown in Table 3-1 and Figure 3-3 were immersed into a pycnometer. By knowing the sample weight, the corresponding weight of mercury displacement, and the density of mercury, the density of the sample was calculated.

Results and Discussions

Figure 3-5 shows the FTIR spectra for the partially densified gels heat-treated at various temperatures. The samples were scanned between 200 cm^{-1} (50000 nm) and 5600 cm^{-1} (1786 nm). The results show that the Si-O-Si molecular stretching

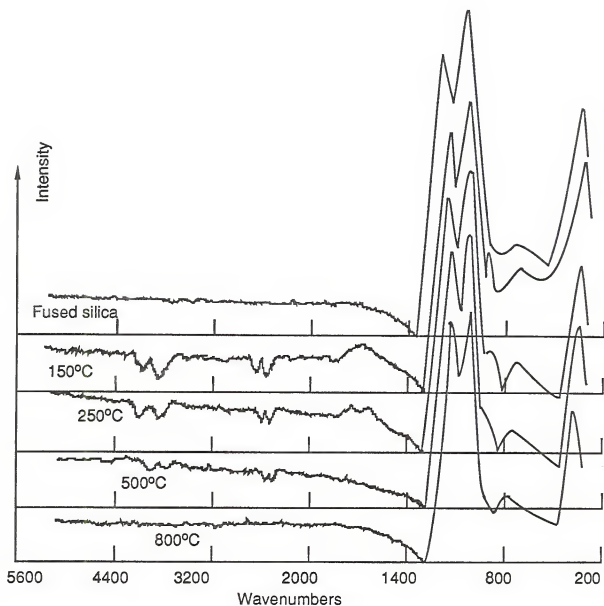


Figure 3-5 FTIR hot stage data from 25°C to 800°C of pure silica gel

vibration is observed at 1120 cm^{-1} (8928.6 nm), even in the low temperature sample. The peak at 1250 cm^{-1} (8000 nm) is an artifact of the diffuse reflection stage. The primary difference between these curves is that peaks corresponding to organic residuals in the range between 1400 cm^{-1} (7142.9 nm) and 2600 cm^{-1} (3846.2 nm) are absent in the high temperature sample. The spectrum of the 800°C silica sample is nearly the same as that for fused silica, with the exception of a small shift in the absorption edge near 1400 cm^{-1} (7142.9 nm) to lower wavenumbers.

The temperature-dependent changes in intensity of the characteristic absorption band at 950 cm^{-1} (10526.3 nm) have been attributed to the stretching vibration of the Si-O-H nonbridging oxygen (NBO) groups. With increasing temperatures, the concentration of silanol groups is decreased to a nondetectable level and the characteristic 950 cm^{-1} (10526.3 nm) peak disappears. The extent of hydroxyl absorption bands at 3500 cm^{-1} (2857.1 nm) to 4000 cm^{-1} (2500 nm) is also diminished for the higher temperature samples. This does not mean that the gel is completely free (zero ppm) from all types of water, but rather that the FTIR technique is not sensitive enough in this region (950 cm^{-1}) to detect the residual hydroxyl bonds to fully understand and monitor the water associated with gel structure. Overtone and combination frequencies should be investigated [71].

These results show that the only significant "impurity" in the ultrapure silica gel is water. The amount of water determines the extent of non-bridging oxygen (NBO) content, which prevents complete densification. Water content can also be observed easily using a UV-VIS-NIR spectrophotometer. Figure 3-6 shows the intensity of free water peaks at 1363.3 nm, 1891.1 nm, and 2212.4 nm decreasing with increasing processing temperature. It indicates that the densification is due to the combination of silanol groups on the surface of particles which form free water and escape; consequently, the surface chemical water is reduced and the absorption peaks are diminished.

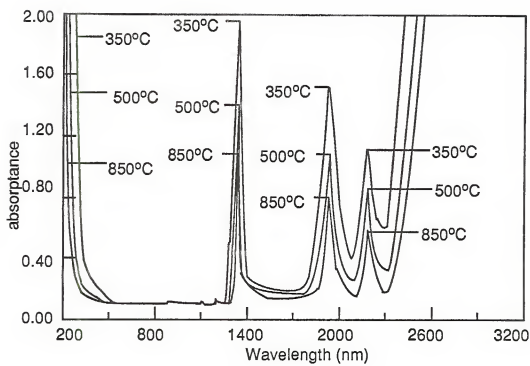


Figure 3-6 The absorbance peaks of water decreasing with increasing temperature.

Samples heated to different temperatures are compared with a pure silica melt glass (Dynasil) in terms of the cut-off wavelength, as shown in Figure 3-7. Increasing the temperature of the thermal treatment increases the optical transmission near the UV absorption end and shifts the uv cut-off to the short wavelength for the pure silica gels, apparently as the result of a decreased water content in the high temperature samples.

As Sigel concludes [72], the introduction of one electron valent elements (i.e. H, Li, Na, K, Rb, Cs, Fr, F, Cl, Br, I) produces a noticeable shift of the uv edge to longer wavelengths. This shift is because these elements terminate the bridging oxygens (BO) into nonbridging oxygens (NBO) and provide lower energy exciton levels for photo-electron excitations. More water-related phenomena will be discussed in detail in the dehydration study in Chapter 4.

Another important analytical technique for understanding the ultrastructure of partially densified gels is the N₂ adsorption-desorption isotherm analyses. The results include analysis of the variation of average pore radius, pore radius distribution, specific surface area, and pore volume with densification temperature, as shown in Figures 3-8, 3-9, 3-10, and 3-11. There was no significant change in pore size (Figures 3-8 and 9) while the total pore volume and surface area decreased (Figures 3-10 and 3-11) with temperatures up to 860°C. An assumption is that the pores decrease in number and force the entire gel body to contract. This is because the pores are very small (in this study, the mean pore diameter is only 2.2 nm). Consequently, they essentially obey the mechanism presented by the Ostwald-Freundlich equation, $\log(S_r/S_i) = KE/Tr$, stated in Chapter 2 Equation #8 and illustrated in Figure 2-21. Once the pores start to decrease in size, the rate of decrease becomes very fast and they immediately fill and disappear under the assistance of the migration of silanol groups along the interior surface and/or migration of vacancies through the structure to the exterior of the gel. Therefore, the gel shrinks as the temperature increases as a result of

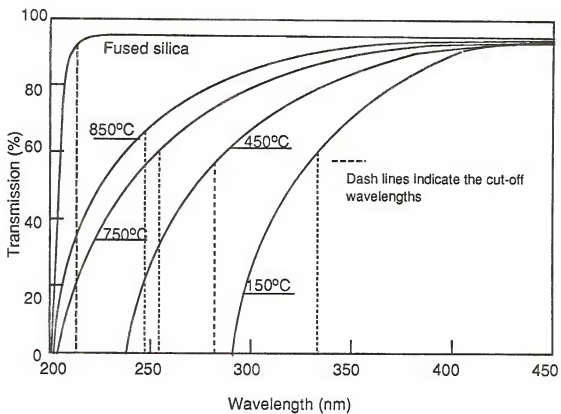


Figure 3-7 Transmission cut-off of pure silica gel

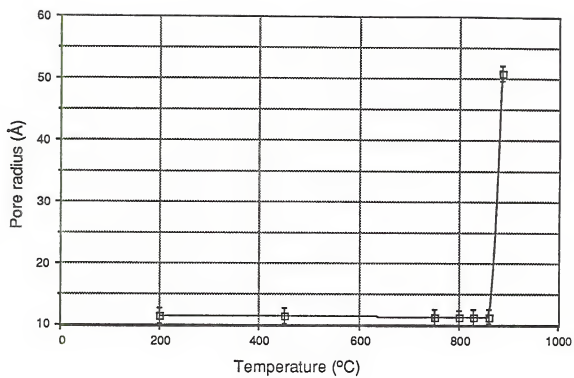


Figure 3-8 Pore radius vs. temperature

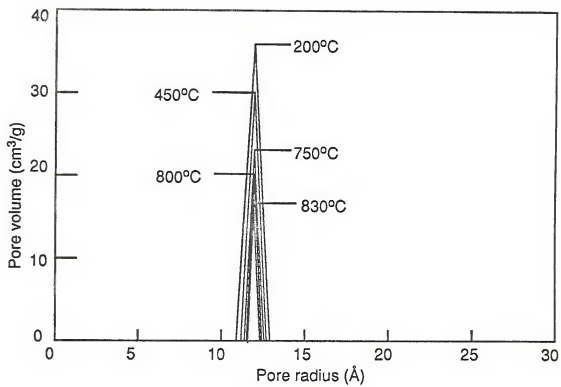


Figure 3-9 pore size distribution vs. pore volume at various temperatures.

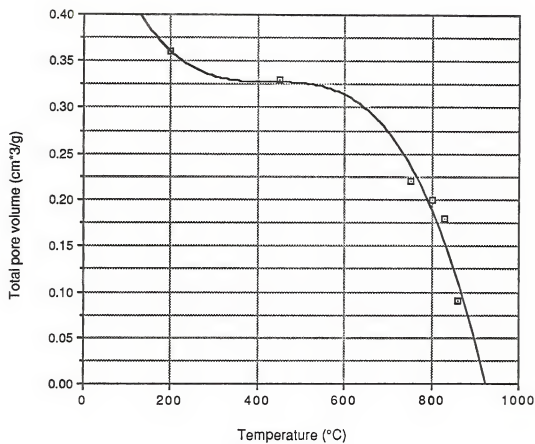


Figure 3-10 Total pore volume versus temperature.

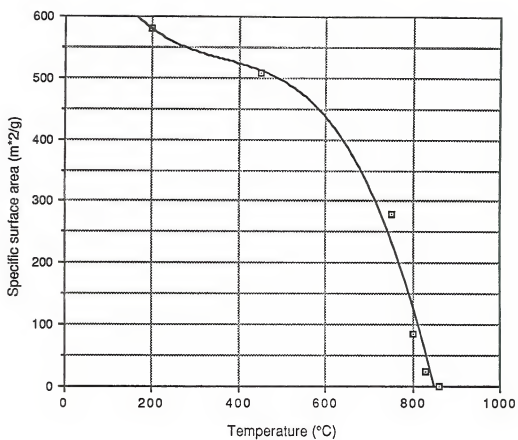


Figure 3-11 Specific surface area versus temperature.

the total pore volume decrease. It can also be reasonably assumed that the decrease of the surface area is linearly proportional to the disappearance of the number of pores.

When a gel is heated higher than its foaming temperature, free water is formed from the dissociated surface hydroxyl groups inside the fully densified gel structure. Immediately, these free water molecules follow the idea gas law in Equation #1 to create new pores:

$$pv=nRT \quad (1)$$

where p is internal pressure of a closed-pore volume v , n is a mole number of gaseous water molecules within an instantaneously created closed-pore v , $v = 4\pi r^3/3$ where r is the closed-pore radius, and T is gel body temperature at the moment foaming occurs. If N is the total molar number of gaseous water molecules in total of such created pores of V per unit volume of matter, then N/n is the total number of pores per unit volume of silica, and $V = Nv/n$ is total pore volume (V_{void}) per unit volume of silica (V_{solid}). Consequently, equations #2 and #3 can be written:

$$pV=nRT \quad (2)$$

$$V=(N/n) \times v = (N/n) \times 4\pi r^3/3 = (1- \rho)/\rho \quad (3)$$

where ρ , the relative density, is equal to ρ_a/ρ_r , $\rho_a = m_{\text{solid}}/(V_{\text{solid}}+V_{\text{void}})$ is the apparent density of the foamed silica gel and $\rho_r = m_{\text{solid}}/V_{\text{solid}}$ is the fully densified silica gel. Therefore, from Equations (2) and (3), we get:

$$p = 3nRT/4\pi r^3 = NRT\rho/(1- \rho) \quad (4)$$

When temperature exceeds the pore closing temperature, the gel immediately foams as soon as the surface water is released.

The gel foaming mechanism is explored by J. Phalippou, T. Woignier, and J. Zarzycki [73]. They use the concept that the rate of total energy input to the gel sintering system equals the rate of total energy output from the system. The total energy input includes the surface energy of silica gel ($dW_a/dt = 8\pi r\sigma dr/dt$) where r is the pore radius, σ is surface tension, and t is time and the external pressure energy is

$dW_b/dt = -PdV = -P \times 4\pi r^2 dr/dt$, where P is external pressure. The total energy output includes the energy for viscous flow ($dW_c/dt = 16\pi\eta\rho(dr/dt)^2$) where η is the viscosity of silica gel at the temperature of foaming, ρ is the relative density of the gel and the energy for varying the pore radius is $dW_d/dt = -pdV = -p \times 4\pi r^2 dr/dt$. The equation for this system is thus:

$$dW_a/dt + dW_b/dt = dW_c/dt + dW_d/dt \quad (5)$$

By replacing all the items, we get:

$$-2\sigma - r(P-p) = 4\eta\rho(dr/dt) \quad (6)$$

and by combining with Equation #3 yields,

$$2\sigma(1-\rho)^{2/3}\rho^{1/3} \times (4N\pi/3n)^{1/3} + (P-p)(1-\rho) = 4\eta/3(dp/dt) \quad (7)$$

when we assume gel is sintered in conventional pressure, $P=0$, the equation becomes:

$$dp/dt = (1-\rho)(3\sigma/2\eta r - 3p/4\eta) \quad (8)$$

If there is no escape of gaseous water from the closed-pores, then combine Equation #4

$$dp/dt = (1-\rho)(3\sigma/2\eta r) - 3NRT\rho/4\eta \quad (9)$$

and let $dp/dt = 0$, and use Equation #3, then a critical pore radius r_{min} is obtained:

$$r_{min} = (3nRT/8\pi\sigma)^{1/2} \quad (10)$$

By substituting Equation #10 into Equation #9, then, an expression for the maximum value of density (ρ_{max}) is achieved:

$$\rho_{max} = 1/[(NRT/4\sigma)(3nRT/8\pi\sigma)^{1/2} + 1] \quad (11)$$

These two equations (#10,11) show that a maximum value ρ_{max} and a corresponding critical pore radius r_{min} can be predicted in terms of the sintering temperature (T), surface tension (σ), the amount of free water in a pore (n) and the number of pores per unit volume of silica (N/n). From this study the conclusion is reached that whenever the residual surface water is released after the collapse or closing of the original open-pores, then the free water in the gel structure follows the idea gas law at higher temperatures to create closed-pores. Consequently, foaming of the gel happens and the average radii of the pores increases significantly when temperature is just above 860°C

(see Figure 3-9). At 860°C the pore radius suddenly increases from a 1.1 nm open-pore radius to a 5.4 nm closed-pore radius.

X-ray diffraction patterns from fused silica generally exhibit a broad peak centered around the second strongest peak in the diffraction pattern of quartz (Figure 3-12). The partially densified silica gels made in this study have broader diffraction patterns than that of fused silica, as shown in Figure 3-12. The broadening of the gel diffraction peak decreases with increasing temperature, indicating an increase in the ordering inside the gel [74]. The BET data in Table 2-1 using Havard, Wilson, Iler's particle size model described in Section II also suggest that the effective particle diameter of the gels increases with temperature; e.g. 200°C (3.6 nm), 750°C (6.6 nm), 800°C (7.1 nm) and 860°C (15.7 nm) [75]. These values can be compared to the diameter around 100 nm of fully densified silica. These results imply that very short-range-ordering is taken place inside the structure forming crystallites. The size of a single silica tetrahedron is about 0.3 nm. Therefore, the structure of the gel crystallites is composed of only few silica tetrahedra. The gel preheated to 200°C is estimated to be about 8 tetrahedra, at 750°C it is about 15 tetrahedra, at 800°C it is about 17 tetrahedra, and at 860°C the gel has about 35 tetrahedra along the diameter of the gel fibrillar structure. As a result, x-ray diffraction produces a relatively broader peak for this relatively short-range-ordering than is observed for fused silica.

This observation led to the suggestion that the silica gel is composed of a randomly oriented fibrillar structure (random-network model [23]) in which the silica molecules are relatively ordered crystallites (crystallite model [23]). This phenomenon is similar to a "mosaic structure" in an imperfect crystal in which the lattice is broken up into a number of tiny blocks (about 1000 Å), each slightly disoriented one from another [74]. The overall observed gel structure is amorphous.

Based upon the above results, the structure of porous gel in which the temperature-independent pore diameter is always around 2.2 nm (see Table 2-1) is

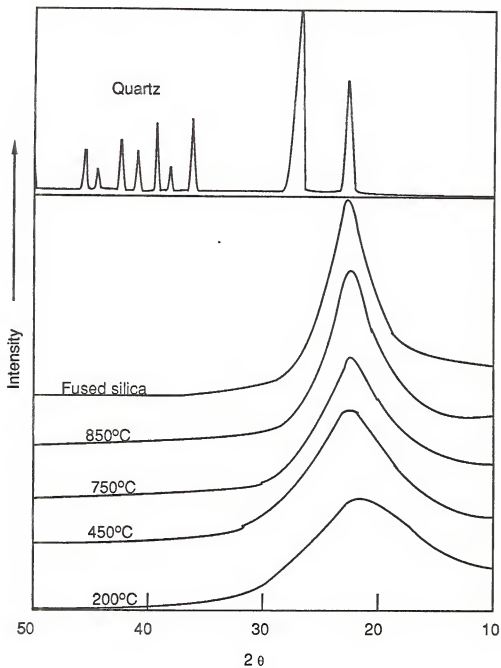


Figure 3-12 X-ray patterns of silica gels at different temperatures compare to that of fused silica.

proposed as shown in Figure 3-13. The ultrastructure of a densified gel is also proposed as shown in Figure 3-14.

The data obtained show that the index of refraction of the gel monoliths increases with the pyrolysis temperature as well as density. The measured index of refraction ranged from $n = 1.27 \pm 0.03$ to $n = 1.35 \pm 0.04$ for the sample heated from 150°C to 830°C , and the corresponding density varied from $1.40 \pm 0.02 \text{ g/cm}^3$ to $1.80 \pm 0.02 \text{ g/cm}^3$. Within experimental error the results shown in Figure 3-15 are reasonably well predicted by the Lorentz-Lorenz equation [see p. 658 in ref. 23]:

$$\alpha = [3 \epsilon_0 (n^2 - 1) M] / [N_0 (n^2 + 2) \rho] \quad (12)$$

Rearranging equation #12 yields:

$$(n_1^2 - 1) / [(n_1^2 + 2) \rho_1] = (n_2^2 - 1) / [(n_2^2 + 2) \rho_2] \quad (13)$$

where the constants are:

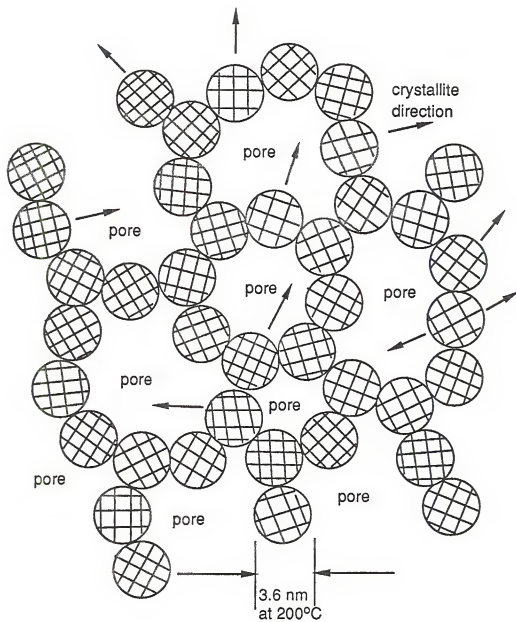
- α is polarizability of a silica molecule,
- ϵ_0 is the dielectric constant of a vacuum,
- M is the molecular weight of silica,
- N_0 is Avogadro's number,

and the variables are:

- n is index of refraction, ρ is density,
- n_1 is index of refraction of the gel and n_2 is that of fused silica,
- ρ_1 is density of the gel and ρ_2 is that of fused silica.

The results of Figure 3-15 show that it is possible that silica gel optics can be heated to specific temperatures to obtain a required combination of density and index of refraction. It is also possible that lenses can be obtained by controlling the temperature gradient in the silica gel to produce a refractive index gradient of refraction in a flat silica gel.

The differential scanning calorimeter (DSC) data, shown in Figure 3-16, indicate an endothermic desorption of physical water at a maximum 100°C in the 27.7°C to



Surface silanol groups are not shown

Figure 3-13 A proposed gel structural model.

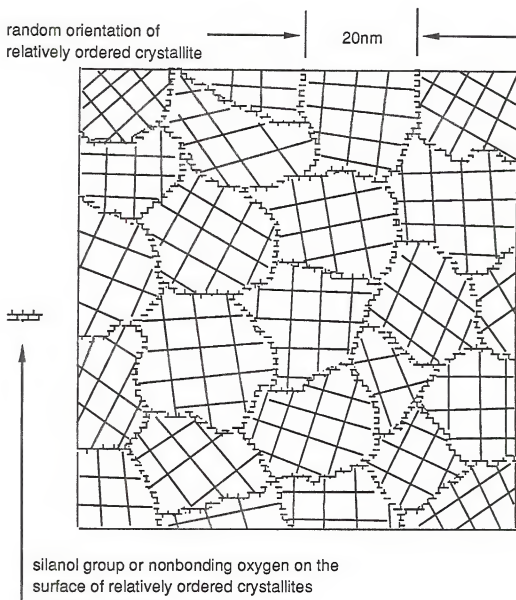


Figure 3-14 A proposed scheme of sintered silica gel in which silanol groups terminate bridging bonds on the surface of crystallites.

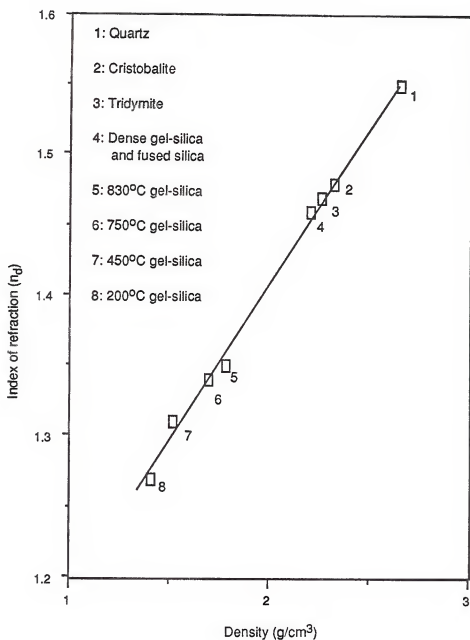


Figure 3-15 Index of refraction vs. density for silica gels, gel-glass, and crystalline phases.

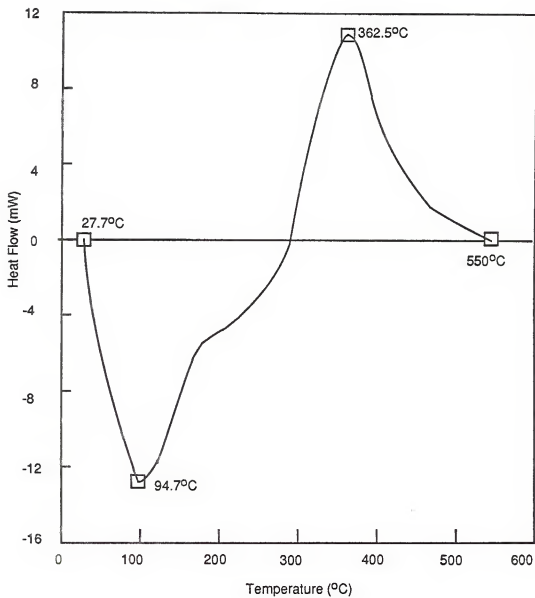


Figure 3-16 The differential scanning calorimeter (DSC) data of a dried silica gel.

200°C range and an exothermic decomposition and/or oxidation of oxalic acid at a maximum 362.5°C in the 200°C to 450°C range. The DTA data are collected via the same method as the DSC data, but DTA has an increased testing range to 1200°C, as shown in Figure 3-17. There is significant endothermic desorption of physical water within the pores. A very large exothermic decomposition and/or oxidation of oxalic acid is also observed with DTA. No further thermal sorption is observed in the range between 550°C and 1200°C. Thus, the dried and desorbed gels are stable from 550°C onwards.

A thermogravimetric analyzer (TGA) was also used to analyze the dried gel sample, as shown in Figure 3-18. In this case, the differential weight loss shows a very high peak at 124.0°C in the 25°C to 200°C range, indicating the maximum loss of physical water. There is a significant weight loss of oxalic acid at 361.3°C in the 300°C to 400°C temperature range; no further weight loss was observed from 450°C to 800°C. This TGA observation, together with DSC or DTA data obtained during sintering, clearly indicates that two phenomena are present; (1) the endothermic water evaporation in the range of 25°C to 200°C, and (2) the exothermic oxidation of oxalic acid in the 300°C to 400°C range.

Figure 3-19 illustrates two TMA curves, one of an unfired standard silica gel sample and one of a fired (540°C) sample; the curve of the unfired sample has a significant decrease in linear dimension from 200°C to 750°C. The preheated 540°C sample shows only a slight dimensional decrease (0.056%) when reheated to 540°C. When heated above 540°C the dimensions decreases noticeably. These results show that the structure of the fired sample has already undergone rearrangement and that it is irreversible.

In a 3-point bending test, a beam loaded has tensile stresses on one surface and compressive stress on the other, as shown in Figure 3-20. Flexural strength is a measure of the level of the tensile stress on the surface required to make a material fail. A partially densified gel is like fully densified glass which shows no plastic deformation

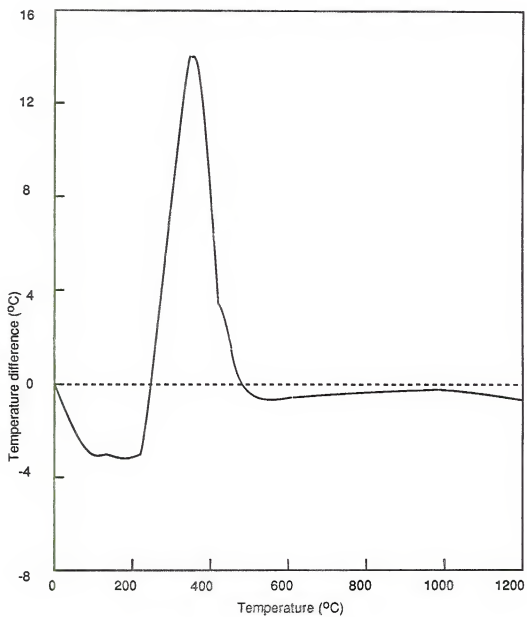


Figure 3-17 The differential thermal analysis (DTA) data of a dried gel.

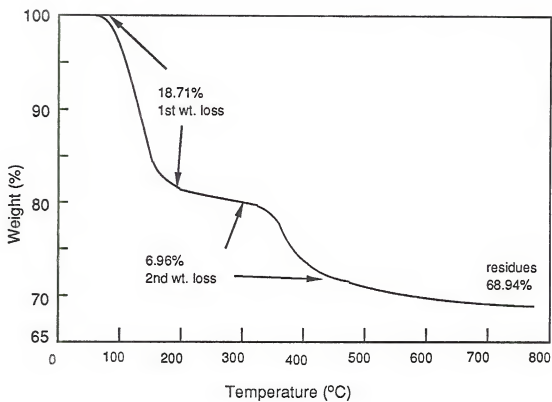


Figure 3-18 Thermogravimetric analysis (TGA) curve of a dried gel.

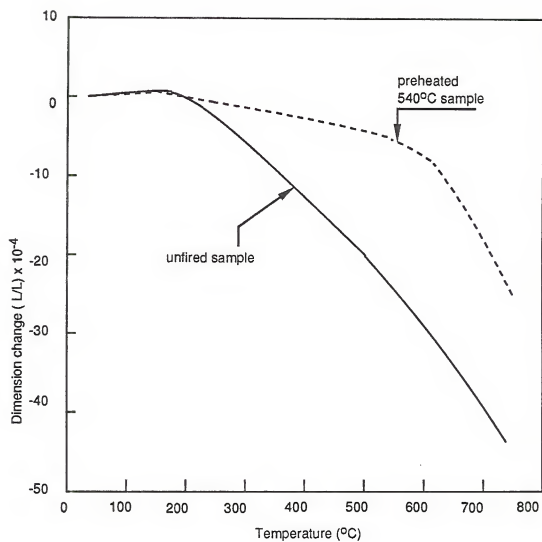


Figure 3-19 Thermal mechanical analysis of a unfired sample and a preheated sample.

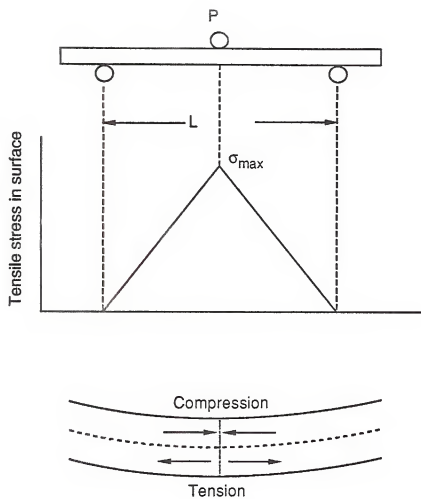


Figure 3-20 A three-point bending test.

under the stress. Samples can be loaded and stressed up to the proportional limit (rupture point at a maximum tensile stress σ_{\max}). Elastic strain is directly proportional to the applied tensile stress, σ , by following the Hooke's law ($\sigma = E \epsilon$ where σ is tensile stress, E is Young's modulus of elasticity for bending test, ϵ is elastic strain. See ASTM D 790M - 84) and is recoverable below σ_{\max} . In this test, the load to failure was calculated using the equation [see p. 156-158 in ref. 63]:

$$\sigma = 3P_1 L / 2bd^2 \quad 0 \leq \sigma \leq \sigma_{\max} \quad (14)$$

where

σ : tensile stress on the outer surface at midspan, pascal (newton/m²),

P_1 : load at a given point on the load-deflection curve, N (newton),

L : support span distance, m,

b : width of specimen, m, and

d : thickness of specimen, m.

the elastic strain before or at fracture was obtained using equation [69]:

$$\epsilon = Z t = 6 R t d / L^2 = 6 D d / L^2 \quad 0 \leq \epsilon \leq \epsilon_{\max} \quad (15)$$

where

ϵ : strain, mm/mm, ϵ_{\max} is the maximum strain at σ_{\max}

Z : strain rate, mm/sec,

t : time, sec,

R : rate of crosshead motion, mm/min,

D : midspan deflection, mm.

The variation of maximum flexural strength (σ_{\max}), maximum strain (ϵ_{\max}), Young's modulus of elasticity ($E = \sigma_{\max}/\epsilon_{\max}$) with standard deviations for each set of five samples prepared at different temperatures are listed in Table 3-2 and shown in Figures 3-21, 3-22, 3-23. A large increase in flexural strength was noted above 700°C (Table 3-2, Fig. 3-21). The specimen heated to 830°C has a value of about 30.4 MPa which is about half the value of fused silica glass (58.9 MPa) [76]. The obtained

Table 3-2
Mechanical properties of partially densified silica gels and fused silica

Temperature °C	Flexural strength σ_{\max} (MPa)	Maximum strain ϵ_{\max} , ($\Delta L/L \times 10^{-6}$)	Young's modulus MPa
150	08.4 ± 0.5	1060 ± 201	07925
250	09.8 ± 0.7	1071 ± 178	09148
450	11.8 ± 1.2	980 ± 94	12035
750	25.0 ± 2.3	876 ± 157	28539
800	27.0 ± 2.6	833 ± 150	32413
830	30.4 ± 3.6	826 ± 121	36803

***For reference [76]:

fused silica	58.9	806	73089
--------------	------	-----	-------

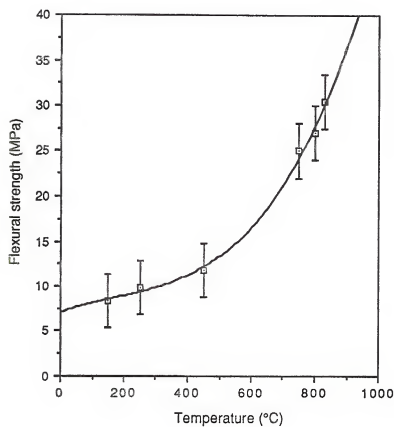


Figure 3-21 Flexural strength versus temperature.

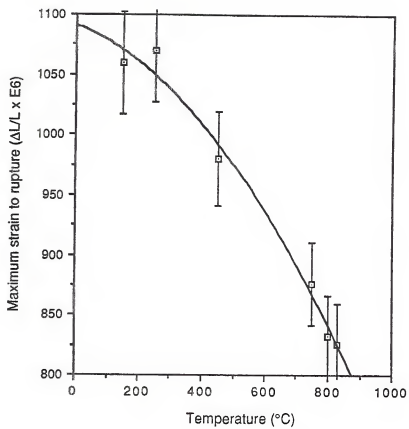


Figure 3-22 Maximum strain to rupture versus temperature.

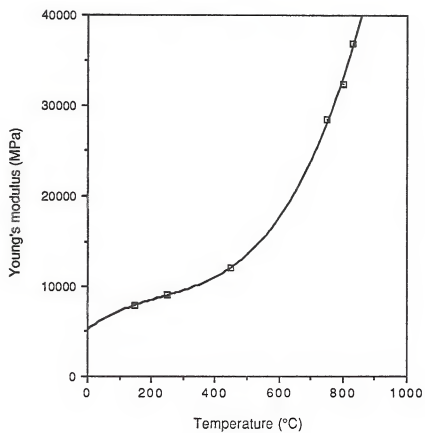


Figure 3-23 Young's modulus versus temperature.

maximum strain to the point of rupture for the gel samples decrease to approach the value, 806×10^{-6} of vitreous silica (Table 3-2, Fig. 3-22). It is concluded that the gels have higher elastic deformability than fused silica since the fibrillar gel structure can endure relatively higher dimensional deformation before rupture. Because of the low densities of the porous gels, the Young's moduli calculated from equation $E = \sigma_{\max}/\epsilon_{\max}$ are much lower than the 73089 MPa [76] value of fused silica. However, the Young's modulus increases and approaches the value of fused silica as the densification temperature increases (Table 3-2, Fig. 3-23). We should also notice that it is very difficult to achieve a highly polished surface for partially densified gel-glasses. Consequently, relatively lower values with wider standard deviations are expected.

The test results (Figure 3-24) show that the compressive strength increases gradually with temperature and reaches a value of 556 MPa at 830°C, approximately half the value of vitreous silica glass (1108 MPa) [76].

The density of the silica gels and gel-glasses are plotted as a function of firing temperature in Figures 3-25, with density increasing as the densification temperature increases. Only small changes in density were observed below 500°C; however, above 700°C the density increased considerably with processing temperature. This indicates that viscous sintering is initiated above this temperature. The density of the samples heated to 830°C is about $1.80 \pm 0.05 \text{ g/cm}^3$ — approximately 82% the density of fused silica glass. The temperature required to reach a density equivalent to type I-IV silica is a function of the ultrastructure of the gel itself, ranging from 830°C to 900°C, depending on particle size and the residual water content of the solid.

The results of a diamond point microhardness test for silica gel as a function of pyrolysis temperatures are given in Table 3-3 and Figure 3-26. For a constant load (0.05 Kg), the length of the indentation diagonal decreases as the temperature and the microhardness increases. The 830°C gel sample has a microhardness value of 245 Kg/mm² which is about three times less than the 710 Kg/mm² value of fused silica. The

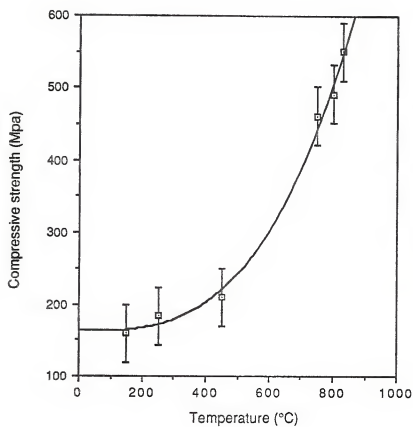


Figure 3-24 Compressive strength versus temperature.

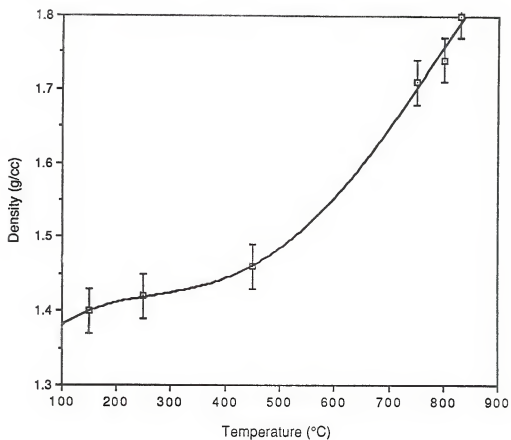


Figure 3-25 Density versus temperature.

Table 3-3
Microhardness data of partially densified silica gel
(0.05 Kg load)

Temperature (°C)	Indentation Diagonal length d, (mm)	Microhardness DPN (kg/mm ²)
150	0.0202 ± 0.0040	113 ± 27
250	0.0193 ± 0.0054	125 ± 38
450	0.0182 ± 0.0032	140 ± 43
750	0.0154 ± 0.0024	196 ± 52
800	0.0145 ± 0.0025	220 ± 35
830	0.0138 ± 0.0030	245 ± 49

***Vickers' hardness number for silica is 710 kg/mm² [see p. 144 in ref. 63].

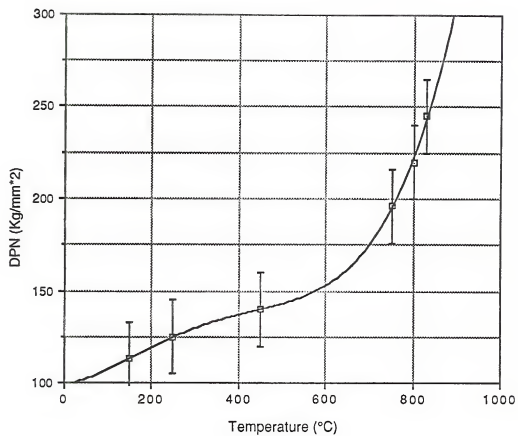


Figure 3-26 Microhardness vs. temperature

slope of the curve in Figure 3-26 becomes very sharp at about 700°C indicating a significant structural change in gels.

Fracture toughness indicates the amount of energy absorbed by a material during failure. This is in contrast to flexural strength (σ_{\max}), which is a measure of the stress required to break a material. A tougher material can absorb more energy within the structure before rupture occurs. The critical stress intensity factor, K_{IC} , can be estimated from the length of the plastic zone ahead of the crack tip. A simple testing procedure and economical method, using a Vickers diamond pyramid indenter, was introduced by S. Palmqvist [77] and evaluated by Anstis [64]. Although the determination of K_{IC} by this method is not unique, the experimental relationship established by Anstis is given below:

$$K_{IC} = 0.016 (E/H)^{1/2} P_2/(c/2)^{3/2} \quad (16)$$

where

E : elastic modulus in pascals,

H : microhardness in $\text{Kg/cm}^3 = 2P_2 \sin 68^\circ/d^2$ [see p. 143-149 in ref. 63],

P_2 : indentation load in kg,

68° : the half angle between opposite faces of the four-sided pyramid of diamond indenter.

d : diamond point indentation diagonal length, mm,

c : extended crack length, μm .

The experimental data (density, Young's modulus, microhardness and extended crack length) and the calculated results (K_{IC} and K_{IC}/ρ) are compared to the values of vitreous silica, as listed in Table 3-4. The low K_{IC} value ($0.72 \text{ MPa}\cdot\text{m}^{1/2}$) of fused silica glass indicates its brittle character. None of the silica gel samples has a higher K_{IC} value than fused silica. This shows that the gel samples are even more brittle and easier to break than fused silica. Surprisingly, the 150°C gel ($0.49 \text{ MPa}\cdot\text{m}^{1/2}$) is fairly tougher than the 830°C gel ($0.40 \text{ MPa}\cdot\text{m}^{1/2}$). If the K_{IC} value is divided by the density

Table 3-4
Fracture toughness (K_{Ic}) and K_{Ic}/ρ ratio of partially densified silica gels, data
obtained from diamond indentation cracks.
(0.05 Kg load)

Temp. T (°C)	Density ρ (*g/cm ³)	Modulus E (MPa)	Microhardness H (***Kg/cm ²)
150	1.40 ± 0.05	7925	11300 ± 2700
250	1.42 ± 0.05	9148	12500 ± 3800
450	1.46 ± 0.05	12035	14000 ± 4300
750	1.71 ± 0.05	28539	19600 ± 5200
800	1.74 ± 0.05	32413	22000 ± 3500
830	1.80 ± 0.05	36803	24500 ± 9800
fused silica	2.20	73089	71000

Temperature T (°C)	Extended Crack Length c ** μm	Toughness K_{Ic} *** MPa·m ^{1/2}	K_{Ic}/ρ
150	24.3 ± 5.8	0.49	0.35
250	27.0 ± 3.8	0.43	0.30
450	30.6 ± 3.2	0.39	0.27
750	32.2 ± 5.1	0.47	0.27
800	35.0 ± 9.7	0.42	0.24
830	35.9 ± 4.3	0.40	0.22
fused silica	21.5	0.72	0.33

* 1Kg = 1000 g.

** 1 μm = 10^{-6}m = 10^{-4}cm = 10^{-3}mm ,

***10.194 Kg/cm² = 1 MPa = 145 psi.

of samples, the 150°C gel sample has a value 0.35 which is even greater than the value of 0.33 of fused silica. The reason is probably due to the fibrillar ultrastructure of the low temperature gel which is described in Figure 2-36, Chapter 2.

Mechanical properties of the silica gels and gel-glasses, including flexural strength, compression strength, microhardness, and toughness, are all dependent on the gel ultrastructure. The evolution of ultrastructure, monitored by N₂ adsorption-desorption isotherms, FTIR, uv-vis-nir, and x-ray diffraction techniques, proves that the pore volume, the surface area, and the amount of nonbridging oxygens (surface silanol group) decreases and the effective particle size increases with an increase in pyrolysis temperature. Consequently, the overall bulk density increases with sintering temperature, representative of the degree of ultrastructural rearrangement. In Figures 3-27, 3-28, 3-29, 3-30, 3-31, and 3-32, the experimental data of compressive strength, maximum strain to failure, flexural strength, Young's modulus, microhardness, and toughness are plotted as a function of density. The maximum density of 2.2 g/cm³ represents the value of vitreous silica. Within experimental error, the mechanical properties are linearly related to the density. A simple relationship is:

$$X_{\text{gel}} = X_s (\rho_{\text{gel}}/\rho_s) \quad (17)$$

where

X_{gel} : mechanical properties of the partially densified gel (i.e. compressive and flexural strength, Young's modulus, and microhardness),

X_s : mechanical properties of vitreous silica,

ρ_{gel} : density of the partially densified gel,

ρ_s : density of vitreous silica, 2.2 g/cm³.

Dashed lines drawn in Figure 3-27, 3-29, 3-30, and 3-31 were obtained from the above relationship. Although the present experimental results do not fit those predicted by equation 17, a linear relationship can still be applied to the present

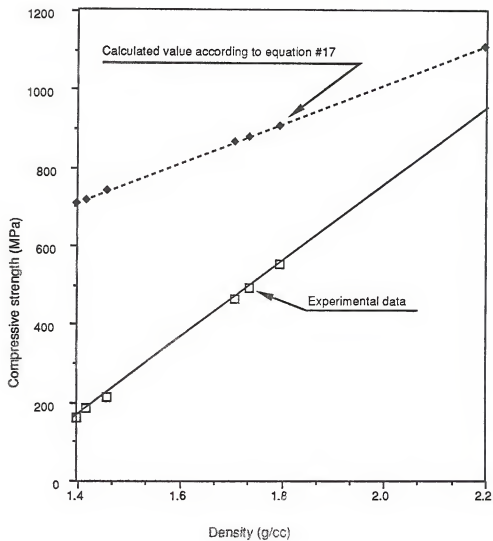


Figure 3-27 Compressive strength versus density.

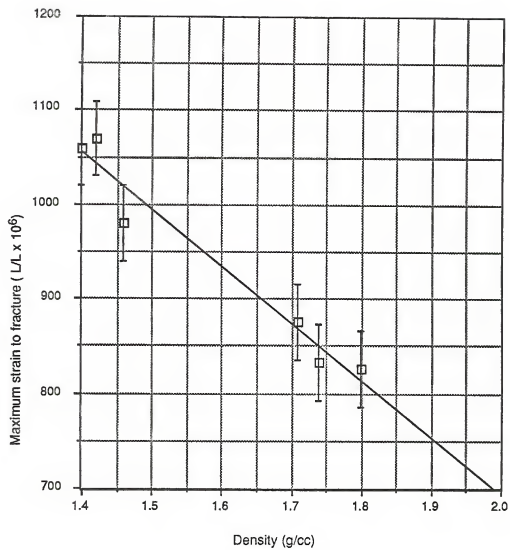


Figure 3-28 Maximum strength to failure versus density.

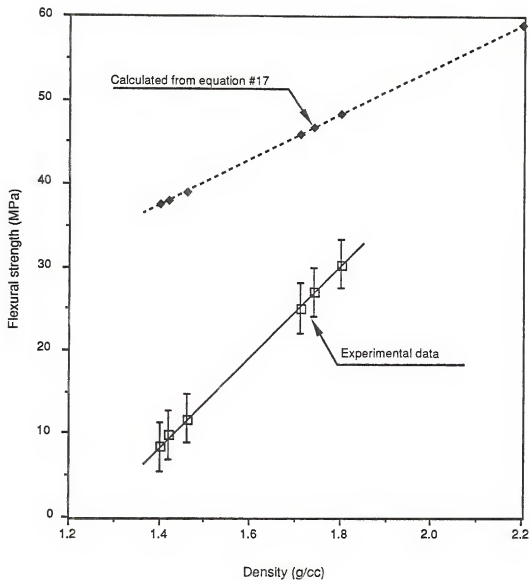


Figure 3-29 Flexural strength versus density.

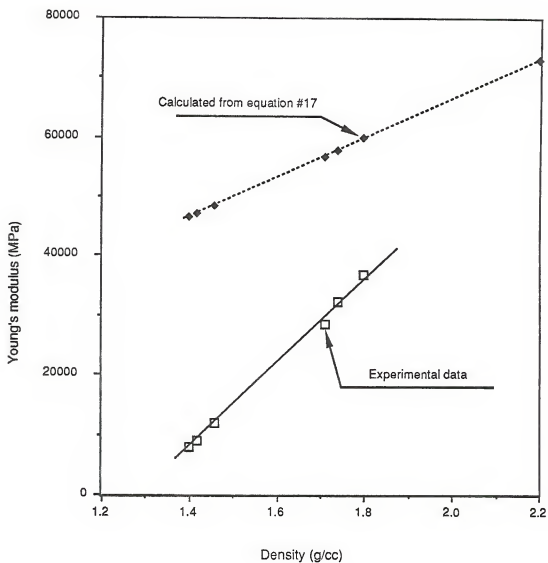


Figure 3-30 Young's modulus versus density.

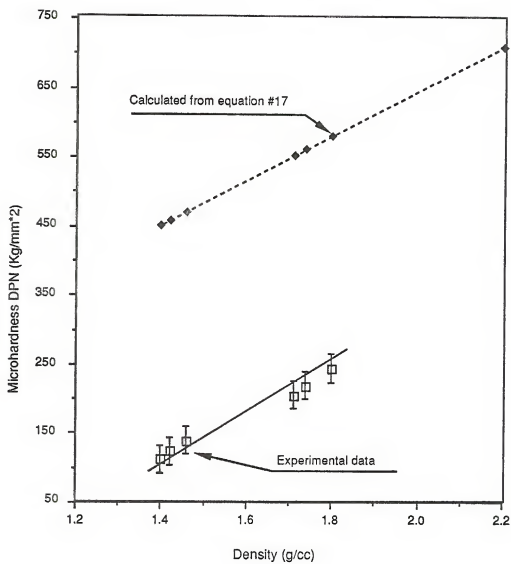


Figure 3-31 Microhardness versus density.

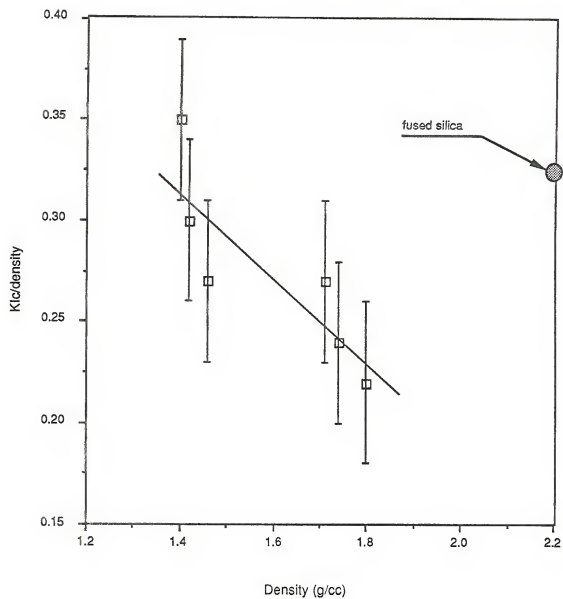


Figure 3-32 Toughness versus density.

experiment.

Several models [see p. 773-777 in ref. 23] have been developed to predict the Young's modulus of a two phase system, such as a partially sintered gel-glass. The first is the Voigt model which assumes that the strain in each phase is the same; therefore, the Young's modulus of this two phase system is expressed as $E_{upper\ bound} = V_2 E_2 + (1 - V_2) E_1$ where V_2 is the volume fraction of the phase with modulus E_2 , and E_1 is the modulus of the other phase. The second is the Reuss model which assumes that the stress in each phase is the same; therefore, the modulus of this two phase system can be expressed as $1/E_{lower\ bound} = V_2/E_2 + (1-V_2)/E_1$. Z. Hashin and S. Shtrikman have established upper and lower limits for the moduli which are much narrower than the Voigt and the Reuss models.

Ultimately, the second phase in a material can be considered as pore spaces that have zero Young's modulus value. This model was developed at porosities (closed pores) up to about 50% by J. K. Mackenzie and expressed as $E/E_0 = (1 - 1.9P + 0.9P^2)$ where P is porosity, and E_0 is the modulus of the matrix phase. This is a much more reliable model compared to the first three models in dealing with porous material. Porous gel can be treated as a two-phase material in which the second phase is porosity. Consequently, it seems reasonable to use this model to predict the Young's modulus of the porous gel. The Young's modulus of the gels obtained from experiment are compared with the values from Mackenzie's model as shown in Figure 3-33.

The experimental values of Young's moduli for the gels are generally lower than the predicted values. The deviations between them at lower densities are larger than that at higher densities. This may be due to the high surface water content in the lower density gels which promotes crack propagation [24]. As the gel becomes denser, the number of pores decreases and the surface water is reduced. Therefore, in the higher density region, the experimental data become closer to the values the above equation predicts.

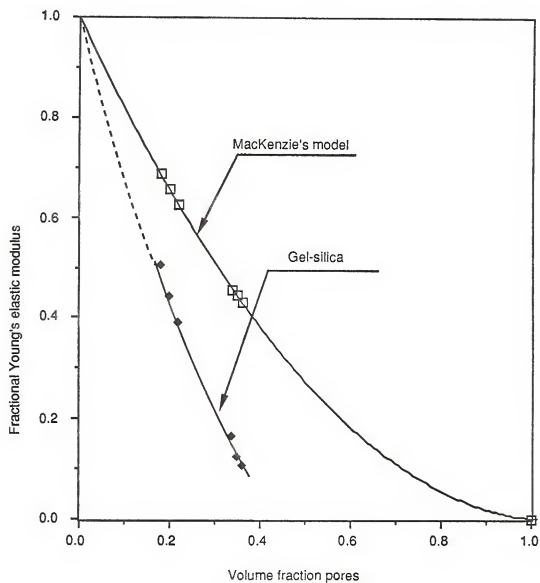


Figure 3-33 Relative Young's modulus versus porosity.

Conclusions

The determination of the physical properties of partially densified gels establishes the nature of the porous gel ultrastructure and ultrastructural dependence of properties.

FTIR analysis showed a 950 cm^{-1} SiOH stretching vibration peak decreasing with increasing temperature, indicating that the sample is becoming increasingly dehydrated. The peaks of organic residuals in the range from 2000 cm^{-1} to 3000 cm^{-1} disappear as temperature increases. The shift to lower UV cut-off wavelengths with increasing temperature, noted in the UV-VIS-NIR data, also shows that the impurity (water) level is reduced. A quantitative study on the change of water level during sintering is discussed in Chapter 4.

X-ray diffraction of the gels showed no evidence of devitrification, confirming the development of an amorphous glass phase from the gel. More important in this study, the observation led to suggestion that silica gel is composed of random oriented fibrillar structure (random-network model) in which the silica molecules are very well ordered crystallites (crystallite model).

The Index of refraction of silica gel varied with density as predicted by the Lorentz-Lorenz relationship. This variation of refractive index with density can be utilized to manufacture optical waveguides and lenses using localized index gradients.

BET data showed a uniform size distribution of porosity for all temperatures below the fully densified temperature. The densification mechanism reduces the volume and number of pores, as opposed to pores merging together without reduction in pore volume.

The DSC, DTA, TGA, and TMA data provide information useful in monitoring thermodynamic, weight loss, and dimensional changes during sintering. With these data an optimized manufacture process can be achieved.

Mechanical properties, including flexural and compressive strength, microhardness, together with density, showed an increase in values with increasing

processing temperature approaching the values of vitreous silica. The low toughness, K_{Ic} and K_{Ic}/ρ , values of the partially densified gels are comparable to those of Type I-IV vitreous silicas. The interesting point is the 150°C gel sample has a higher K_{Ic}/ρ value than fused silica confirming that the fibrillar ultrastructure of the gel can absorb relatively high energy before rupture occur. The presence of surface water is suggested to be a major deteriorating factor for the mechanical properties, and is especially severe in the lower temperature gels.

CHAPTER 4 DEHYDRATION OF SOL-GEL DERIVED SILICA OPTICS

Introduction

An amorphous silica gel can be characterized by a random packing of SiO_2 tetrahedra which gives rise to a nonperiodic, solid, fibrillar structure with many voids and a very large surface area. The surface area ranges from $500 \text{ m}^2/\text{g}$ to $900 \text{ m}^2/\text{g}$ depending on the low temperature sol-gel processing schedule.

Based on Iler's study, silica gel consists of connected spherical particles; the interior of the particles have a density of 2.2 g/cm^3 made entirely of anhydrous $-\text{O}-\text{Si}-\text{O}-\text{Si}-$ bridging bonds. Located on the particle's surface are non-bridging terminal oxygens, each having an attached hydroxyl ion; these are also referred to as silanol groups. As a wet silica gel is dried, or partially densified, free water is removed from the pores; however, the silanol groups remain intact [78, 79].

Theoretically, for ultrapure silica without silanol groups the energy gap between the valence and conduction bands is approximately 8.9 eV , as the oxygen ions have very tightly bound electrons [80]. The high intrinsic absorption edge results from the excitation of the valence band electrons within the bridging $\text{Si}-\text{O}$ network to unoccupied higher energy states, such as exciton levels or conduction band levels [see p. 161-164 in ref. 26]. To excite these electrons requires ultraviolet photons of at least 140 nm wavelength (or wavenumber $= 71428 \text{ cm}^{-1}$). Thus, the UV absorption peak for ultrapure silica should occur at approximately 140 nm and its UV absorption tail, which is associated with thermally activated phonons [81], becomes negligible in the visible-infrared portion of the spectrum.

The intrinsic fundamental vibrations of the ultrapure silica molecules result in resonance with the incoming light at an infrared absorption peak of 8333 nm (1200 cm^{-1} , 0.149 eV); however, weak combination and overtone bands exist at 3200 nm (3125 cm^{-1} , 0.39 eV) and 3800 nm (2632 cm^{-1} , 0.33 eV), and strong bands occur at 4400 nm (2273 cm^{-1} , 0.28 eV). The infrared absorption tail of ultrapure silica, like its UV absorption tail, is also caused by phonons. These combinations and overtones influence the infrared absorption tail down to 1300 nm (7692 cm^{-1} , 0.95 eV) [82].

Extrinsic absorption of light in silica gel in the 140 nm to 8333 nm range has been detected and interpreted as essentially the result of surface hydroxyl groups and their associated free water; only one ppm of hydroxyl ions in glass can produce 30 dB/km loss at 1390 nm [83]. All other types of impurities have been reduced to very low levels (only several parts per billion) by a chemical refining system during TMOS synthesis, thereby contributing no significant absorption effects in these gels.

Thus, a major problem in producing gel-silica optics is that gel surface hydroxyl groups and hydrogen-bonded pore water give rise to atomic vibrational energy absorption in almost the entire range of ultraviolet to infrared wavelengths (160 nm to 4500 nm). This absorption greatly decreases the optical applications of a silica-gel monolith. Consequently, in order to achieve the full theoretical performance of silica complete dehydration is imperative. The degree of dehydration of gel-silica optics is monitored by analyzing the light absorption spectra in a broad range; the Perkin-Elmer UV-VIS-NIR spectrophotometer covers the range from 184.5 nm (54200 cm^{-1}) to 3200 nm (3125 cm^{-1}) and the Nicolet FTIR covers the range from 2083 nm (4800 cm^{-1}) to 50,000 nm (200 cm^{-1}).

After extensive experimentation a reliable method was found that completely eliminates the surface chemical hydroxyl groups and associated pore water in gel-silica monoliths. By applying the concepts of fundamental silica surface chemistry [84-86], it was found that many chlorine compounds – some of these include methylated

chlorosilanes, such as $\text{ClSi}(\text{CH}_3)_3$, $\text{Cl}_2\text{Si}(\text{CH}_3)_2$, $\text{Cl}_3\text{Si}(\text{CH}_3)$, silica tetrachloride (SiCl_4), chlorine (Cl_2) and carbon tetrachloride (CCl_4) – can completely react with surface hydroxyl groups to form hydrochloric acid, which then desorbs from the gel body at a temperature range (400°C to 800°C) where the pores are still interconnected. In this study, carbon tetrachloride is used successfully to achieve complete dehydration of ultrapure gel-silica monoliths.

Review of the Literature Regarding Dehydration

The quality of silica gel can be significantly reduced by impurities. By far the most troublesome impurity, "water", is present in two forms: free water within the ultraporous gel structure (i.e., physical water), and hydroxyl groups associated with the gel surface (i.e., chemical water). The amount of physical water adsorbed to the silica particles is directly related to the number of hydroxyl groups existing on the surface of silica. During the 1950's and 1960's, researchers Young, Friplat, Benesi and Jones, Hockey and Pethica, Kiselev, McDonald, et al. [87-91] contributed much information regarding the hydration/dehydration characteristics of the silica gel/water system, as summarized below:

1. The physical water can be eliminated and surface silanol (Si-O-H) groups condensed starting at about 170°C , as shown in Figure 4-1. Thermal analyses, such as TGA and DSC, confirmed this process in our silica gel system, as shown in Chapter 3.
2. The dehydration is completely reversible, up to about 400°C , as shown in Figure 4-2. Decomposition of organic residuals, up to 400°C , was also confirmed using DSC and TGA for our TMOS derived silica gels, as presented in Chapter 3.
3. Above 400°C , the dehydration process is irreversible as a result of shrinkage and sintering across pores, as shown in Figure 4-3. Thus, the amount of existing hydroxyl groups on the gel surface is an inverse function of the temperature of

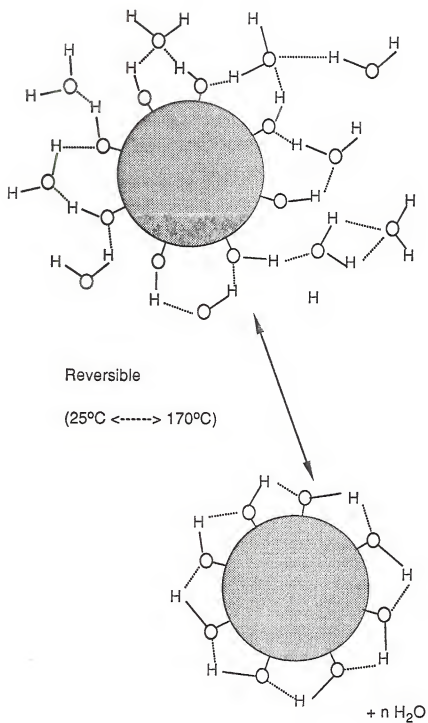


Figure 4-1 Physical water decreases and silanol groups condense in the range of room temperature and 170°C.

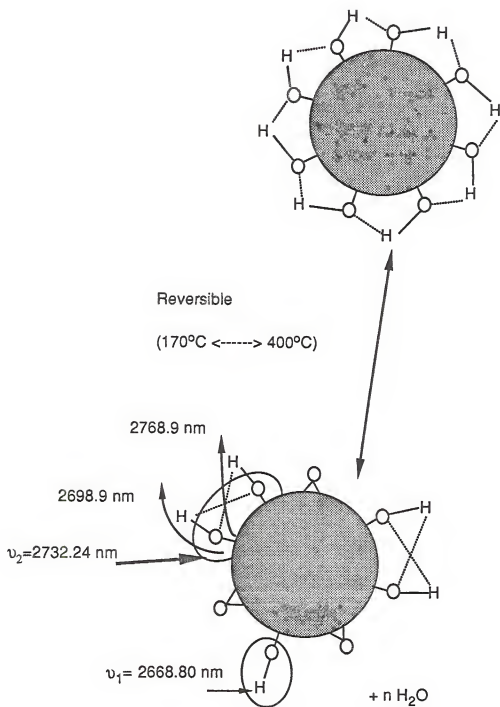


Figure 4-2 Surface silanol groups are reversible in the range of 170°C to 400°C.

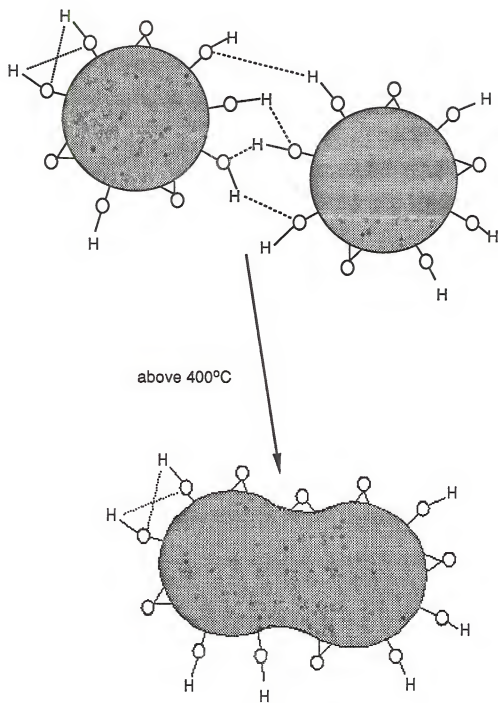


Figure 4-3 Irreversible elimination of adjacent hydroxyl groups.

densification. It is shown in Chapter 3, based upon UV-VIS-NIR data, that the reduction of surface hydroxyl groups occurs above 400°C.

4. Viscous flow occurs above 850°C with the exact temperature depending on the particle size of a specific gel. The singular hydroxyl groups on the gel surface react with each other bringing particles together, thereby eliminating voids within the gel. Some surface water, which is unable to be desorbed prior to pore closure, is trapped inside the densified gel.

Young, in his early work, found that the decrease in surface area of the silica gel at high temperatures is a function of the time and temperature of the heat treatment. This supports the concept that the sintering mechanism is essentially the result of viscous flow, rather than surface diffusion. Impurities (i.e., surface water) effectively lower surface energy and thereby the sintering temperature, presumably by facilitating viscous flow; Zarzycki, et al. [73] confirmed this point.

Hair [see p. 87 in ref. 27] also proved that heating silica gel in the 170°C to 400°C range causes reversible dehydration via elimination of surface water and the formation of both single and adjacent surface hydroxyl groups, as illustrated in Figure 4-2. Hair found that at 400°C, no more than half of the surface hydroxyl groups had been desorbed and that most of the remaining surface hydroxyl groups were adjacent to each other and therefore situated for preferential water adsorption, shown in Figure 4-4. He stated that heating the gel above 400°C causes a drastic, irreversible elimination of adjacent hydroxyl groups, as shown in Figure 4-3, until at about 800°C, only single hydroxyl groups remain, as shown in Figure 4-5. As the temperature increases, single hydroxyl groups depart from the gel surface until the gel is densified; this occurs in the 850°C to 1000°C range. However, some single hydroxyl groups are still unable to escape from the gel surface and therefore can contribute to foaming of the gel as the temperature increases.

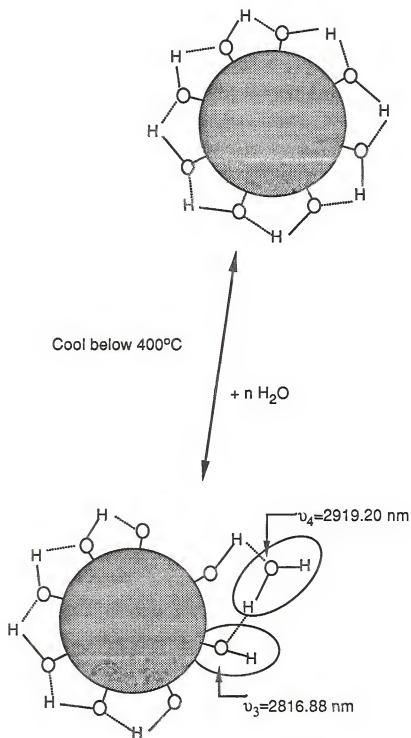


Figure 4-4 Reabsorption of physical water below 400°C.

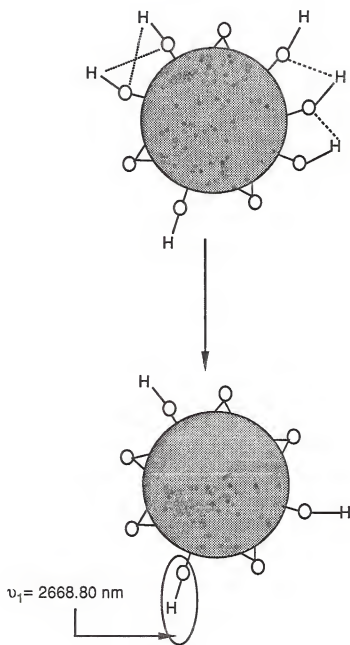


Figure 4-5 Only single hydroxyl groups remain at temperature above 800°C

More importantly, Hair mentioned that when the silica gel has been completely dehydrated, there are no surface hydroxyl groups to adsorb the free water; in other words, the surface is essentially hydrophobic. Clearly, it is the realization of this critical point that is the focus for this study.

The vibrational overtones and combinations of hydroxyl groups and their associated molecular water, occurring in the 1250 nm to 3000 nm range, have been studied by Anderson and Wickersheim [92]. Evaluation of a partially dehydrated (800°C) silica gel shows an absorption peak at $\nu_1 = 2668.80$ nm (see Fig. 4-5), surely due to the fundamental stretching vibration of hydroxyl groups on the gel surface. These singular, or free, hydroxyl groups are also referred to as "isolated silanol groups". The symmetrical appearance of this peak indicates that these singular hydroxyl groups have no interaction with water molecules. The band at 1366.12 nm ($2\nu_2$) is the first overtone of the adjacent silanol group vibration $\nu_2 = 2732.24$ nm (see Fig. 4-2). The 1366.12 nm peak becomes less intense as the gel is heated and disappears with complete dehydration. The combination peak at 2207.51 nm ($\nu_2 + \nu_{OH}$ (bend)) is the result of the hydroxyl ion's stretching and bending vibrations, where ν_{OH} is a bending wavelength between 11494.25 nm and 12345.67 nm. Researcher Peri [93] suggests that this combination band is due to the Si-O-H stretching vibration and an out-of-plane O-H displacement (bending) vibration. This type of hydroxyl group is labeled an OH(2) group.

The adjacent hydroxyl groups also interact with free water (ν_3 , see Fig. 4-4) to form hydrogen bonds; this effect causes a change in both the fundamental stretching vibration and its associated overtones and combinations. Therefore, the hydroxyl groups associated with water show a new combination peak at 2262.44 nm ($\nu_3 + \nu_{OH}$ (bend)); this kind of hydroxyl group is called OH(3). The energy calculations, by Benesi and Jones [88], predict that the fundamental stretching vibration of OH(3) at $\nu_3 = 2816.88$ nm is a value shifted about 148.08 nm from the vibration of the free hydroxyl group at

$\nu_1 = 2668.80$ nm (OH(1)). From actual absorption data, McDonald observed a peak at 2816.88 nm, indicating a strong interaction between free pore water and surface hydroxyl groups.

When a dehydrated silica gel is exposed to a slightly humid air atmosphere, sharp peaks appear at 2816.88 nm (ν_3), 2732.24 nm (ν_2), 1890.35 nm ($\nu_3 + 2\nu_{OH}$ (bend)), 1459.85 nm ($2\nu_4$), and 1408.44 nm ($2\nu_3$). Hair [see p. 89 in ref. 27] believes that the intensity changes upon adsorption of water indicate that all these bands are connected with the hydroxyl group which is associated with physical pore water. Further hydration results in a broadened band at about $\nu_4 = 2919.70$ nm (see Fig. 4-4) --characteristic of bulk water.

Cant and Little [94, 95], and Chapman and Hair [96], tend to agree that for silica gel a sharp and slightly asymmetrical peak on the high-wavelength side, at 2668.80 nm (ν_1), together with a distinct band at 2732.24 nm (ν_2), can be attributed to freely vibrating surface silanol groups, and to hydrogen-bonded adjacent silanol groups, respectively. In addition, a broad band at 2919.70 nm (ν_4) is due to the stretching of molecular water.

Elmer, et al. [97], in their rehydrated study of porous silica showed that the intensity of the peak at 2668.80 nm increases during rehydration. They also indicated that physical water prefers to adsorb on adjacent hydroxyl groups rather than on the singular hydroxyl groups.

Recent studies in optical fiber communication technology by D. B. Keck, R. D. Maurer, and P. C. Schultz [71] found that the extrinsic hydroxyl groups also give rise to some noticeable overtones and combinations occurring roughly at 725 nm, 880 nm, 950 nm, 1125 nm, 1230 nm, 1370 nm. These absorptions strongly degrade the performance of optical fibers.

Most of the silica glasses manufactured by melt or synthetic methods (Type I to IV silicas stated in Chapter 1), such as those produced by Corning, Melles Groit, Dynasil,

and Quartz Scientific, Inc., result in impurities (e.g., water and/or metallic elements). Three significant absorption peaks at 2732.24 nm (ν_2), 2207.51 nm ($\nu_2 + \nu_{OH(bend)}$) and 1366.12 nm ($2\nu_2$) are found to be the unique stretching vibration of adjacent silanol groups and its overtone and combination, as shown in Figures 4-6, 4-7, 4-8, and 4-9. No singular silanol group (ν_1) was found using high resolution UV-VIS-NIR spectrophotometer.

The electrons of these impurity atoms can be easily excited by photons of lower energy than those associated with the 8.9 eV UV band edge of theoretically pure silica, thereby causing a shift in the ultraviolet absorption edge to longer wavelengths. These excitations also cause additional absorption bands or peaks in the visible and near infrared ranges. Without complete dehydration, the quality of silica gel-glasses is significantly affected by the problem of water retention.

The highest quality of pure silica manufactured in the world today is that of optical fibers fabricated by vapor phase reaction of pure oxygen with silicon tetrachloride (Type IV silica). This process results in fibers of ultralow loss — about 1.0 dB/km to 5.0 dB/km in the 900 nm to 1300 nm range. It is shown in Chapter 5 that the fully dehydrated, completely densified, gel-glass monoliths developed in this dissertation are of such a quality as to compare with optical fibers.

Experimental Procedure

The standard dried gels (150°C), manufactured as per Example One in Chapter 2, are used as the basis for preparing two sample sets for the following dehydration study. One sample set was partially densified at designated temperatures in an ambient air atmosphere; the other set was chemically and thermally treated prior to sintering in a mixed vapor (carbon tetrachloride and helium) atmosphere within a special apparatus, shown in Figure 4-10.

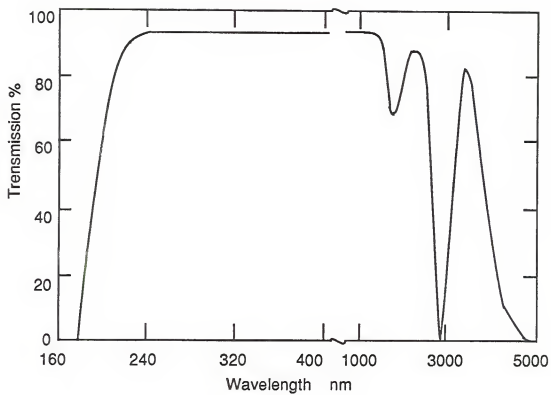


Figure 4-6 Transmission curve from Corning Glass Co. commercial UV grade optical melt silica Code 7940. Thickness 10 mm.

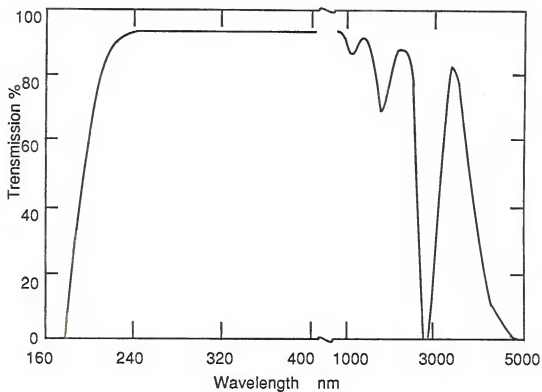


Figure 4-7 Transmission curve from Melles Griot Co. commercial UV grade optical melt silica Code UVGSFS. Thickness 10 mm.

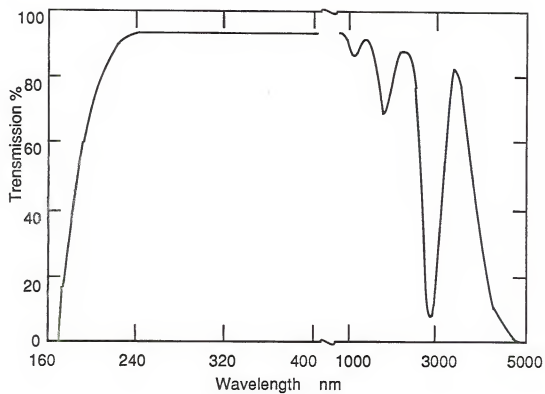


Figure 4-8 Transmission curve from Dynasil Co. commercial UV grade optical melt silica Code 1000. Thickness 10 mm.

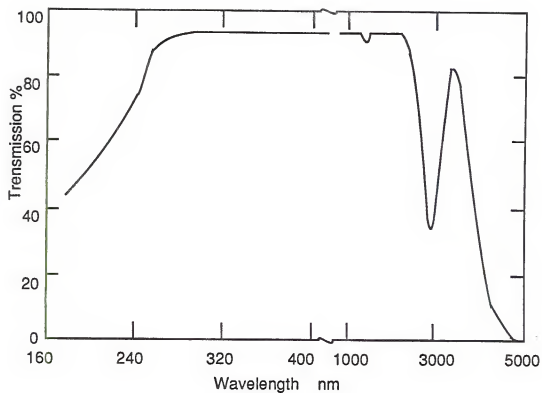


Figure 4-9 Transmission curve from Quartz Science Inc. commercial UV grade optical melt silica. Thickness 10 mm.

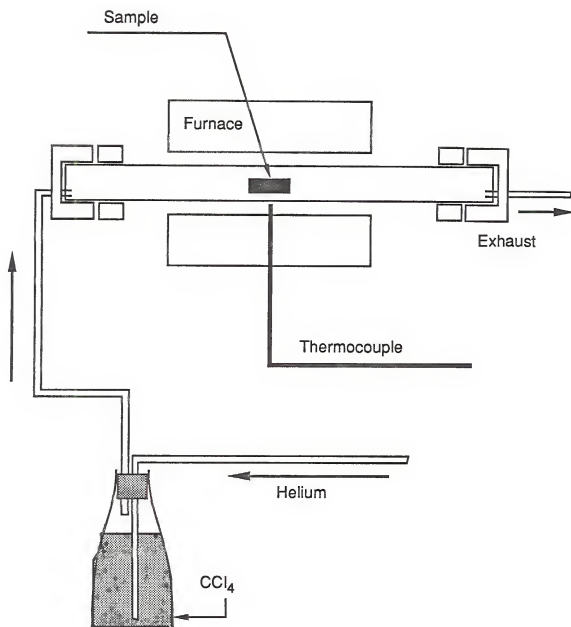


Figure 4-10 A mixed vapor(CCl_4 and He) atmosphere within the tubing of a furnace.

Densification in an air atmosphere was carried out using the heating program shown in Figure 4-11. These samples were heated to designated temperatures (150°C, 450°C, 750°C, 800°C, 850°C), cooled to room temperature, and then subjected to density and optical absorption measurements. The UV-VIS-NIR and FTIR spectra were used to monitor the fundamental, overtone, and combination vibrations of hydroxyl groups within the ranges of 900 nm to 3200 nm and 2083 nm to 50,000 nm, respectively.

The heating program for densification of samples dehydrated in a carbon tetrachloride/helium atmosphere in a tube furnace is shown in Figure 4-12. During the dehydration process carbon tetrachloride was consumed at a rate of 4 cc/hour. The samples were removed at various temperatures during the heating program (850°C, 950°C, 1050°C, 1150°C). Density measurements of the samples were taken, followed by the UV-VIS-NIR and FTIR spectra measurements within the previously stated ranges.

Results and Discussions

The density measurements at various sintering temperatures for samples with or without chlorination are shown in Figure 4-13, in which the density of the water-rich (without chlorination) gel sample reaches a maximum (≈ 2.2 g/cc) at a lower temperature about 860°C, and the density of the water-free (with chlorination) gel sample has its maximum (≈ 2.2 g/cc) at a relatively higher temperature of about 1100°C. This indicates that the hydroxyl groups significantly decrease the sintering temperature by lowering the surface energy of silica.

The important absorption peaks and bands found in this dehydration study are summarized in Table 4-1. These peaks and bands are identical to those discovered by previous researchers stated in Section II of this Chapter.

Curves a, b, c, and d in Figure 4-14 show the UV-VIS-NIR spectra of gels heated in ambient air at various temperatures up to about 850°C. Overtone and combination

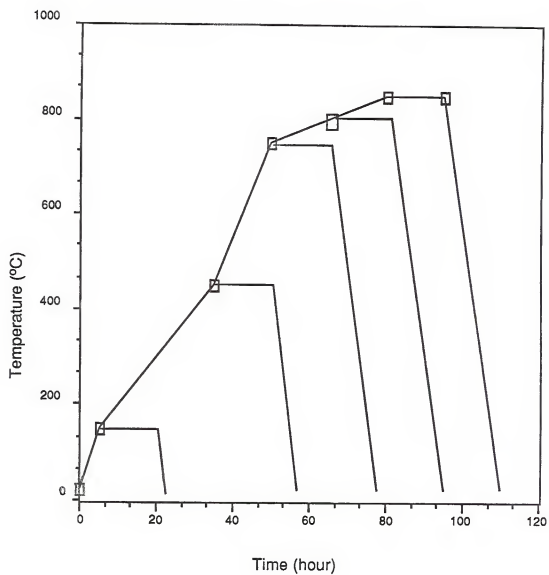


Figure 4-11 Heating cycles for air atmosphere furnace.

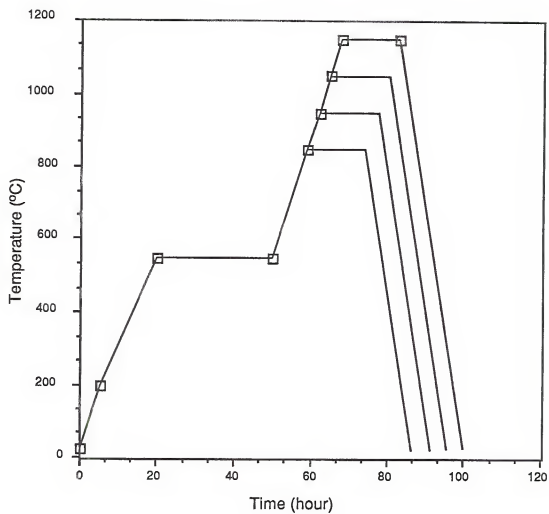


Figure 4-12 Four heating programs for controlled atmosphere furnace.

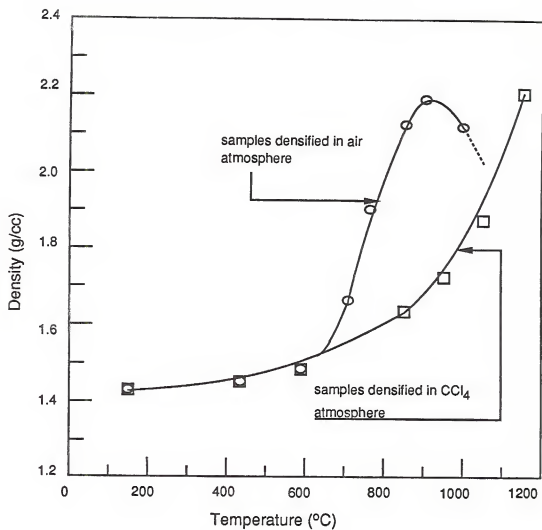


Figure 4-13 Density measurements at various temperatures for samples with or without CCl₄ treatment.

Table 4-1
Absorption peaks of the pore water and the surface hydroxyl groups of gel-silica monoliths

Wavelength (nm)	Identification	observation command
2919.70	***** ν_4	a broad peak on a broad band
2816.88	**** ν_3	a tiny peak on a broad band
2732.24	*** ν_2	a joint of two small peaks at 2768.90 nm and 2698.90 nm
2668.80	** ν_1	a very sharp symmetric peak
2262.48	$\nu_3 + \nu_{OH}$	a broad band, no peak
2207.51	$\nu_2 + \nu_{OH}$	a high broad asymmetric peak
1890.35	$\nu_3 + 2\nu_{OH}$	a high broad asymmetric peak
1459.85	$2\nu_4$	a tiny peak on a broad band
1408.44	$2\nu_3$	a small peak on a broad band
1366.12	$2\nu_2$	a very sharp symmetric peak
1237.85	$\{[2\nu_3 + \nu_{OH}] + [2\nu_2 + \nu_{OH}]\}/2$	a small peak
1131.21	$2\nu_3 + 2\nu_{OH}$	a tiny peak
938.95	$3\nu_3$	a small peak
843.88	$3\nu_3 + \nu_{OH}$	no peak observed
704.22	$4\nu_3$	a tiny peak

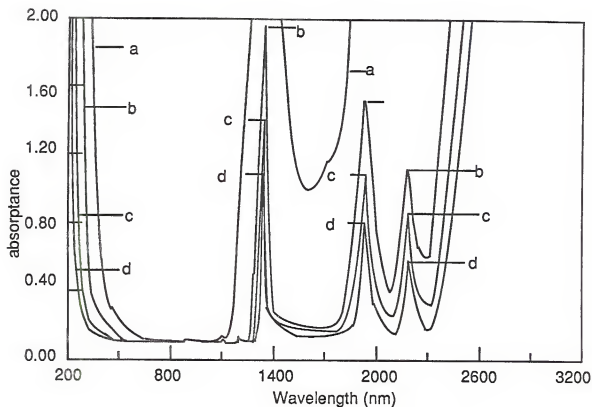
* ν_{OH} : an out of plane bending vibration of Si-O-H bond.

** ν_1 : stretching vibration of an isolated Si-O-H bond.

*** ν_2 : stretching vibration of an adjacent Si-O-H bond.

**** ν_3 : stretching vibration of a Si-O-H bond which is hydrogen-bonded to water.

***** ν_4 : stretching vibration of absorbed water.



curve a is the spectrum of 150°C sample
curve b is the spectrum of 750°C sample
curve c is the spectrum of 800°C sample
curve d is the spectrum of 850°C sample

Figure 4-14 Absorption curves of partially densified gels in air.

vibrational peaks are observed at 704.22 nm, 938.95 nm, 1131.21 nm, 1237.85 nm, 1366.12 nm, 1408.44 nm, 1459.85 nm, 1890.35 nm, 2207.51 nm. A very strong, broad absorption band occurs between 2400 nm and 3200 nm. None of these peaks have been eliminated by heating, instead they have only decreased in intensity with increasing temperatures. Clearly, the gel is not completely dehydrated, even when heated to the point of full densification; further heating results in a foaming problem.

Data obtained in this study show that a combination vibration is identified at 2207.5 nm, resulting from the adjacent silanol stretching vibration at 2732.24 nm (ν_2) and the out-of-plane hydroxyl ion deformation vibration at 11494.25 nm (ν_{OH} (bend)). The peak at 1890.35 nm is a combination vibration of 2816.88 nm (ν_3) plus two times the bending frequency ($2\nu_{OH}$ (bend)). The peak at 1459.85 nm ($2\nu_4$) seems to be the first overtone of the 2919.70 nm (ν_4). The peak at 1408.44 nm ($2\nu_3$) observed is the first overtone at 2816.88 nm (ν_3); whereas the 1366.12 nm ($2\nu_2$) peak is exactly from the first overtone of the fundamental hydroxyl stretching vibration observed at 2732.24 nm (ν_2).

The peak observed at 1237.85 nm is presumed to be an overlap from the contribution of two type of combinations which are 1221.00 nm ($2\nu_2 + \nu_{OH}$ (bend)) and 1254.70 nm ($2\nu_3 + \nu_{OH}$ (bend)). A tiny peak at 1131.21 nm is believed to be $2\nu_3 + 2\nu_{OH}$ (bend) and a small peak at 938.95 nm is presumed to be a second overtone of 2816.88 nm ($3\nu_3$). There is a very tiny peak at 704.22 nm which is a third overtone of 2816.88 nm ($4\nu_3$) as shown in Figure 4-14 curve d.

These results show that for critical optical applications where complete transmission over a broad range of wavelength is important, densification in an air atmosphere is obviously a failure. The resulting quality of this gel can not compete with that of fused silica (see Chapter 1), and it will never reach the point of complete dehydration.

Carbon tetrachloride treated samples were removed from the tube furnace after reaching various temperatures (850°C, 950°C, 1050°C, 1150°C) and then analyzed to determine their characteristic UV-VIS-NIR absorption spectra, as shown in Figures 4-15, 4-16, 4-17(a) and (d). Absorption peaks were visible at 2890.1 nm, 2768.9 nm, 2698.9 nm, 2668.8 nm, 2207.5 nm, 1897.6 nm for the 850°C sample; and at 2884.3 nm, 2765.4 nm, 2698.3 nm, 2669.4 nm, 2207.5 nm, 1897.6 nm for the 950°C sample.

Stretching vibrations of the adsorbed physical water gives rise to typical broad absorption peaks at 2890.1nm and 2884.3nm which are shifted from 2919.70 nm (ν_4) within a broad range from 2700 nm to 3200 nm. Absorption peaks at 2698.3 nm and 2698.9 nm are suggested to be the result of the stretching vibrations of hydrogen-oxygen bonds of adjacent silanol groups. The 2768.9 nm and 2765.4 nm peaks are proposed to be the result of stretching of the hydrogen bonds to the neighboring silanol oxygens, as shown in Figure 4-2. These two kinds of absorption peaks in general can not be distinguished and thus form the combined broad peak at 2732.24 nm which is observed by many researchers [91, 93, 98, 99]. The sharp peaks at 2668.8 nm and 2669.4 nm are identified to be caused by vibrating surface isolated silanol groups (i.e., free hydroxyl groups).

The intensity of all absorption peaks decreases as the temperature increases. The spectrum from the 1050°C sample shows only one peak, as shown in Figure 4-17 (a), occurring at 2668.8 nm (ν_1), which is caused by isolated hydroxyl groups. The sample heated to 1150°C has a spectrum in which the water peaks have been eliminated, as shown in Figures 4-17 (b) and 4-18. The absorption loss due to water is estimated to approach zero as no water or hydroxyl absorption peaks are present at any wavelength. The quality of optical transmittance of this sample is significantly higher than that of traditional fused silica glass.

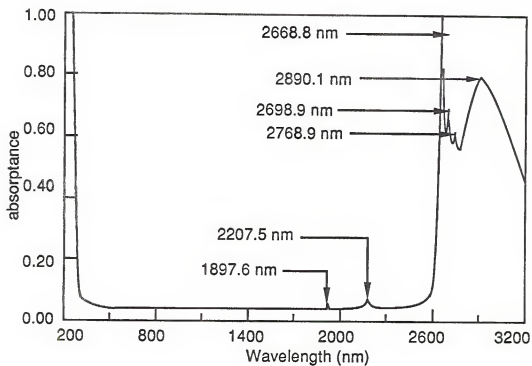


Figure 4-15 Absorption curve of gel partially densified in controlled CCl_4 atmosphere for a 850°C sample of 4 mm thickness.

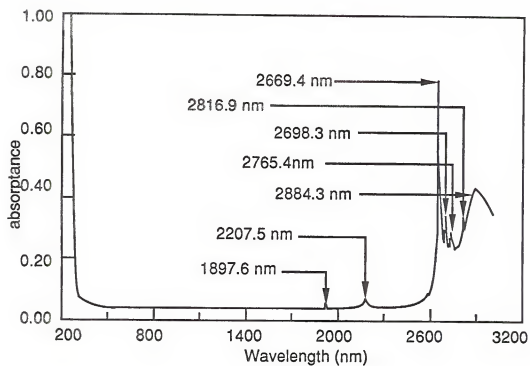


Figure 4-16 Absorption curve of gel partially densified in controlled CCl_4 atmosphere for a 950°C sample of 3.8 mm thickness.

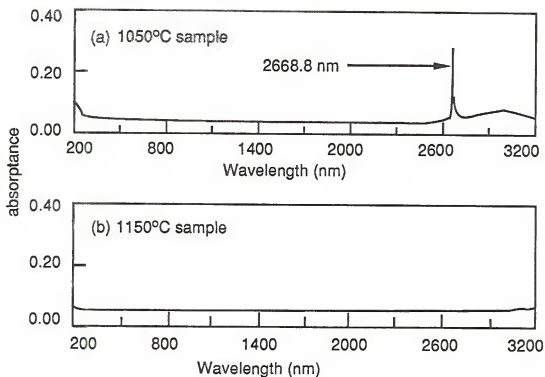


Figure 4-17 Absorption curves of gels partially densified in controlled CCl_4 atmosphere for a 1050°C sample of 3.6 mm thickness and a 1150°C sample of 3.4 mm thickness.

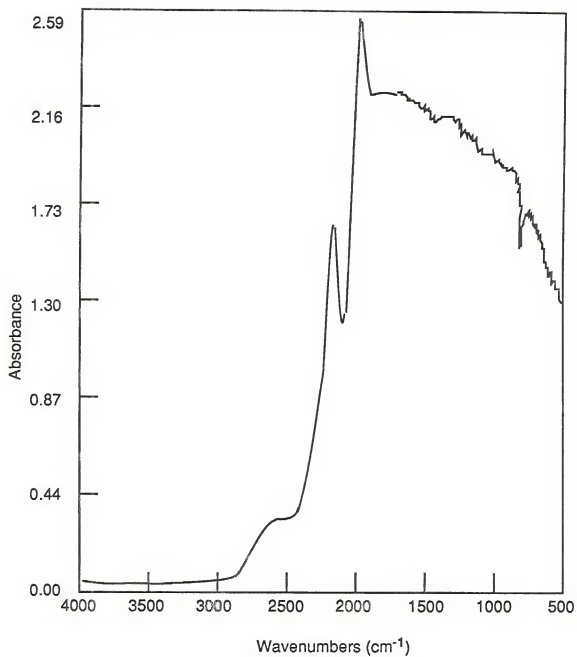


Figure 4-18 FTIR absorption curve of fully densified gel-glass.

Samples which had been heated to 1050°C in the tube furnace were aged for various durations in air: 1 day, 2 days, 4 days, and 7 days. The density, surface area, total pore volume, and pore radius measured were 1.89 g/cm³, 187.23 m²/g, 0.14%, and 11.07 Å respectively. The resulting absorption spectra from each of these samples indicates the readsorption of molecular water with the corresponding reappearance of a broad absorption peak in the 2863.2 nm to 2898.5 nm range and shows no overtone or combination peak, as shown in Figure 4-19(a), (b), (c), and (d).

On the other hand, the samples which were heated to 1150°C in the tube furnace and aged in air for 7 days, 14 days, and 30 days showed no evidence of readsorption, as shown in Figure 4-20(a), (b), and (c). Consequently, the dehydration and densification of gel-silica monoliths as developed in this study results in an optical material equivalent to the best Type IV silica. However, the temperature of densification has been reduced to 1150°C.

Conclusions

The second goal of this study, which was to achieve dehydration of monolithic xerogels, has been accomplished. All the absorption peaks and bands in the range from 200 nm to 4400 nm due to the presence of pore water and surface hydroxyl groups were identified. Monolithic gel-glasses were routinely produced by this sol-gel method in conjunction with the carbon tetrachloride treatment. These completely dehydrated samples were able to reach and maintain a completely hydrophobic surface. Further evidence that these samples were completely densified is supported by mercury-displacement density measurements, with a resulting average value of 2.2 g/cm³ – the density of fused silica glass of Types I, II, III, IV. The optical properties of these fully dehydrated gel-glasses will be evaluated in Chapter 5.

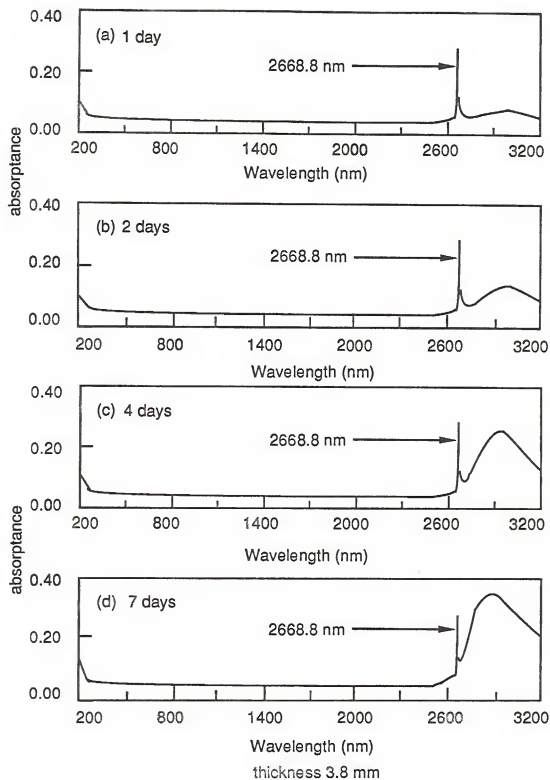


Figure 4-19 Absorption curves of 1050°C samples aged in air for various times.

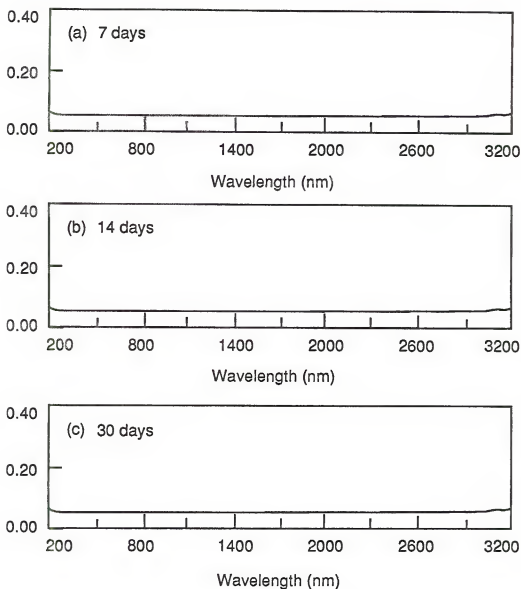


Figure 4-20 Absorption curve of 1150°C sample aged in air for various times.

CHAPTER 5 OPTICAL PROPERTIES OF FULLY DEHYDRATED SILICA GEL GLASS

Introduction

The initial approach towards producing high optical quality, pure silica gel glass monoliths via a chemically treated, thermal densification process was achieved, as described in Chapter 4. The purpose of this chapter is to investigate the optical properties of these samples and to compare them with those of traditional, high-purity, commercial type III and type IV silica glasses.

Silica glass, whether produced by the traditional method or by the low-temperature sol-gel route, can be described as a solidified supercooled silica liquid of randomly packed silica tetrahedra in which a relatively stress free, short-range-ordered structure has been formed, as discussed in Chapter 3 Section IV. This solid appears to have a complete lack of periodicity and a tendency to "order" only in the sense that a few silica tetrahedra are fairly tightly packed together with a statistical preference for a particular interatomic distance, as indicated by x-ray scattering. For optical applications, silica glass usually is required to be an amorphous, isotropic, homogeneous, transparent, dielectric, insulating material.

An ideal silica glass, defined as silica glass without nonbridging oxygen bonds or cation or anion impurities, does not exist in the real world. However, like an ideal gas an ideal silica glass can be approached. The sol-gel fabrication technique developed herein is a step forward to this goal since the new low-temperature route results in no absorption loss due to hydroxyl (OH^-) ions and minimal other ionic impurities in the ppb range.

Interactions between electromagnetic radiation and glass, based on both quantum mechanics and classical treatments, has been well established in the literature [80, 100, 101] and is the basis for interpreting the results presented in this chapter.

Optical properties of gel glass are determined not only by intrinsic chemical aspects (e.g. electronic energy gap, interatomic bond strength, ionic mass, and impurity levels), but also by extrinsic physical aspects of the processing (e.g. thermal history, thermal gradients, structural arrangement, and degree of isotropy) developed during densification process.

The physical properties of a glass are always interrelated; for example, molecular vibrations are responsible for light absorption, resonance, heat dissipation, fluorescence, phosphorescence and thermal expansion [102]. Refractive index is a function of density and electronic polarizability, etc. The optical properties to be examined in this chapter include vacuum ultraviolet (VUV) transmission, ultraviolet (UV) transmission, visible (VIS) and near infrared (NIR) transmission, infrared (IR) spectra, index of refraction (n), and dispersion (v). In addition, the optical quality of the gel silica monoliths is tested by measurements of homogeneity, stress birefringence, striae, bubbles, inclusions, and impurities. This information along with coefficient of thermal expansion (CTE), density and microhardness (Knoop hardness, DPN) data are used to compare and characterize the gel-silica glasses.

Literature Review Regarding Optical Properties of Silica Glass

Classification of the ultraviolet cutoff wavelength of commercially available high purity fused silica has been made by Sigel [72]. He suggests that the location of the VUV (vacuum ultraviolet) absorption edge can be attributed to three factors: (a) a completely stoichiometric Si-O network, with its strong O-Si-O bridging bonds, which provides the minimum absorption wavelength at about 150 nm; (b) a small amount of terminal Si-O bonds (e.g. silanol groups), also called non-bridging oxygen (NBO) bonds,

which determines the degree of shift to higher wavelengths in the 150 nm to 200 nm range; (c) significantly higher wavelength shifts, from 200 nm to 350 nm, which are induced by impurities (e.g. transition elements, alkali, alkaline-earth and halogen elements) in the ppm range, as listed in Tables 1-1, 1-2 and shown in Figure 1-1.

Refinement of the sol-gel precursor, for example TEOS (tetraethylorthosilicate) reduces the metallic impurities to a minimal ppb level, as listed in Table 5-1, which makes it possible to produce a glass having a very high quality of light transmission in the VUV and UV. The elimination of physical and chemical water (also considered impurities) associated with the gel has been described in Chapter 4. An absolutely impurity-free silica glass should exhibit a VUV absorption edge of approximately 150 nm, as indicated in factor (a) above.

Silica glass is capable of being used as an "optical window" between the vacuum ultraviolet and infrared absorption (160 nm to 4400 nm) regions. The subregion from 600 nm to 1100 nm is the portion of the electromagnetic spectrum of interest for present day long distance optical fiber communication systems [103]. However, the "window" from 600 - 1100 nm is not usually perfect since a number of material absorption and scattering losses are present. Loss mechanisms, including fundamental UV and IR absorption tails, overtone and combination peaks of hydroxyl groups, and Rayleigh scattering are shown in Figure 5-1.

Rayleigh scattering is due to density and compositional variations in the material. Today, type IV silica is developed and produced commercially for making optical waveguides (fibers) which require extremely low signal loss for long distance use in optical communication cable systems. The best quality of silica optical fiber (type IV) has been achieved with an internal attenuation value around 0.2 dB/Km ($10 \text{ dB} = 1 \text{ OD}$ optical density absorbance = 10% transmission, $\text{OD} = \text{Log } [I_0/I]$ where I_0 is the incident intensity, I is the transmitted intensity) at 1550 nm in single-mode operation [see p. 32 in ref. 83]. Silica gel-glass optical fiber with no hydroxyl groups and minimal

Table 5-1
Impurity levels in TEOS (ppb).

Al = 20	Li < 10	Cu ≤ 10	Fe = 1000
Ca = 50	Mn < 10	Ti ≤ 20	Mg = 100
Co < 50	Na = 30	Cr ≤ 50	Zn ≤ 50
K = 100	Ni < 100		

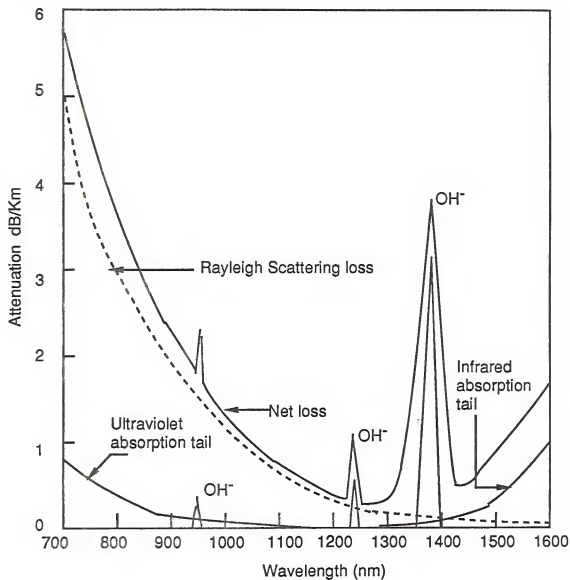


Figure 5-1 Typical spectral loss curves of silica optical fibers.

metallic ion impurities has been made by Susa showing a low-loss 5.9 dB/km at 850 nm [104]. The gel-glass monoliths developed herein should have equivalent or even better quality.

The infrared absorption (IR) spectrum of a glass can be used as a tool to understand the chemical composition, molecular vibrations and the molecular bonding within the material. According to both classical and quantum theories, as two atoms with partially filled outer electron orbital approach each other the energy will either increase or decrease. For example, if two outer electrons, one from each atom, have parallel oriented spins, the result will be repulsion and the energy will increase. The closer they move together, the higher the repulsive force, consequently, the atoms will move apart resulting in an antibonding molecular orbital arrangement. If the spins are antiparallel, the result will be attraction and the energy will decrease. The lowest energy is achieved when the bonding takes place as the two orbitals overlap and electrons are shared by two atoms. If the atoms come too close together, the repulsive force rises due to two positively charged nuclei. The energy curves of this bonding (Morse curve) and antibonding system is shown in Figure 5-2 [see p. 381-408 in ref. 102].

Atoms in a molecule can vibrate harmonically but not symmetrically with the atoms moving together and moving apart as a stretching mode. This vibration of a bonding molecule can be expressed as a horizontal line at a certain temperature within the bonding curve of Figure 5-3. As shown in quantum theory, the vibration levels are not continuous and always have many rotational levels associated with a vibration level and a lowest possible energy level, called zero point energy, must exist even at 0°K. The higher energy level of a stretching vibration results in a larger average displacement between two nuclei. Any vibration energy higher than the destruction of the bonding energy will move atoms apart. The vibration frequencies of all molecules is so low that the energy involved is too small to interact directly with visible light; however, the absorption due to vibrational transitions between the vibrational ground state and

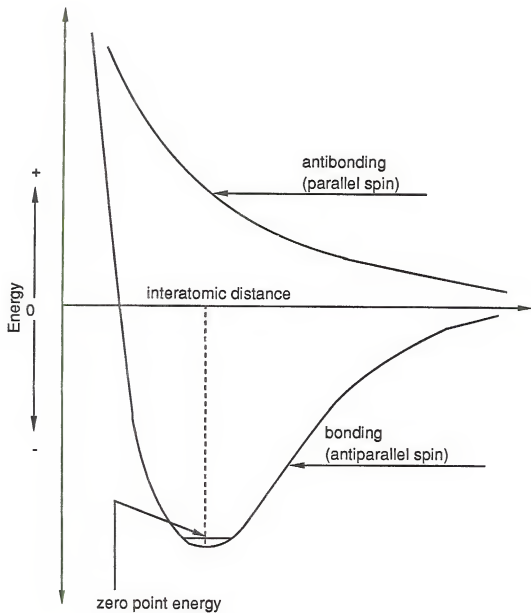


Figure 5-2 The energy curves of the antibonding and bonding molecular orbitals.

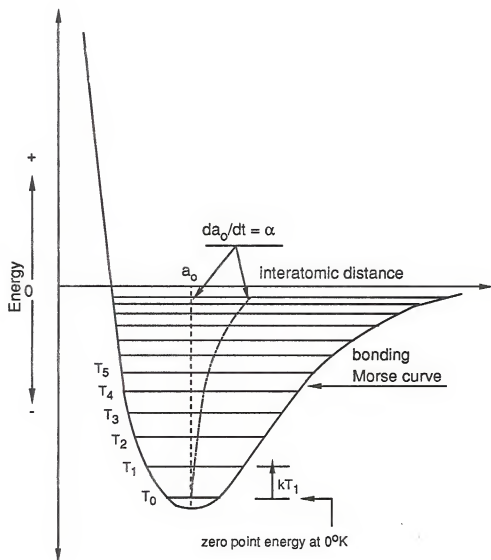


Figure 5-3 The vibration levels at various temperatures.

excited states are found in the energy range of the infrared spectrum, at least for silica and silicate glasses.

A comprehensive simplified diagram of the molecular vibrational energy levels in a ground state Morse curve and two excited state Morse curves is shown in Figure 5-4. This diagram indicates that the IR absorption could possibly result in a series of possible energy transformations in a silica glass which include resonance, heat dissipation by internal conversion, fluorescence, heat dissipation by interstate crossing, and phosphorescence.

Because of the asymmetry in the potential energy curve (Morse curve), the mean position of the center of mass of the vibrating atoms will be displaced as the amplitude of vibration increases, as shown in Figures 5-3 and 5-5(a), resulting in thermal expansion of the material. The thermal expansivity is determined by the asymmetry in the potential energy curve, and the deeper the minimum the more symmetrical is the curve near the bottom, as shown in Figure 5-5(b). A strong bonding material has a deeper valley of higher symmetry which results in a smaller thermal expansion.

D. G. Holloway, in his book *The Physical Properties of Glass* [see p. 36-41 in ref. 63], states that "silica glass shows an anomalous thermal expansion behavior: the thermal expansion coefficient (CTE) for this glass is very much lower than for quartz (80×10^{-7} parallel to axis 134×10^{-7} perpendicular to axis), and it becomes negative below about -80°C . This unusual behavior may be related to the very open structure of the network, since the density of quartz is 2.66 g/cm^3 and silica glass is 2.20 g/cm^3 , and the consequent predominance of vibrational modes involving displacements of the silicon and oxygen ions transverse to the bond direction".

It is reasonable to assume that the large interatomic space in vitreous silica partially accommodates the dimensional increase with temperature due to stretching vibrations and this reduces the thermal expansion effect. From the point of view of a classical spring model, it is relative easier to bend than to stretch a spring.

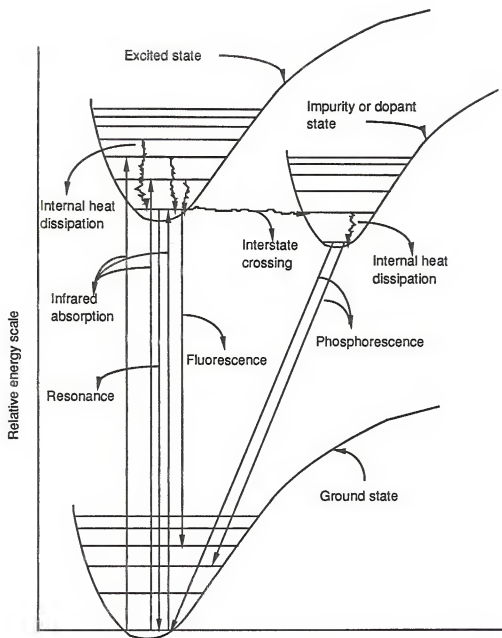
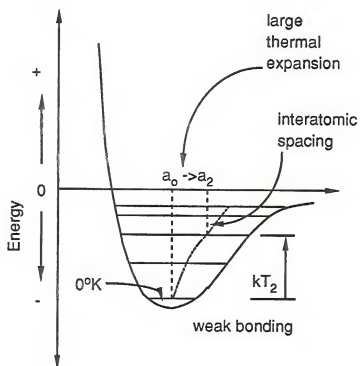


Figure 5-4 Possible energy transformation in a glass.

(a)



(b)

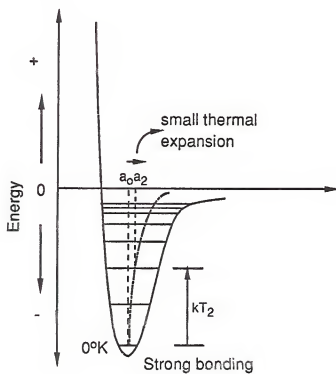


Figure 5-5 Thermal expansion depends on bonding strength

Consequently, the stretching vibration of a Si-O-Si bond is at a higher energy, at around 1130 cm^{-1} than the rocking vibration which is at 480 cm^{-1} .

As the temperature decreases below a certain point (T_C) the stretching vibration can no longer contribute to a dimensional change due to the onset of symmetry of the Morse curve, as shown below point (T_C) in Figure 5-6(b) curve (1).

It is also reasonable to propose that as the temperature continuously decreases below T_C the strong transverse bending vibration of silica starts to reduce its amplitude. This consequently increases the interatomic distance as shown in Figure 5-6(b), curve (2), and thus changes the dimensions as shown in Figure 5-6(a) and curve (3) of Figure 5-6(b).

The corresponding coefficient of thermal expansion curve of vitreous silica is shown in Figure 5-6(c). Thus, both the large interatomic space and the decrease of amplitude of bending vibrations with temperature below T_C contribute to the unusual thermal expansion behavior in silica glass. As will be shown later, this "anomalous" CTE behavior of vitreous silica is dramatically different for a sol-gel derived silica.

The optical properties are not solely determined by the chemical composition of the silica gel glass, but are also influenced by the densification procedure. Since the refractive index of glass is related to both chemical composition and density, it can be altered by changes in two interrelated intrinsic properties, the electronic polarizabilities of negatively charged chemical species (e.g., oxygen ion, chlorine ion) and density. The electronic polarizability, α_e , is an inverse function of the electronegativity [105]. The electronegativity of an oxygen ion (O^{2-}) is higher than that of a chlorine ion (Cl^{-1}). Consequently, the polarizability of a chlorine ion is higher than that of oxygen ion.

The index of refraction (n) is proportional to the summation of the polarizability of all the chemical species in a glass. Because of the higher polarizability of the anions, n is primarily dependent on the summation of the anionic

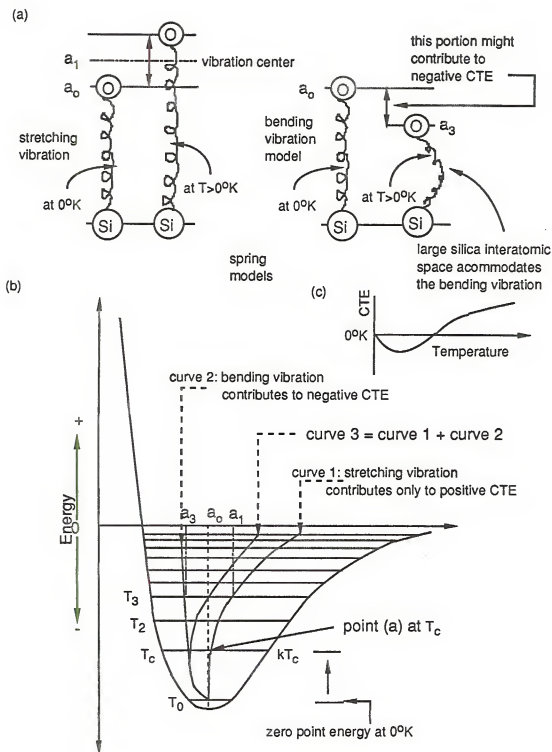


Figure 5-6 A proposed classical spring model and thermal expansion curves of silica glass

polarizabilities. This relationship is described by the Lorentz - Lorenz equation:

$$\alpha = \frac{3}{4} \epsilon_0 (n^2 - 1) M / [N_0 (n^2 + 2) \rho] \quad (1)$$

Therefore n is directly proportional to α as the other items in the equation above are constants; i.e.

N_0 is Avogadro's number

ϵ_0 is the dielectric constant of vacuum

M is the molecular weight of silica

ρ is the density of silica

The second important effect to consider is density. Since α is constant for silica, on condition that other anionic impurities are negligible, the density is proportional to $(n^2 - 1)/(n^2 + 1)$. Thus, as density increases the index of refraction increases.

Susa, Matsuyama, Satoh, and Suganuma at Hitachi Ltd. Japan [106], reported on the effect of chlorine content in sol-gel derived silica glass. They observed that the refractive index of the gel glass increases in proportion to the chlorine content. These findings are correct according to the larger chlorine ion polarizability discussed above. However, in their report the chlorine content of selected gel glass samples was determined by nephelometry, which is a method to measure the concentration of a suspension or substance or a second phase (e.g., bubbles, inclusions) by comparing the brightness of light passed through a sample with that passed through a standard and is incapable of directly measuring a colorless ionic solution (e.g., NaCl in water, or Cl^- in glass). All the samples they produced had been heated to 1300°C, consequently, those with a higher initial chlorine (Cl^-) ion concentration were likely to have proportionally freed more chlorine gas (Cl_2) to create more closed micropores. This structural change would decrease the brightness of incident light in the measurement and lower the apparent density. In addition the equilibrium of $2\text{Cl}^- \rightleftharpoons \text{Cl}_2 + 2e^-$ should be a constant, $K = [\text{Cl}_2]/[\text{Cl}^-]^2$, at that temperature for all samples having various chlorine contents. Therefore, samples with a higher initial surface area were

expected to have a higher structural chlorine (Cl^{-1}) residual attaching to the silica matrix which would contribute to a higher refractive index (freed Cl_2 gas which boiling point is -34.6°C , the index of refraction is 1.000768). It is thus reasonable to conclude that the measured refractive index in the report of Susa, et al. was mainly proportional to the concentration of micropores rather than to that of chlorine (Cl^{-1}) and the obtained apparent density decreased as the chlorine gas, Cl_2 , content increased.

According to the Lorentz - Lorenz relation, the refractive index is linearly proportional to the true density of silica (SiO_2) as shown in Figure 5-7 [107]. Consequently any changes in short-range-ordering, crystallization or structural transformations of vitreous silica that increases the density will also increase the refractive index. The true density can be varied in a sintering process by controlling the thermal history in the glass transition range of temperatures. Unfortunately, such phase changes or structural rearrangements in small scale (below 2 wt.%) is unable to be detected using x-ray diffraction. In addition, a small amount of a second phase (microvoids) found in gel dried at 160°C using a microscope, is x-ray undetectable by x-ray diffraction.

The true density of a dehydrated gel glass with microvoids and closed micropores is difficult to determine. The apparent density, which has a value around 2.184 gm/cm^3 comparing to 2.202 gm/cm^3 $((2.202 - 2.184)/2.202 = 0.8 \text{ wt.}\%)$ of fused silica, shows the effect of a very small volume fraction of micropores. Thus, differences in refractive index can be due to either an increase of chlorine content or an increase in density. When both factors are present it requires a measurement other than nephelometry to separate them.

The index of refraction of a material usually decreases as the wavelength (λ) of light increases. This change with wavelength is called the dispersion of the index of refraction and is defined as $dn/d\lambda$. However, most practical measurements are made by using the index of refraction at fixed wavelengths at the yellow helium d line (587.0740

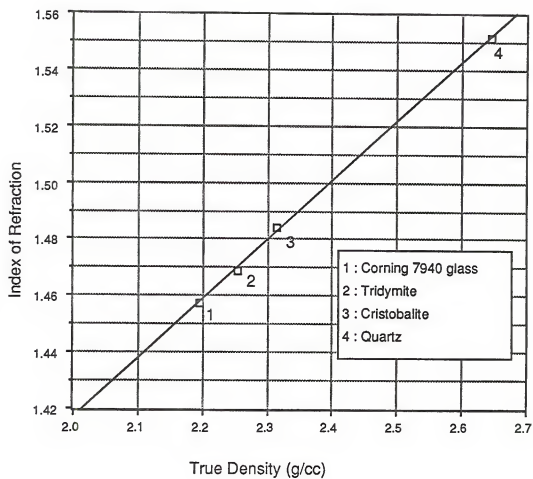


Figure 5-7 Index of Refraction versus True Density

nm), the blue hydrogen f line (486.1337 nm), and the red hydrogen c line (656.2725 nm). The numerical difference between the two indices of refraction at the f and c lines is called the mean dispersion ($n_f - n_c$). The ratio $(n_f - n_c)/(n_d - 1)$ is the dispersive power. Its inverse is called Abbe's value, $(n_d - 1)/(n_f - n_c)$. The dispersion of the gel derived silica glasses developed herein is described in a later section.

Examination of the homogeneity of a piece of glass for optical applications is very important since the wavefront of incident light can be distorted by any variations of index of refraction in a nonhomogeneous glass. Index variations can be caused by localized thermal gradients which induce density gradients. Such inhomogeneities can result from either an improper sintering process or impurity fluctuations within the densified glass. Consequently, careful control of both densification and the dehydration process is necessary to provide a uniform refractive index throughout the gel glass body.

Interferometry is a precision measurement which can be used to examine the quality of a material surface, to metrology, to the alignment of optical and mechanical components, or to examine the differences in optical path length ($S = Ln$ where S is optical length, L is sample thickness, n is index of refraction) in a glass. The path difference, T , is the difference between two such path lengths, $T = S_2 - S_1 = L(n_2 - n_1)$, where thickness L is constant. From Young's double-slit experiment, T can be expressed as $T = m\lambda$ where m is the order of interference or the number of fringes.

By rearranging the two equations above we have $m = L(n_2 - n_1)/\lambda$ [see p. 187-204 in ref. 100]. Consequently, for a piece of glass with two perfectly parallel surfaces and constant thickness, any internal irregular variation of refractive index results in an irregular fringe shift pattern on an interferogram. An interferogram always shows alternative dark bands and white bands with one fringe corresponding to one pair of white and dark bands. This is the method used to examine optical homogeneity in the densified gel-glass samples.

Internal stress in glass can be produced by many factors such as mechanical stress, thermal quenching, phase separation, crystallization, etc.. For example, If a piece of glass quenched from high temperature has residual stresses (tension and compression) and if light is propagated through such a glass the difference in refractive index between the regions of stress results in stress birefringence. The birefringence is defined as the numerical difference between the two refractive indices ($\epsilon - \omega$) or a measure of path difference, T , per sample thickness, L . Consequently, the birefringence can be expressed as the retardation of light which is $\epsilon - \omega = T/L$ where T is $\delta\lambda/2\pi$, δ is the phase difference, and λ is wavelength of incident light [see p. 339-341 in ref. 100].

To examine the stress induced birefringence the addition of two polarizing filters and a rotatable stage converts a laboratory microscope into an polarizing microscope. If a piece of strain-free glass is placed on the stage between these two crossed polarizers, the glass remains dark no matter how the stage is turned; such a glass is isotropic. Anisotropic glass, in contrast, has four positions of maximum extinction, 90° apart, when the stage is rotated. The phase difference, δ , can be determined by measuring the angle of rotation to give compensation.

To be optically useful a silica glass must be able to transmit electromagnetic waves efficiently within the region in which it is to be used, i.e., it must exhibit a very low scattering. For uniform interaction between light and glass, the glass should not only have a homogeneous index of refraction but also be free of excessive striae, bubbles and inclusions. In traditional melt glasses, these three types of defects are often found if the thermal processes are inadequate. Striae result from incomplete homogenization and high temperature mixing in the liquid phase prior to casting. Bubbles from chemical reaction of raw materials and inclusions from unmelted high-temperature impurities on the scale of micrometers to millimeters, and even larger, are formed and trapped during an improper melting and cooling process. Consequently, it is necessary to examine whether such imperfections are present in a gel glass.

Finally, impurities such as alkali and alkali earth elements, transition-metal elements, and halogen elements terminate the bridging oxygen bonds, create light interaction centers and degrade the optical performance of a silica glass. All of the above physical and structure factors must be determined to characterize the quality of the gel-silica glass produced herein.

Experimental Procedure

Glass Fab, Inc. of Rochester, New York was selected to evaluate these first generation ultrapure silica gel glass, produced as described in Chapter 4, as potential optical components. They were contracted to perform optical performance characteristics and properties tests on six gel-silica glass samples. Several commercially available, high quality type III optical silica glasses were used for comparison. The samples were three high purity fused silica samples (Corning 7940) and three synthetic optical quartz samples (NSG quartz - type ES). Comparative optical transmission and stress birefringence data were also obtained at the Advanced Materials Research Center (AMRC) of University of Florida. The tests performed on these samples are listed in Table 5-2.

Prior to Glass Fab's transmission testing they polished all samples simultaneously to 0.5 wavelength of red helium light (706.5188 nm). After polishing, the samples were tested for flatness on two surfaces to 0.5 wavelength flatness. Samples were then cut into 20 mm squares and two surfaces were polished to a 90 degree angle.

Vacuum ultraviolet (VUV) transmission tests, in the 160 nm to 200 nm range, were performed by Glass Fab on an Acton Research Corporation, 0.2 meter (focal length), Model VM-502 with an uncertainty of $\pm 2\%$.

Transmission in the UV-VIS-NIR range, 200 nm to 2600 nm, was measured by Glass Fab using a double-beam Perkin-Elmer spectrophotometer, slit width 2-10 nm, with an uncertainty of $\pm 1\%$. Transmission measurements were made in the 186 nm to

Table 5-2
Physical property measurements on fully densified gel-silica glasses
and fused silica glasses

Test	Number of Samples measured	Source
Optical tests:		
Transmittance	6 gel glass samples 6 control samples	Glass Fab
(1) Vacuum UV (2) UV-VIS-NIR (3) IR		
Refractive index	6 gel glass samples 6 control samples	
Dispersion	6 gel glass samples 6 control samples	
Homogeneity	6 gel glass samples 6 control samples	Glass Fab
Striae	6 gel glass samples 6 control samples	Glass Fab
Stress birefringence	6 gel glass samples 6 control samples	Glass Fab
Bubbles and Inclusions	6 gel glass samples 6 control samples	Glass Fab
Impurity	1 gel glass sample	Glass Fab North Carolina State University
Thermal and mechanical test:		
Coefficient of thermal expansion	(a) 1 gel glass sample (b) 2 gel glass samples	Penn State University University of Arizona
Specific gravity	3 gel glass samples 2 control samples	Corning Engineering Lab Services
Knoop hardness	1 gel glass sample 1 control sample	Corning Engineering Lab Services

3200 nm range at the AMRC on approximately 50 unpolished gel-silica glass samples using a double-beam Perkin-Elmer Lambda 9 UV/VIS/NIR spectrophotometer, Model 33, slit width 1 nm, with an uncertainty of $\pm 1\%$.

Infrared transmittance was also measured in the 2500 nm to 5000 nm range by Glass Fab using the spectrophotometer previously mentioned.

Refractive indices were measured by Glass Fab on a Pulfrich Abbe Refractometer using four special light sources, isolating the six spectral lines at which the tests were conducted, as listed in Table 3. Calibration was accomplished by use of a standard index sample certified by the National Bureau of Standards (NBS) accurate to $\pm 1 \times 10^{-5}$. Dispersion ($dn/d\lambda$) values were calculated from refractive indices at different testing wavelengths in accordance with the Abbe's value $v_d = (n_d - 1) / (n_f - n_c)$ defined in Section II of this chapter.

Homogeneity of the gel glass and control samples was checked for wavefront distortion by Glass Fab on a Zygo Zapp Interferometer. Samples were examined and then additionally tested using oiled-on master plates to eliminate any effects of polishing.

Striae tests were made by Glass Fab using a pin hole arc lamp to project an image 10 times size onto a projection screen. In this test any striae in a glass appear as fine lines on the screen.

Stress birefringence tests were performed by Glass Fab using a Fridel Polariscopes, Polarmetrics Model 35 polarimeter. Prior to cutting, polished samples were examined in two directions. Any visible strain appeared as a field change (a twist of the polarized length). Using a rotating eyepiece, the field was rotated until the field change was reversed. This angle change was used to determine the retardation level, R , (strain) using the formula: $R = 3.3 A/T$, where A is angle of rotation to give compensation, and T is thickness of sample.

Table 5-3
Optical dispersion wavelengths

Designation	Wavelength (nm)	Spectral Line
r	706.5188	red helium line
c	656.2725	red hydrogen line
d	587.5618	yellow helium line
e	546.0740	green mercury line
f	486.1327	blue hydrogen line
h	404.6561	violet mercury line

Stress birefringence was qualitatively determined at the AMRC on "as cast", partially dense (~60%) and fully dense gel-silica glass samples using two plane polarized laminated plastic sheets.

Bubbles and inclusions were examined by Glass Fab using a Nomarski phase-contrast microscope. In this test the magnification is set at 400X and the resolution is 1 micrometer. The number of bubbles and inclusions were counted in a volume 0.02 mm^3 . Volumes were randomly selected in each quadrant and at the center of the samples. The sampling volume was defined by a 0.5 mm diameter field of view and a 0.1 mm sweep inside the sample about 0.5 mm from a polished face, as shown in Figure 5-8.

Impurity levels were measured in a gel glass sample by the Department of Nuclear Engineering, North Carolina State University using a neutron activation analysis technique [108] to measure the number and energy of gamma and x-rays emitted by the radioactive isotopes produced in the sample matrix. This method involves irradiation of the test sample with thermal neutrons from a nuclear reactor at a selected time period. Quantitative analysis was obtained by comparing the number of characteristic x- or gamma rays detected from the gel glass with the number determined for appropriate standards.

Other physical properties measured included coefficient of thermal expansion, specific gravity and knoop hardness.

Coefficient of thermal expansion (CTE) values from room temperature to 773 K were measured on one gel glass sample by the Materials Research Laboratory, Pennsylvania State University using a laser speckle dilatometer and on one gel glass sample by Orton Jr. Ceramic Foundation, Ohio, using an automatic recording dilatometer. The new laser speckle method [109] was based on the movement of a laser beam reflected from a probe bar caused by thermal expansions of the sample and reference rods as shown in Figure 5-9. The reflected laser beam was observed with a small photodetector. A minute change in the laser beam position thus results in a precision

gel glass sample

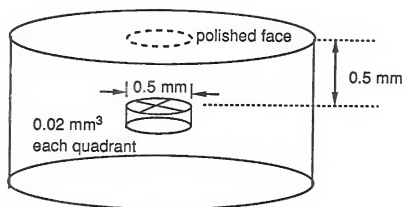


Figure 5-8 Volume for counting "bubbles or stars"

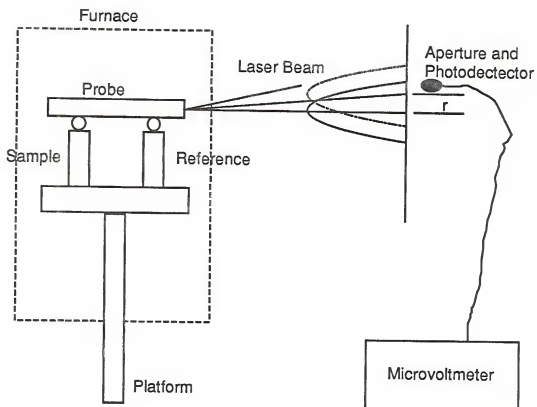


Figure 5-9 Schematic diagram of a laser speckle dilatometer

thermal expansion measurement. The Orton dilatometer was laboratory calibrated for accuracy against platinum to help insure precise measurement of thermal length changes of the gel glass sample.

CTE values from 4 K to 473 K were obtained on two gel glass samples with five control samples by the Optical Science Center, University of Arizona using a low temperature laser interferometer dilatometer.

Precision apparent density measurements were obtained on three gel glass samples with two control samples (Corning 7940 and NSG ES fused silicas) by Corning Engineering Lab Services using a simple deionized water displacement buoyancy method.

Knoop Microhardness values of one gel glass sample and one control sample were determined by Corning Engineering Lab Services using a 100 gram loaded knoop hardness tester in accordance with ASTM C-730 testing procedure [110].

Results and Discussions

Transmission data of the six silica gel glass samples are separated into three sections, according to their wavelength testing ranges, and compared with the traditional glass control samples. The results shown in Figures 5 - 10, 11, 12 and Table 5-4. The gel glass samples demonstrate a uniformly high transmittance in the 200 nm to 2600 nm range. In the vacuum ultraviolet region at 165 nm the gel glass has five times the transmittance of the Corning 7940 sample and 2.5 times that of the NSG-ES samples. The flat transmission spectra of the gel glass is evidence that cation impurity contaminations have been minimized and water has been eliminated. In contrast, transmission spectra for both control samples show significant water absorption peaks at the wavelengths of 1370 nm and 2200 nm.

The gel-silica glass also shows substantially greater transmission than the traditional type III silica glasses when tested in the far IR range from 2500 nm to 5000 nm, as shown in Figure 5-12. Corning 7940 and NSG-ES fused silica samples show 0%

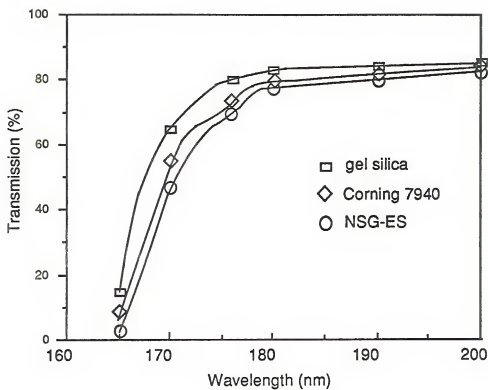


Figure 5-10 Vacuum ultraviolet transmission of optical silicas
sample thickness: 3 mm.

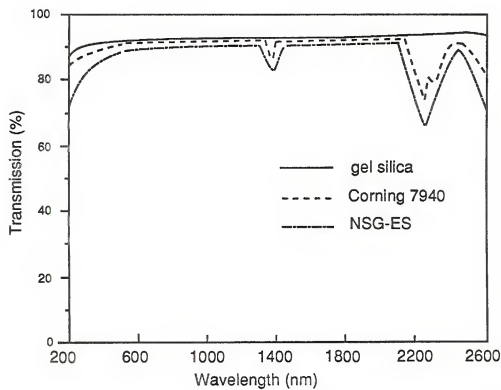


Figure 5-11 UV-VIS-NIR transmission of optical silicas
sample thickness: 3 mm.

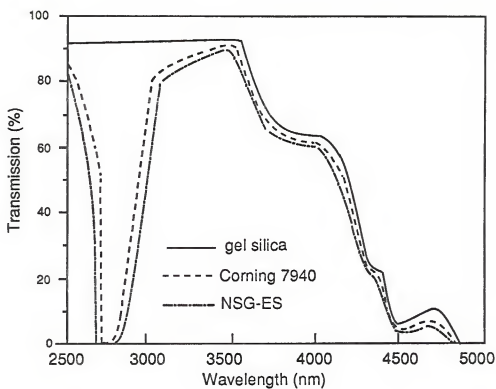


Figure 5-12 Infrared transmission of optical silicas
sample thickness: 3 mm.

Table 5-4
Vacuum ultraviolet transmission data

Sample	Transmission (%) at Wavelength of					
ID No.	165 nm	170 nm	176 nm	180 nm	190 nm	200 nm

Gel glass test samples 3 mm thick:

Q 27	13.9	65.0	80.0	83.0	84.5	85.5
N 34	14.0	63.0	78.0	80.5	82.5	83.5
P 37	15.0	64.0	78.5	80.5	83.0	84.0

Corning # 7940 Control Sample, 2 mm thick:

CGW-2(a)	08.0	60.0	76.0	83.0	88.0	91.0
----------	------	------	------	------	------	------

Corning # 7940 Control Sample, Converted to 3 mm thickness:

CGW-2 (a)	03.0	47.0	67.0	77.0	82.5	87.0
-----------	------	------	------	------	------	------

From reference, reflection loss per single surface:

R Loss (b)	05.7	05.5	05.3	05.1	04.9	04.7
------------	------	------	------	------	------	------

Notes:

a) As noted, the Corning #7940 sample measured was 2 mm thick compared to the 3 mm thick gel-glass test samples. This data was converted to 3 mm thickness for comparison.

b) Reflection losses shown are based on published data for fused silica available from Glass Fab, Inc. and is presented for reference only.

transmission at the hydroxyl group absorption peak of 2730 nm, compared to 93% transmission of gel-silica glass.

Precise refractive index measurements of the silica gel glass and control silica samples are listed in Table 5-5 as a function of measuring wavelength. The mean value and its standard deviation of the index at each wavelength is also shown in Table 5-5. A summary of the dispersion data is given in Figure 5-13. The size of data points in Figure 5-13 represents the variation of the data in Table 5-5.

The reference index n_d and the calculated Abbe constant for each type of silica is listed in Table 5-6. The variation in refractive index (d-line), from sample to sample of gel glass, indicates that this characteristic is related to variations in thermal processing.

A homogeneity test on one gel glass sample, Figure 5-14, shows an approximately 0.863 wave peak to valley (P/V) ratio wavefront distortion in the inner 25 mm area, which compares to the Corning samples with a 0.529 P/V wavefront distortion (equal to the power of the polished surface). However, further examination of the gel glass shows a roll off with 4 to 5 waves P/V significant distortion at the outer 5 mm. No strain was evidenced on the gel glass edge; therefore, it is clear that the Inhomogeneity in the material and its edges is strictly due to changes in refractive index within the material. This variation is quite pronounced and consistent at the ends, but appears to be better in the middle. The localized variation in refractive index is a result of density gradients caused by thermal gradients and/or chlorine impurity gradients.

No striae were visible during the striae test, indicating that there are no surface irregularities, capillaries, or localized structural defects within the glass. This was true for the six gel glass samples as well as the six control samples.

Table 5-5
Refractive index measurements of the gel-silica glass and fused silica glasses

Test No. ID No.	r	c	Index of refraction (n):			
			d	e	f	h
Corning # 7940 Control Samples:						
1) CGW-1	1.45518	1.45639	1.45848	1.46010	1.46316	1.46965
2) CGW-2	1.45516	1.45638	1.45848	1.46010	1.46317	1.46968
3) CGW-3	1.45517	1.45639	1.45848	1.46010	1.46316	1.46965

Statistical Value:	1.45517	1.45638	1.45848	1.46010	1.46316	1.46966
(\pm)	0.00001	0.00001	0.00000	0.00000	0.00001	0.00002

NSG "ES" Control Samples:

4) NSG-1	1.45516	1.45638	1.45847	1.46009	1.46315	1.46965
5) NSG-2	1.45517	1.45638	1.45848	1.46009	1.46315	1.46965
6) NSG-3	1.45514	1.45636	1.45846	1.46008	1.46315	1.46967

Statistical Value:	1.45516	1.45637	1.45847	1.46009	1.46315	1.46966
(\pm)	0.00001	0.00001	0.00001	0.00001	0.00000	0.00001

Gel-Glass Samples:

7) N34	1.45978	1.46102	1.46317	1.46483	1.46797	1.47464
8) Q34	1.45936	1.46061	1.46276	1.46443	1.46057	1.47426
9) Q27	1.45983	1.46109	1.46326	1.46448	1.46764	1.47435
11) Q11	1.45994	1.46119	1.46334	1.46501	1.46817	1.47487
12) Q30	1.45979	1.45104	1.46319	1.46485	1.46800	1.47468

Statistical Value:	1.45968	1.46093	1.46309	1.46476	1.46791	1.47461
(\pm)	0.00024	0.00024	0.00024	0.00024	0.00024	0.00024

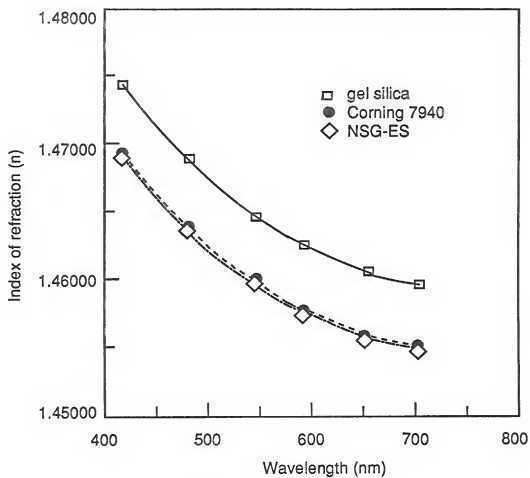


Figure 5-13 Dispersion data comparison of optical silicas.

Table 5-6
Reference indices and Abbe values of silica glasses

Test No.	ID. No.	Reference index (n_d)	Abbe Value (v_d)
Corning #7940, Control Samples:			
1)	CGW-1	1.45848	67.72
2)	CGW-2	1.45848	67.52
3)	CGW-3	1.45848	67.72
Statistical Value:			
		1.45848	67.65
	(\pm)	0.00000	0.11
NSG-ES, Control Samples:			
4)	NSG-1	1.45847	67.72
5)	NSG-2	1.45848	67.72
6)	NSG-3	4.45846	67.52
Statistical Value:			
		1.45848	67.65
	(\pm)	0.00001	0.11
Gel Glass Test Samples:			
7)	N34	1.46317	66.64
8)	Q34	1.46276	66.49
9)	Q27	1.46326	65.90
10)	P37	1.46281	66.21
11)	Q11	1.46334	66.38
12)	Q30	1.46319	66.55
Statistical Value:			
		1.46309	66.36
	(\pm)	0.00024	0.27

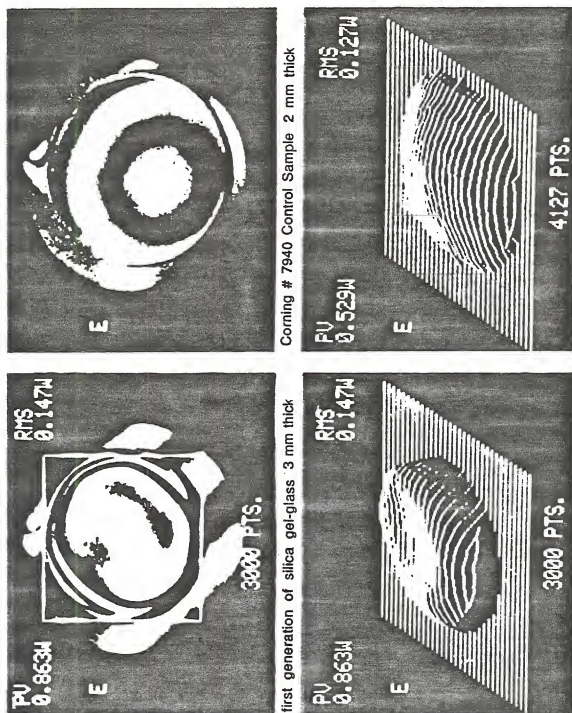


Figure 5-14 Homogeneity tests of silica gel glass sample and Corning #7940 control sample by Zygo Zapp Interferometer.

The stress birefringence test showed that through the faces of the six, 30 mm x 3 mm (diameter x thickness), fully densified gel-silica glass samples no stress or strain could be measured. Through the ends (30 mm length) strain was observed which computed to 4 millimicrons (nanometers) per centimeter. For comparison, normal optical glass, per MIL-G-174 [111], should have less than 10 millimicrons per centimeter. The birefringence constant (R) of 4 nm/cm determined for the gel-silica glass is nearly equivalent to the values of 3.54 nm/cm and 5 nm/cm of Corning 7940 and NSG-ES samples, respectively.

The strain associated with partially densified gel-silica glass samples, using two plane polarized films, is shown in Figure 5-15. The strain present in partially densified gel-silica is eliminated by the densification process (Figure 5-16). This effect can perhaps be characterized as "precision annealing".

The six control samples tested showed no evidence of bubbles or inclusions. All of the silica gel glasses exhibited bubbles approximately one micrometer in size. The so-called "bubbles" are really optical diffraction points. They appear more like "stars" than "bubbles". They are closed micropores created by the freed chlorine gas inside densified gel glass, as discussed in Section II of this chapter. Since the tested samples vary in quantity of these diffraction points, they seem directly related to thermal process parameters and should, therefore, be able to be eliminated by optimization of the thermal-chemical processing. Due to these defects the first generation gel silica samples would not be acceptable for certain precision optical applications. Further analysis of the test results shows the spacing between points to be fairly homogeneous at a distance of about 75-125 microns.

Impurity tests by neutron activation analysis show a significant chlorine content at about 0.1 wt.% with the other impurities in the ten to hundred ppb. No hydroxyl groups were detected. Except for the chlorine content, all impurity levels were below the levels of commercially available Types III and IV fused silica.

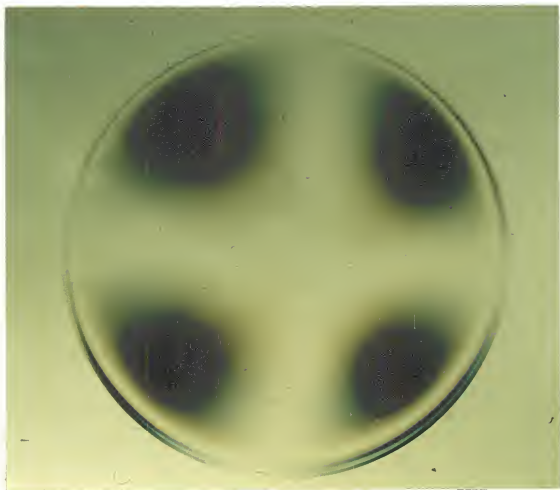


Figure 5-15 Observed strain in a partially dense gel-silica glass

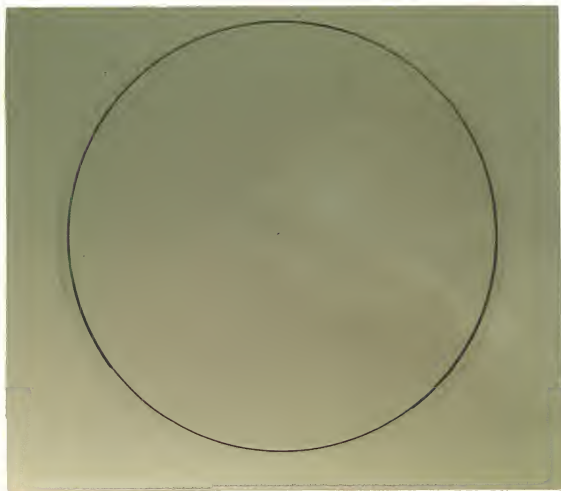


Figure 5-16 Strain elimination in a fully dense gel-silica glass

The physical characteristics of silica glass, which generally include optical, thermal, and mechanical properties, are interrelated. For example, in the gel glass samples, having a large number of diffraction points or "microvoids", lower densities were measured, and lower Knoop hardness values were obtained. Also, the degree of inhomogeneity observed directly relates to the degree of refractive index variation measured. These data are supported by the Lorentz - Lorenz relationship, which indicates that refractive index variation is the result of density gradients and/or chlorine gradients within the gel glass.

Coefficient of thermal expansion (CTE) measurements from three testing laboratories are listed in Table 5-7. Figure 5-17 presents that data collected by the Optical Sciences Center of the University of Arizona, courtesy of Dr. Steve Jacobs. Statistically, gel silica has a CTE value about two times lower and a more stable CTE over a wide range of temperatures than all five of the commercial glasses tested. As discussed earlier the possible reason for the gel silica glass CTE behavior is the lower concentration of cation impurities and a larger intermolecular space between the silica structural units.

Density measurements made on three gel silica samples and two control samples (Corning 7940, NSG-ES) are shown in Table 5-8. The densities of the gel glass measured, on an average, 0.016 g/cm^3 lower than the control samples. Micropores are responsible for these somewhat lower density measurements.

Knoop hardness values were measured on one gel silica sample and one control sample (Corning 7940) with the results shown in Table 5-9. The gel silica measured lower than the control sample; however, the control sample measured significantly lower than its published data. Corning Engineering Laboratory Services reformed their tests and support those results. Though inconclusive, these data are an indication that the first generation gel silica has a lower hardness than fused silica which is

Table 5-7
Coefficient of thermal expansion of fully dense gel silica (α)/°C

Temp °C	Temp °K	Orton	Penn State	Univ. of Arizona
	150			2×10^{-7}
	225			2×10^{-7}
25	298	0.4×10^{-7}	-1.0×10^{-7}	2×10^{-7}
100	373	1.1×10^{-7}	-1.0×10^{-7}	2×10^{-7}
200	473	1.4×10^{-7}	3.1×10^{-7}	2×10^{-7}
300	573	1.9×10^{-7}	3.1×10^{-7}	
400	673	1.0×10^{-7}	3.1×10^{-7}	
500	773	2.4×10^{-7}	3.1×10^{-7}	

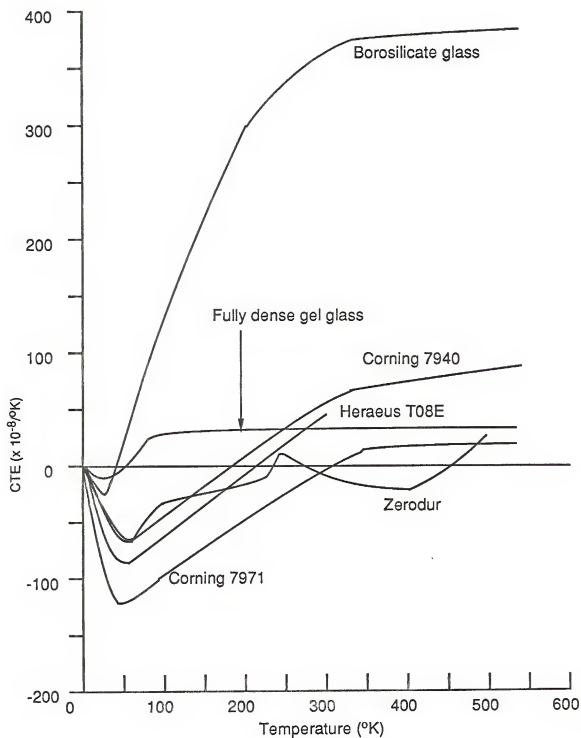


Figure 5-17 Coefficient of thermal expansion of gel silica compare with other fused glasses.

Table 5-8
Density measurements of gel-silica and fused silica

Test Sample Sample No.	ID No.	Density (Specific Gravity, gm/cm ³)
---------------------------	--------	--

Gel Glass Samples, Silica Material:

No.	8	Q 34	2.1829
No.	9	Q 27	2.1835
No.	10	P 37	2.1844

Control sample, Corning #7940, Fused Silica:

No.	1	CGW-1	2.2020
-----	---	-------	--------

Control Sample, NSG ES Fused Silica:

No.	4	NSG-ES	2.2002
-----	---	--------	--------

For Reference Only:

Following are the density (specific gravity) characteristics of various materials based upon published data, grams per cubic centimeter:

- | | | |
|-------------------------------------|-------|---------------------|
| 1. Fused Silica, Corning #7940: | 2.202 | (Same as measured) |
| 2. Fused Silica (Synthetic) NSG-ES: | 2.201 | (> measured value) |
| 3. Fused Quartz (Natural) NSG: | 2.203 | |

Table 5-9
Knoop hardness

TEST SAMPLE NO.	SAMPLE ID No.	100 gm Load, Kg / mmH ²
--------------------	------------------	------------------------------------

Gel Glass Sample:

No. Q 11	456	Standard Deviation: 16.6
----------	-----	--------------------------

Corning #7940:

No. CGW-3	508	Standard Deviation: 11.2
-----------	-----	--------------------------

For reference only:

Following are the Knoop Hardness characteristics of various materials based upon published data (100 gm Load):

1. Fused Silica (Synthetic) 600 - 630
2. Fused Quartz (Natural) 590 - 620

Notes:

It should be noted that the Knoop hardness of the control sample of Corning fused silica measured lower than published data. Other Corning published data on the same material is lower than was measured.

consistent with the density data. It is believed that these low microhardness measurements are also related to the presence of micropores.

A summary of the property data for the commercial dense gel-silica made by a modification of the process developed in this study is presented in Table 5-10. The gel-glass is designated as a type V silica for comparing with the other four types of traditional vitreous silicas.

Conclusions

Data from the characterization tests on the first generation of silica gel-glass monoliths were compared to commercially available control samples of high quality fused silica (type III). It was shown that the VUV-UV-VIS-NIR-IR transmission of gel silica glass is superior to that of fused silica, as observed from its broader transmission range approaching the theoretical value of ideal silica glass, 150 nm to 4400 nm. Gel-silica's broad transmission spectra having no absorption peaks is conclusive evidence that the major impurities, except chlorine, have been successfully reduced to ppb levels. The variation in index of refraction from sample to sample indicates that the chemical dehydration process and/or thermal process greatly influence the homogeneity of the gel-silica optical material, and can thereby be controlled. Recent improvements in thermal processing have eliminated most of this source of variation, as indicated in Table 5-10. No stress birefringence or strain was observed, indicating that the samples were well annealed; also no striae were found.

A significant number of microvoids were observed in the first generation gel silica glass samples. These inhomogeneities resulted in a somewhat lower apparent density and lower Knoop hardness value. Also density variations and/or chlorine gradients within the gel silica glass induced a refractive index gradient, which seriously distorted the incoming wavefront in the optical homogeneity tests.

Table 5-10
Preparation and characteristics of five types of silica glass

Type of Silica	I	II	III	IV	V
	Electromelted Quartz	Flame-Fused Quartz	Hydrolyzed SiCl ₄	Oxidized SiCl ₄	Dense Gel-Silica
Tradenames	Vitreosil-IR ^a Infrasil ^b	Homosil ^b NSG-OX ^e Optosil ^b	7940 ^c 1000 ^d Suprasil ^b NSG-ES ^e	Spectrosil WF ^a 7943 ^c Suprasil-W ^b	Gelsil ^f
Total Cation: (ppm)	30-200	10-30	1-2	1-2	1-2
OH ⁻¹ group: (ppm)	< 5	150-1500	600-1000	0.4-5	< 1
Cl ⁻¹ : (ppm)	0	0	100	< 200	< 1000
UV 50% transmission: (nm)	212-223	210-220	165-188	165-180	165-168
Thermal Expansion Coefficient: (x10 ⁻⁷)	5.4	5.5	5.5-5.7	5.5	2.0
Bubbles and Inclusions: (#/in ³)	0-8	0-5	0-3	0-2	0
Strain: (nm/cm)	5-10	5-10	5-10	10-40	5
Refractive index: (n _d)	1.458	1.458	1.458	1.458	1.458-1.463
Dispersion: (v _d)	67.8	67.8	67.8	67.8	66.4 -67.8
Density: (g/cm ³)	2.21	2.21	2.20	2.20	2.20

a = Thermal American Fused Quartz; Montville, NJ.

b = Heraeus Amersil; Sayreville, NJ.

c = Corning Glass Work; Corning, NY.

d = Dynasil; Berlin, NJ

e = NSG quartz; Japan.

f = Material Engineering & Science, University of Florida & GelTech, Inc.; Alachua, FL.

The gel glass coefficient of thermal expansion is linear over a wide temperature range and lower than that of any previous fused silica. Less impurities and/or a larger intermolecular volume may account for both the low and anomalous thermal expansion behavior.

Elimination of the density variations, microvoids and micropores can be accomplished with a final optimization of the sol-gel process. More precise control of the thermal program and the dehydration technique in densification process will make it possible for gel silica glass to approach the theoretical optical performance of an ideal silica glass.

CHAPTER 6 SILICA GEL OPTICAL FILTERS USING TRANSITION-METAL COMPOUNDS

Introduction

Large, monolithic pure silica gels have been made rapidly and reliably from tetramethylorthosilicate (TMOS) using drying control chemical additives (DCCA). In this chapter attention is shifted to using the TMOS-DCCA method to make silica gels with optical filter characteristics by introducing transition-metal ions into the transparent and colorless matrix. When the impurity is added, five incomplete but equal energy levels are split by the ligand field of the matrix. Ions with incomplete, split d electronic excitational and associated vibrational levels are responsible for absorbing light in characteristic ranges of wavelength in the gel matrix. Color observed in the gel glass containing transition-metal ions is the complementary color to the region of optical absorption due to these excitational and vibrational electron transitions. For instance Cr^{3+} in a distorted octahedral ligand field of crystalline alumina (ruby) absorbs the violet and green-yellow from the spectra, thus giving ruby its beautiful red color with a slight purple overtone.

If an optical absorption is simply due to an electronic transition between two electronic levels, then the absorption bands should be very sharp. However, for glass containing transition-metal ions the band widths are very broad. This implies that the associated vibrational levels of an excitational state interact with each other in the presence of the ligand field, and also indicates that by altering the composition of the glass, the ligand field strength can be changed. Consequently, variations of bonding strength may shift the absorption spectra and alter the band width. Unlike transition-metal ions, the ligand field is effectively shielded by the outer s and p orbitals of a rare

earth element; thus the electron transitions taking place in inner f orbitals have less ligand field effects. The resulting absorption peaks are much sharper and comparable to that of a free ion.

Color formation in glass arises from excitation of unpaired electrons in the d or f orbitals of the transition-metal ion or the rare earth element incorporated within the glass networks. Colors of transition-metal ion doped materials are particularly subject to change by the variation of the coordination numbers and the splitting of the outer five d energy levels associated with the chemical bonding of the adjacent ions. Therefore the colors in such materials are described as resulting from specific chromophores, which are complex ions that produce a particular optical absorption effect [112]. In contrast, rare earth colorants depending on electron transitions in the inner f shell are much less subject to the local chemical environment of the coloring element; therefore, the change in color with local chemical bonding is minimal [113].

In this chapter are discussed the variations in colors and spectral absorption due to excitation of electrons in the silica gels and gel-glasses containing transition-metal ions. The optical properties are interpreted using the ligand field theory of chromophores. The theories of ligand field and molecular orbital transitions in d-shell colorants are reviewed and applied to the optical spectra of the chemically doped gel glasses. The transition metal elements investigated are Co, Cu, and Ni ion-doped silica gels and gel-glasses. The effects of thermal history are also studied. The results are compared with the spectra of the same elements in melt derived silicate and phosphate glasses.

Review of Literature

Pure silica gel-glass has a very wide optical transmission range from the vacuum ultraviolet, 163 nm (7.60 eV, 61347 cm^{-1}) to the infrared, 4400 nm (0.28 eV, 2272 cm^{-1}) as described in previous chapters. The silica O-Si-O bonding electrons

have a fully filled noble gas electron shell. Consequently, no incoming photon with lower energy than 7.6 eV can excite these strongly bonded electrons to higher quantum levels; as a result pure silica gel glass is transparent and colorless to human eyes.

Coloring is one of the most important arts in human life. Artists since ancient China have tried successfully to preserve their masterpieces forever using vivid colors in porcelain ceramic glazes. The coloring constituents and molecular ratios of the glazes are trade secrets since they can only be developed by way of trial and error.

The most common coloring ingredients found in ceramic arts are the transition metal ions characterized by an incomplete d electron shell, particularly V, Cr, Mn, Fe, Co, Ni, Cu. Rare earth elements, such as Nd, Er and characterized by an incomplete f shell, are less frequently used due to their cost and rareness. Insoluble metallic colorants such as Au are also used but will not be considered in this chapter since the chemistry is so dissimilar to that of the transition-metal ions.

Ligand-field theory, which is a special case of the most general molecular orbital theory, is an alternative to crystal-field theory [114-116] to explain the color formation of transition metal doped silica glasses. In crystal field theory, bonding is treated as electrostatic, derived from the electric field of the ligands viewed as purely ionic species. Thus, in a crystal field method the chemical compound of a transition metal ion is considered as an aggregate of ions and/or dipolar molecules which symmetrically interact with each other electrostatically but do not exchange electrons. Consequently, when any covalency is involved, a pure crystal field theory can not explain the experimental data very well.

The advantage of the ligand field theory is the mixing between the electrons of the central ion and the ligands. This feature of mixed ionic-covalency successfully explains the coloring phenomena for most situations involving transition elements. In this theory, a ligand presents a negatively charged, nonspherical, partially covalent bonded, distorted coordination complex towards the positive central transition-metal ion.

For example, in a free ion of a transition metal the five equivalent d orbitals are depicted spatially as shown in Figure 6-1. The energy level diagram of the five orbitals in a free transition metal ion is also illustrated in Figure 6-2(a). The electrons can be found with equal probability in any of these five orbitals (Figs. 6-1, 6-2(a)). When this positive transition metal ion with partly filled d-orbitals is placed at the center of a regular (undistorted crystal field) octahedron of ligands, represented as point negative charges, the configuration is as shown in Figure 6-3. An interaction of the d orbitals of the central ion with the six ligands in the octahedral field is expected. The two lobes of the d_{z^2} orbital point exactly at the two ligands in the +Z and -Z directions; similarly, the four lobes of the $d_{x^2-y^2}$ orbital point exactly at the four ligands in the plus and minus directions of the X and Y axes. The electrostatic interaction of these two d shells with the negative ligands at the corners of the octahedron is repulsive, consequently, there is a splitting and raising of the energy of these two of the five d energy levels of the system. This leads to the two upper e_g levels for the octahedral ligand field configuration as shown in Figure 6-2(b).

The remaining three sets of d orbitals of Figure 6-1, the d_{xy} , d_{yz} and d_{zx} orbitals, have orientations which protrude halfway between the ligands as shown in Figure 6-4. Because there is no repulsive interactions with the ligands these orbitals will have lower energy levels than the e_g set. Thus, the d_{xy} , d_{yz} and d_{zx} orbitals are shown as the three equal energy t_{2g} levels in Figure 6-2(b).

The energy difference between the e_g and t_{2g} levels called the crystal field splitting, is designated Δ_o . Since the overall energy does not change, the upward and downward movements are inversely proportional to the number of equal energy levels; e.g., the degeneracy. Thus in Figure 6-2(b), the triply degenerate lower energy t_{2g} level moves down $0.4 \Delta_o$, while the upper doubly degenerate e_g level moves up $0.6 \Delta_o$ compared to the unsplit free ion levels (Figure 6-2(b)).

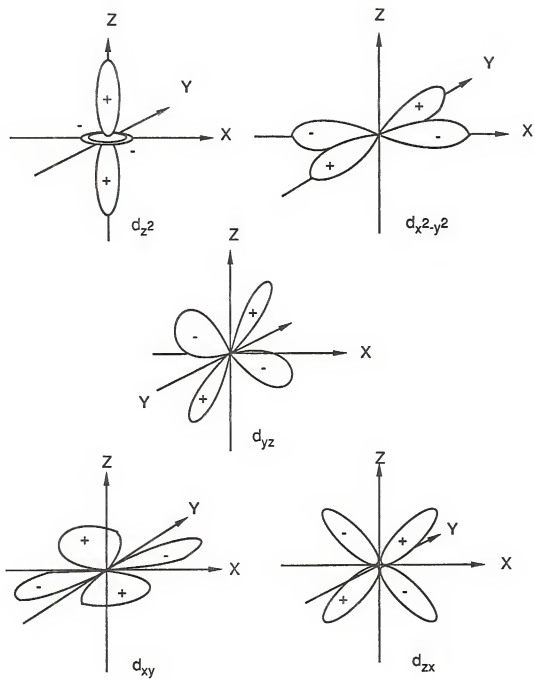


Figure 6-1 Electron distribution shapes of the five equivalent d orbitals.

Ligand configurations:

- (a) five unsplit d orbitals in a free ion.
- (b) five splitted d orbitals in an octahedral field.
- (c) five splitted d orbitals in a tetrahedral field.
- (d) five splitted d orbitals in a tetragonally distorted octahedral field.
- (e) same as (d) but relatively strong distorted.
- (f) five splitted d orbitals in a square planar ligand field.

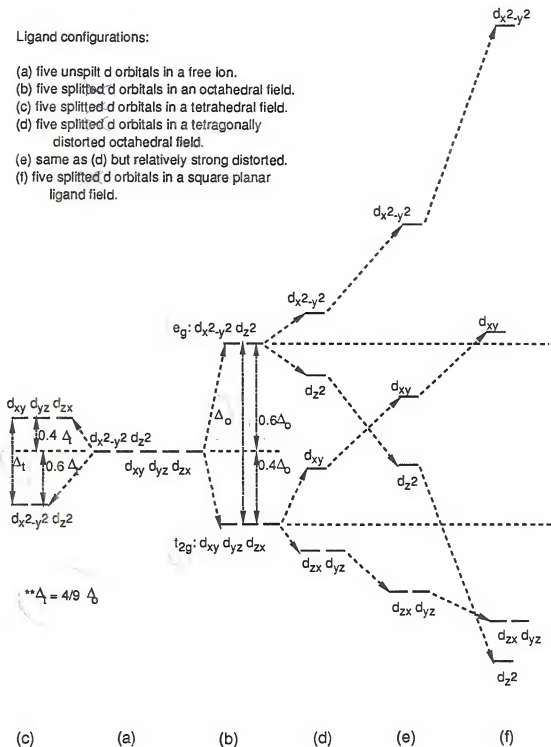


Figure 6-2 Splitting of the five d orbitals in various types of ligand fields.

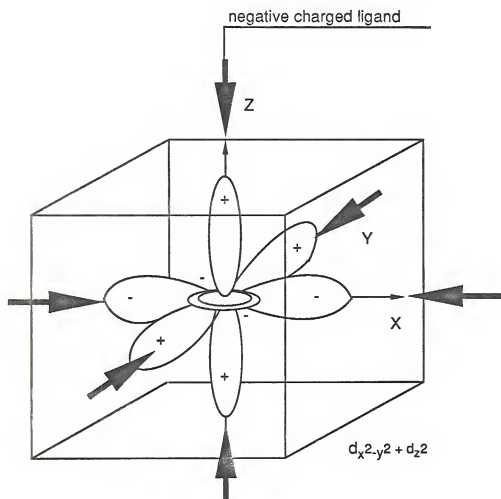
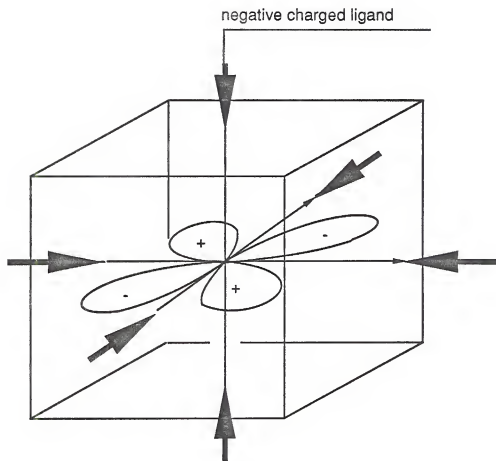


Figure 6-3 Head on interaction of the d_z^2 and $d_{x^2-y^2}$ orbitals of a central ion with six ligands in a octahedral field.



this presents one of d_{xy} , d_{yz} , d_{zx} orbitals

Figure 6-4 Less interaction of the d_{xy} , d_{yz} , d_{zx} orbitals of a central ion with six ligands in an octahedral field.

When the transition-metal ion is in tetrahedral symmetry as shown in Figures 6-5 and 6-6, the situation is reversed. The lobes of the $d_{x^2-y^2}$ or d_{z^2} orbitals now lie in the direction between the ligands, while the lobes of d_{xy} , d_{yz} and d_{zx} orbitals, though not pointing directly towards the ligands, lie closer to them. Thus the t_{2g} (d_{xy} , d_{yz} , d_{zx}) orbitals are destabilized with respect to the e_g orbitals. For the same strength ligands, the tetrahedral scheme Δ_t can be related to the Δ_o value of the degenerate orbitals by $\Delta_t = 4/9 \Delta_o$, as shown in Figure 6-2(c).

Practically, octahedral arrangements of the ligands around the transition-metal ion are often tetragonally distorted. In such a case the two $+Z$ and $-Z$ (d_{z^2}) ligands in Figure 6-3 are gradually moving away from the central transition-metal ion, and new energy differences among the d orbitals arise. The d_{z^2} level will fall and $d_{x^2-y^2}$ level will arise equally at the same time. If the two Z ligands are completely removed, the d_{z^2} level becomes the lowest energy level in the resulting square planar ligand arrangement, since there are now no energy-raising ligands in that direction and the $d_{x^2-y^2}$ becomes the highest energy level, as shown in Figure 6-2(f). For a square planar ligand field the location of the d_{yz} and d_{zx} levels will fall and that of the d_{xy} level must rise two times as much. The frequently observed tetragonally distorted octahedral arrangements are shown in Figure 6-2(d) and (e). Consequently, the kind of energy level arrangement formed by the ligand fields depends on three crucial properties: (1) the orbitals of the central transition-metal ion, (2) the surrounding arrangement of ligand fields, and (3) the strength of the ligand fields.

For ligand fields, in dealing with individual orbitals of an atom, lower case notations such as a_{1g} , b , e_{1g} , t_{2g} are used. Either a or b indicates a nondegenerate orbital with a presenting a wave function which is symmetric with respect to the rotation axis, whereas b represents a wave function which is antisymmetric and changes sign during rotation. The e and t orbitals are symmetrically doubly and triply degenerate. The energy levels in e or t orbitals are equal.

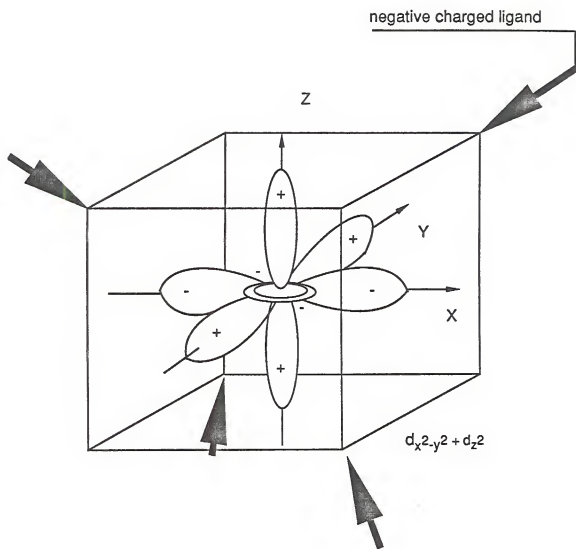
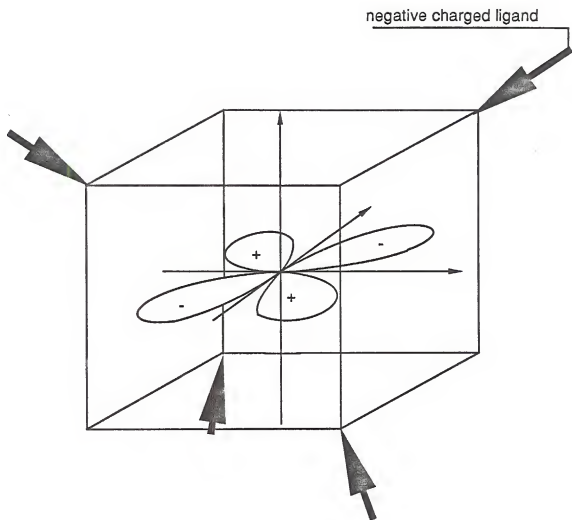


Figure 6-5 Interaction of the d_{z^2} and $d_{x^2-y^2}$ orbitals of a central ion with four ligands in a tetrahedral field.



this presents one of d_{xy} , d_{yz} , d_{zx} orbitals

Figure 6-6 Interaction of one of the d_{xy} , d_{yz} , d_{zx} orbitals of a central ion with four ligands in a tetrahedral field.

Use of the subscript g designates the presence of a change in sign of the wave function on inversion through a center of symmetry. A subscript 1 refers to the presence of mirror planes parallel to the symmetry axis and a subscript 2 refers to mirror planes normal to this axis. Upper case designations such as ${}^2A_{2g}$, 1B_1 , 2E_g , ${}^2T_{2g}$ are generally used to represent the energy levels in the atom, ion, or molecule, with the prefix superscript as the $(2S + 1)$ multiplicity.

The energy states that can accommodate undisturbed or excited electrons in free transition-metal ions having incomplete d orbitals (d^1 to d^9), based on Russell-Saunders coupling [see p. 381-408 in ref. 102], are named to be S, P, D, F, G, H and I corresponding to the quantum number L equal to 0, 1, 2, 3, 4, 5, and 6. These states are listed in Table 6-1 for various transition metals.

In a ligand field the tetrahedral d^9 or d^4 configuration can be viewed as containing one hole; i.e., one electron missing from a full d or half full d shell. This configuration provides a strong analogy with one electron added to an octahedral empty d shell (d^1) or a half filled d shell (d^6) and, conversely, so do the octahedral d^9 or d^4 and the tetrahedral d^1 or d^6 configurations, as shown in Figure 6-7, except that the highest rather than the lowest split orbital is being occupied. The same applies to all other configurations. For example, the tetrahedral d^2 or d^7 configuration has the same sequence of levels as the octahedral d^8 or d^3 and, conversely, so do the octahedral d^2 or d^7 and the tetrahedral d^8 or d^3 configurations. These similarities are shown in Figure 6-8. Consequently, the splitting scheme of d^n (octahedral) configurations is equivalent to that of $d^{(10-n)}$ (tetrahedral) or vice versa. The d^0 and d^{10} configurations corresponding to completely empty or completely full d orbitals cannot show color directly derived from d electronic transitions.

An s^1 orbital is completely symmetrical and hence is unaffected by ligands in an octahedral field such as 2S or A_{1g} . The p^1 orbitals are not split by octahedral fields such as 2P or ${}^2T_{1g}$ since all interact equally as illustrated in Figures 6-9 and 6-10. In an

Table 6-1
Energy levels for transition-metal free ions

Configuration	Example	The lowest energy levels in a free ion
$3d^1 \approx 3d^9$	$3d^1$ (Ti^{3+}) \approx $3d^9$ (Cu^{2+})	$2D$
$3d^2 \approx 3d^8$	$3d^2$ (V^{3+}) \approx $3d^8$ (Ni^{2+})	$3F < 1D < 3P < 1G < 1S$
$3d^3 \approx 3d^7$	$3d^3$ (Cr^{3+} , V^{2+}) \approx $3d^7$ (Fe^+ , Co^{2+})	$4F < 4P < 2G < 2H < 2P$
$3d^4 \approx 3d^6$	$3d^4$ (Cr^{2+} , Mn^{3+}) \approx $3d^6$ (Mn^+ , Fe^{2+} , Co^{3+})	$5D < 3H < 3P < 3F < 3G < 1I$
$3d^5$	$3d^5$ (Cr^+ , Mn^{2+} , Fe^{3+})	$6S < 4G < 4P < 4D < 2I < 4F$

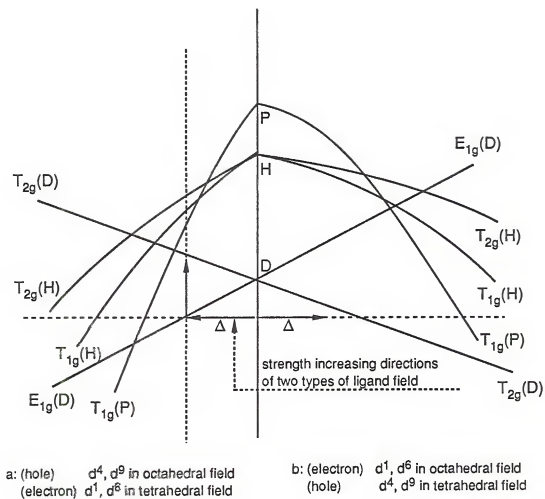


Figure 6-7 Three lowest energy levels for d^1 , d^6 , d^4 , d^9 splitting configurations in octahedral and tetrahedral fields.

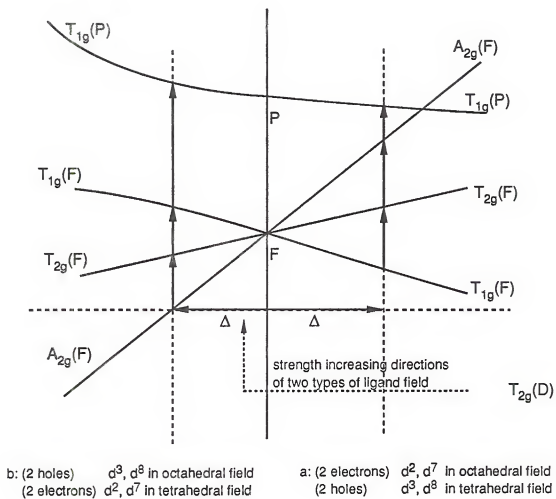


Figure 6-8 Two lowest energy levels for d^2, d^3, d^7, d^8 splitting configurations in octahedral and tetrahedral fields.

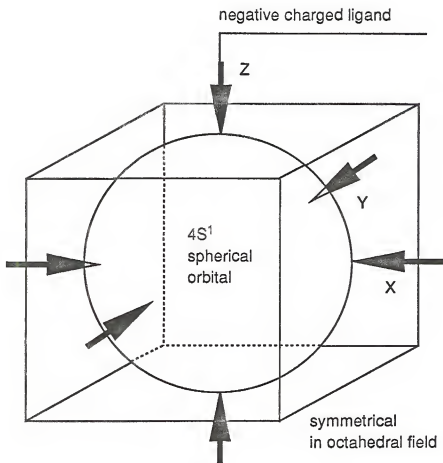


Figure 6-9 All interaction between ligands and $4s^1$ are equal, therefore, no splitting results.

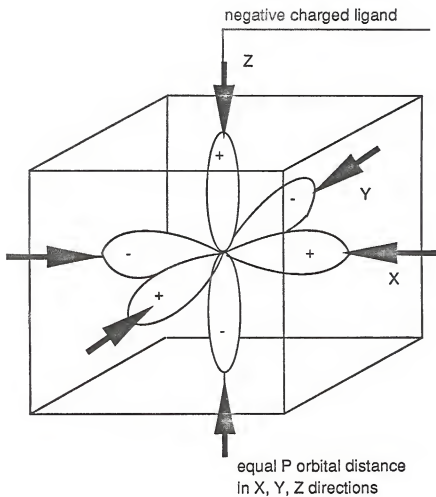


Figure 6-10 All interaction between ligands and $4p^1$ are equal, therefore, no splitting results.

octahedral field the d^1 and d^9 (2D) orbitals, as discussed before, split into T_{2g} (d_{xy} , d_{yz} , d_{zx}) and E_g ($d_{x^2-y^2}$ or d_{z^2}) levels. The f^1 orbitals are split into three levels in an octahedral field: a $^2T_{1g}$ level at $1/3 \Delta$ below, a $^2T_{2g}$ level at $1/9 \Delta$ above, and a $^2A_{2g}$ level $2/3 \Delta$ above the presplit F orbital as shown in Figure 6-11(a).

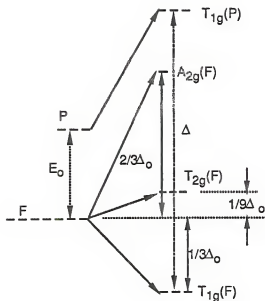
The two split low-energy states 3F and 3P from either the d^2 or the d^8 configuration behave in an octahedral field exactly as the F and P states arising from the $1f$ and $1p$ as discussed above. Consequently, the 3F state is split into $^3T_{1g}(F)$, $^3T_{2g}(F)$ and $^3A_{2g}(F)$ states and the unsplit 3P becomes the $^3T_{1g}(P)$ state. The d^3 or d^7 state has 4P and 4F orbitals. Under a ligand field the 4F splits into $^4T_{1g}(F)$, $^4T_{2g}(F)$ and $^4A_{2g}(F)$ states and the unsplit 4P becomes the $^4T_1(P)$ state, as shown in Figures 6-8 and 6-11(b). The d^4 and d^6 configurations have a low-energy state 5D which splits into $^5T_{2g}$ (d_{xy} , d_{yz} , d_{zx}) and 5E_g ($d_{x^2-y^2}$ or d_{z^2}) in an octahedral field (Figures 6-7 and 6-11(c)). The d^5 state has an unsplit 6S or 6A_1 level in the octahedral field.

As mentioned above, ligand field theory describes the bonding occurring between center transition-metal ion and the ligands. Molecular orbital theory, which develop the combination of the atomic orbitals of the atoms to form the molecule, is used to explain this bonding phenomenon.

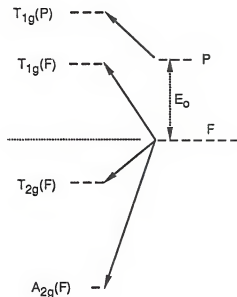
The condition for two atoms to form: (1) a bonding molecular orbital (ψ_b), (2) a nonbonding molecular orbital, or (3) an antibonding molecular orbital (ψ_a) depends on S , the wave function overlap integral $\int \psi_a \psi_b dt$ of the probability equation ($\psi_b^2 dt = \int \psi_a^2 dt + \int \psi_b^2 dt + \int \psi_a \psi_b dt$, where ψ_A and ψ_B are the wave functions of atoms A and B) for finding an electron within the space. Bonding takes place only when the value of S is positive ($S > 0$) and the bonding strength (energy) is proportional to the extent of the overlap of the atomic orbitals. The bonding energy level is reduced relative to the level of the free atoms by the same amount as the energy is increased for the antibonding level.

In the case of 3d transition-metal ions in an octahedral field, the $d_{x^2-y^2}$ and d_{z^2} configurations are in the direction of the ligands. This results in a positive overlap and a

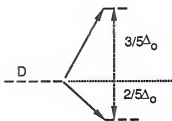
(a) octahedral field
 d^2 (V^{3+})
 d^7 (Co^{2+})



(b) tetrahedral field
 d^3 (V^{2+} , Cr^{3+})
 d^8 (Ni^{2+})



(c)



octahedral field:
 d^1 (Ti^{3+})
 d^6 (Fe^{2+} , Co^{3+})



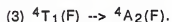
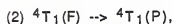
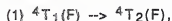
tetrahedral field:
 d^4 (Cr^{2+} , Mn^{3+})
 d^9 (Cu^{2+})

Figure 6-11 The splitting of d orbitals (a), (b) for P, F states, (c) for D state in octahedral and tetrahedral ligand field.

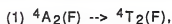
reduction (e_g , bonding) and an increase (e_g^* , antibonding) in energy levels. The t_{2g} (d_{xy} , d_{yz} , d_{zx}) levels are located between the ligands, and no overlap is observed. As a result, the energy levels of t_{2g} remain unchanged in the presence of the ligand field as shown in Figure 6-12(c). The 4s orbital of transition-metal ions has a (a_{1g}) spherical symmetry and a corresponding ligand group orbital that is composed of sigma bonds which are cylindrically symmetrical about the internuclear axis (Figure 6-13). The 4p (t_{1u} bonding and t_{1u}^* antibonding) orbitals with the related ligand group orbitals are shown in Figure 6-14.

The 12 electrons from the ligand group orbitals are perfectly paired into three lowest energy molecular orbitals which are $a_{1g}(1)$, $t_{1u}(3)$ and $e_g(2)$, as shown by the heavy arrows in Figure 6-12(c). Consequently, the d electrons from the transition-metal ions have to fill the $t_{2g}(3)$ levels first. If there are any remaining electrons then the $e_g^*(2)$ levels available. If the energy gap, Δ , is greater than kT , low-spin configurations will be formed. The gap energy, Δ , is generally in the visible range of 1 eV (NIR) to 3 eV (UV) energy. If electromagnetic radiation has the same amount of energy as the gap energy, i.e. $\Delta = h\nu$ (photon energy), then the electronic transitions from $t_{2g}(3)$ to $e_g^*(2)$ levels takes place.

These theories of ligand field and molecular orbital transitions are the basis for interpreting the optical spectra of Co^{2+} ion doped, Ni^{2+} ion doped and Cu^{2+} ion doped silica gels. The possible energy level transitions for the Co^{2+} ion in both d^7 octahedral and tetrahedral symmetries are analyzed by means of Figures 6-8(a) and (b). The octahedral Co^{2+} configuration is predicted to have three spin-allowed transitions:



The tetrahedral Co^{2+} configuration is expected to have three major transitions:



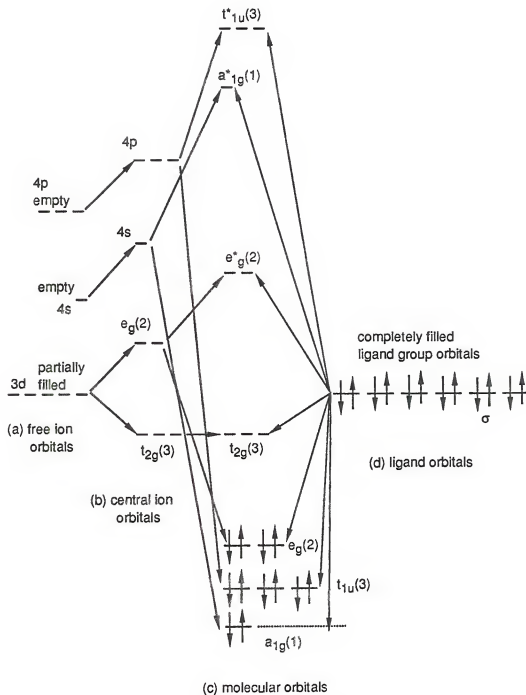
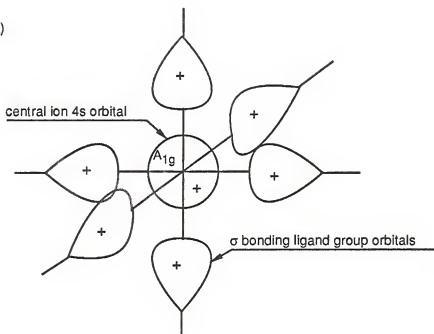


Figure 6-12 Molecular orbital splitting levels for a d orbital ion in an octahedral environment with ligands having only σ bonds.

(a)



(b)

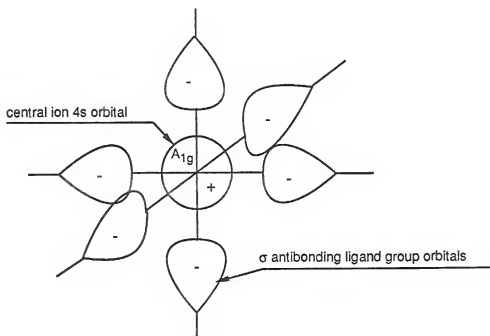


Figure 6-13 Ligand group orbital and central matching atomic orbitals of the bonding symmetry.

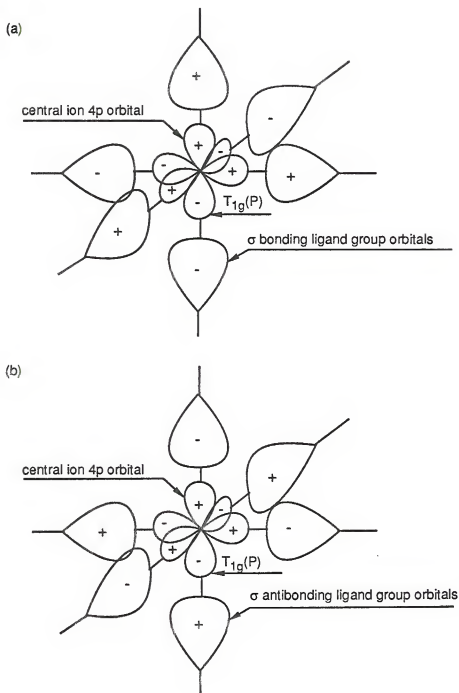
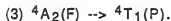
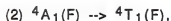
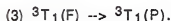
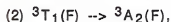
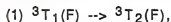


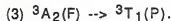
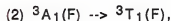
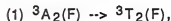
Figure 6-14 Ligand group orbital of only σ bonds and matching atomic orbitals to form molecular orbitals.



The energy level diagram for the Ni^{2+} ion in d^8 tetrahedral and octahedral symmetries is also depicted in Figures 6-8(a) and (b). The tetrahedral Ni^{2+} configuration has three spin-allowed transitions:



The octahedral Ni^{2+} symmetry results in three major transitions:



The Cu^{2+} ion has a $3d^9$ configuration, an inverted d^1 configuration, as shown in Figure 6-7. The major transition is attributed to ${}^2E \rightarrow {}^2T_2$, as is also shown in Figure 6-7(a).

Experimental Procedure

Seven steps are generally used in making the monolithic silica gels and glasses containing transition-metal elements: (1) mixing, (2) casting, (3) gelation, (4) aging, (5) drying, (6) impregnation and (7) densification described in Example Two in Chapter 2. In the mixing stage, it is necessary to select a suitable drying control chemical additives, such as formamide, glycerol, nitric acid, or an organic acid, in order to make monoliths rapidly without: (1) precipitation, (2) formation of an inhomogeneous gel, or (3) crystallization. By use of nitric acid in this system it was possible to produce non-crystalline homogeneous optical silica gels and glasses. To our knowledge, monolithic gels containing the transition and rare earth elements mentioned in Chapter 2 have not previously been described.

The examples used for this investigation were Co^{II} , Ni^{II} and Cu^{II} colored silica monoliths. The first step involved mixing 60 cc (1N) nitric acid DCCA with 340 cc of distilled water for 5 minutes at room temperature, followed by adding to the nitric acid water solution 200cc of TMOS with mixing at 85°C for no more than 60 minutes. This well mixed sol was then cast into a polystyrene mold (20 mm H x 100 mm D, a disk shape) at room temperature. Gelation occurred in the mold at 55°C in about 115 minutes, followed by aging at 55°C for 10 hours and followed by aging at 80°C for 15 hours. The aged silica gel was taken from the molds and dried with a controlled evaporation rate, as described in Section II of Chapter 2. The drying was initially at 70°C with the temperature gradually increasing to 160°C during a 90 hour period. Before impregnation, the gel was stabilized to 800°C at 10°C/hour to increase the strength and density and make it possible to perform a nondestructive doping process. The stabilized gel was then immersed into a 0.25 gram-percent Co^{II} nitrate or a 0.30 gram-percent Ni^{II} nitrate or an one gram-percent Cu^{II} nitrate water solution for 24 hours. The solution doping followed by drying at 160°C for 12 hours to remove the pore solvent. Subsequent thermal treatments to 850°C and 900°C were done in ambient air.

The transmission spectra of the 160°C Co^{II} and Cu^{II} doped silica gel glasses and the 850°C, 900°C Co^{II} doped silica gel glasses were obtained in the visible range from 200 nm to 900 nm using a Perkin-Elmer UV-VIS spectrophotometer model 552. The transmission spectra of the 160°C Ni^{II} doped silica gel glass was performed in the UV-VIS-NIR range from 200 nm to 1300 nm using a Perkin-Elmer Lambda 9 UV-VIS-NIR spectrophotometer.

Results and Discussions

The silica gel samples containing 0.25% Co were heated to certain temperatures. The color of the 160°C Co^{II} gel is reddish pink. The color of the 850°C sample is deep blue, and the 900°C sample has a greenish black color. The UV-Visible spectra

characteristic of these three Co^{II} -silica gel samples are shown in Figure 6-15. There is a totally different absorption curve for the 160°C pink sample than for the 850°C blue sample and the 900°C green sample. Since the color of transition ions such as cobalt in silicate glasses depends primarily on the outer d valence orbitals, it means that the color and absorption spectra depends on the oxidation state and coordination number of the ion. The temperature sensitivity of the Co^{II} -silica gel absorption spectra indicates a shift in oxidation state and coordination number (CN). The low-temperature gel shows evidence of a sixfold CN similar to that reported for Co^{II} in metaphosphate glasses [117] and 10 mol% Na_2O -borate glass [see p. 241 in ref. 112], as shown in Figure 6-16. Thus, it is reasonable to assume that the Co^{II} ion in the silica gel in octahedral symmetry.

The major absorption band of the Co^{II} ion is due to the ${}^4\text{T}_1(\text{F})$ to ${}^4\text{T}_1(\text{P})$ transition (see Figure 6-16). The high energy shoulder at 470 nm is a consequence of spin-orbit coupling in the ${}^4\text{T}_1(\text{P})$ state [9]. The ${}^4\text{T}_1(\text{F})$ to ${}^4\text{T}_2(\text{F})$ transition occurs in the infrared region around 1250 nm and does not contribute to color formation. The ${}^4\text{T}_1(\text{F})$ to ${}^4\text{A}_2(\text{F})$ transition is expected to be at 555 nm. However, this transition is very weak because it involves the forbidden two-electron jump [118]. This weakness combined with the closeness of the major ${}^4\text{T}_1(\text{F})$ to ${}^4\text{T}_1(\text{P})$ transition makes the ${}^4\text{T}_1(\text{F})$ to ${}^4\text{A}_2(\text{F})$ transition unresolved.

In contrast, the high-temperature (850°C and 900°C) Co^{II} doped gels appear to have a CN of 4. This fourfold coordination is more equivalent to that of a standard vitreous silicate glass [119] (see Figure 6-17), that is,



The main absorption band in 550 nm to 700 nm range of this tetrahedral Co^{II} ion is due to the ${}^4\text{A}_2(\text{F})$ to ${}^4\text{T}_1(\text{P})$ transition. As shown in Figure 6-17, the Co^{II} doped high-temperature gel shows evidence of a fourfold CN similar to that for Co^{II} ion in fused

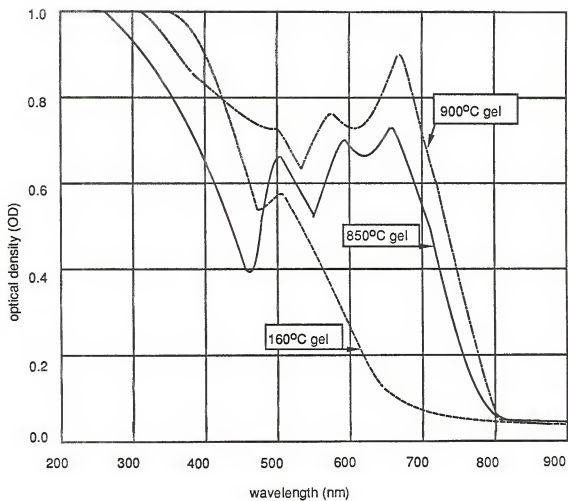


Figure 6-15 Spectra of three Co^{II}-doped silica gel samples at 160°C, 850°C, and 900°C.

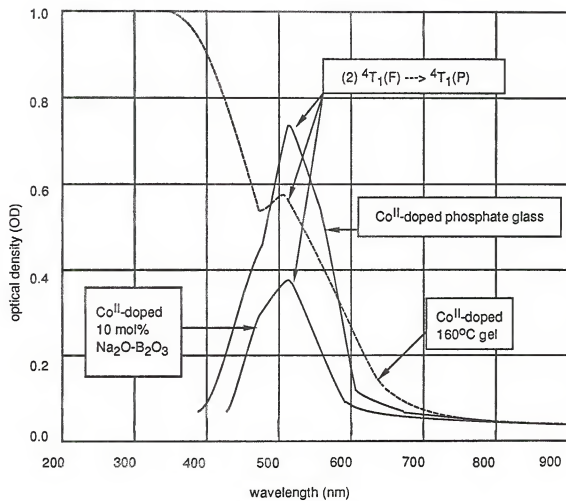


Figure 6-16 Spectra of 160°C Co^{II}-doped silica gel samples and some Co^{II}-doped melted glasses.

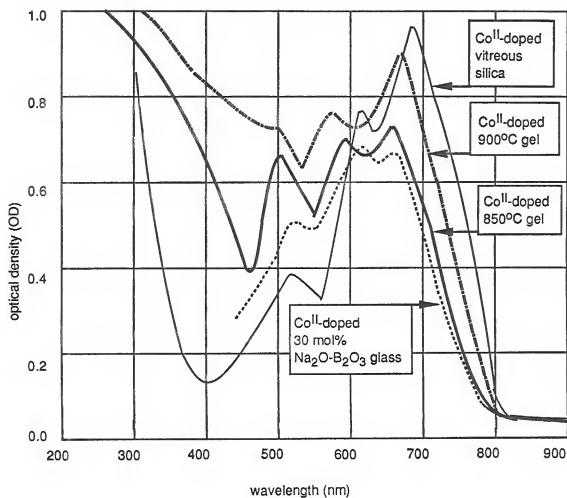


Figure 6-17 Spectra of 850°C, 900°C Co^{II}-silica gel samples and two Co^{II}-doped melted glasses.

silica and a binary 30 mol% Na₂O-borate glass.

The splitting of the $^4A_2(F)$ to $^4T_1(P)$ band is caused by spin-orbit coupling which splits the $^4T_1(P)$ states and allows the transitions to the neighboring doublet states to gain in intensity [see p. 241-242 in ref. 112]. The two other transitions, $^4A_2(F)$ to $^4T_2(F)$ and $^4A_2(F)$ to $^4T_1(F)$ which take place in the infrared region contribute no color chromophores. In this study, none of the spectra for the Co^{II} doped silica gels is identical to the silicate melt glass spectrum in detail. This indicates that the ligand field strength (Δ) may be varied by the thermal history of the gels.

The spectrum of a 160°C Ni^{II} doped silica gel is similar to that of a 16.2 wt.% melt K₂O-borate glass containing Ni ion. It is also similar to that of a [Ni(H₂O)₆]²⁺ octahedral complex in water [see p. 242-243 in ref. 112], as shown in Figure 6-18. The absorption band at 700 nm of Ni²⁺ in an octahedral complex is assigned to the $^3A_1(F) \rightarrow ^3T_1(F)$ transition, and the one at about 400 nm is assigned to the $^3A_2(F) \rightarrow ^3T_1(P)$ transition. Another band corresponding to a $^3A_2(F) \rightarrow ^3T_2(F)$ transition is observed in the infrared region at about 1180 nm. In this study, the spectra of these three samples are almost the same except for the difference in absorption intensity. The similarity in absorption bands of the three curves indicates that the same ligand field strength acts on Ni²⁺ ion in these three samples.

The absorption spectrum of Cu^{II} in a 160°C gel and three binary sodium-borate Cu^{II} melt glasses [120] are shown in Figure 6-19. All the absorption spectra consist of a broad band with a maximum at about 780 nm. This absorption is attributed to the transition from 2E levels to 2T_2 levels. The band is asymmetric and departs from Gaussian symmetry since the 2T_2 levels are split by a distorted low symmetry ligand field component. No significant band shift and shape change is present in spite of the variations of the surrounding ligand chemical composition of the ligands.

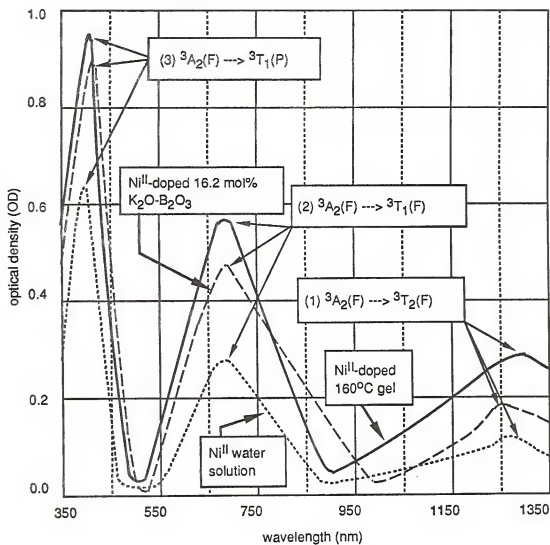


Figure 6-18 Absorption spectra of a Ni^{II}-doped silica gel sample, a Ni^{II} water solution and a Ni^{II}-doped 16.2 mol% K₂O-B₂O₃ glass.

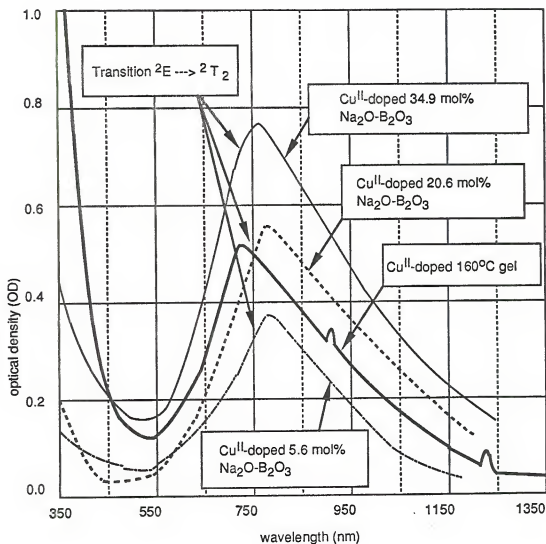


Figure 6-19 Absorption spectra of Cu^{II} -doped silica gel sample and three Cu^{II} -doped sodium-borate glasses.

Conclusions

Thermal history can alter the chemical environment and ligand-field around a transition metal ion in a silica gel and have a marked effect on its optical absorption characteristics and hence on the color produced. These results show that it is possible to take advantage of low temperature sol-gel-glass techniques to manufacture various optical filters using a silica matrix. The absorption spectra can be shifted by controlling the thermal history of silica gels containing transition elements. The optical components produced will have the unique physical properties of silica as discussed in previous chapters, that is, low thermal expansion coefficients, extraordinarily high chemical durability, and superb thermal shock resistance. In addition, depending upon the extent of densification reached during thermal processing the density and index of refraction of the optical component can be varied over wide ranges. The flexibility of the sol-gel technique offers such new exciting processing methods in the production of a variety of optical components. The silica gel glasses chemically doped with transition-metal ions (Co, Ni, Cu ions) discussed in this chapter have demonstrated the possibilities of producing a variety of products including strategic high-tech optical glasses with specific wavelength filtration capabilities, high-tech commercial sun glasses, and tuneable laser glasses.

CHAPTER 7 CONCLUSIONS AND RECOMMENDATIONS

Sol-gel processing offers a new manufacturing method for high technology ceramics and glasses since it allows structural manipulation down to the molecular scale in the nanometer range. Thus, ultrahigh purity and extreme molecular homogeneity of a material may be achieved.

Two major chemical reactions, hydrolysis and polymerization, are involved in sol-gel ultrastructure processing. Hydrolysis enables the organometallic chemical precursor to react to form a monomer on the atomic scale, which is composed of a positive metallic ion surrounded by an anionic complex (e.g., $\text{Si}^{+4}(\text{OH}^-)_4$, $\text{Ti}^{+4}(\text{OH}^-)_4$, $\text{Al}^{+3}(\text{OH}^-)_3$, $\text{Si}^{+4}(\text{CH}_3^-)_4$ etc.). This step is followed by a polymerization based growth process which links the monomers together.

In recent years special optical applications require silica components that meet very stringent requirements. Sol-gel processing applied to silica offers the potential for producing a new generation of silica glasses to meet these requirements for optical and electro-optical applications. The quality of gel-silica glasses expected to meet these stringent requirements are (1) very high purity, (2) extremely low optical signal loss, (3) very high chemically homogeneous doping, (4) very high optical homogeneity. These features make gel-silicas able to upgrade the optical performance in a wide range of precise optical apparatus including lenses, mirrors, waveguides, optical fibers, integrated optoelectronics, and host materials for filters, lasers, and non-linear optical elements or compounds. Therefore, achieving a chemically optimized sol-gel processing for silica optical monoliths was the focus of this study.

The first major difficulty faced in producing large monolithic gel glass for optical components was cracking during drying. In this study the problem was overcome by use of drying control chemical additives (DCCA) and a special designed drying chamber described in Chapter 2.

A fibrillar structure of a silica gel can be formed in the initial preparation of silicic solution. Once the ratio of silica precursor, water and DCCA is fixed the fibrillar structure of the gel is determined. Further evolution of the structure is a function of time and temperature. A relatively strong gel was made using an acidic DCCA which enabled the gel to endure the catastrophic capillary forces developed inside the gel during drying. In addition, the introduction of special drying chamber for ambient atmosphere control also reduced the capillary stress significantly. Monolithic dried (physical water free) gels as large as 10 cm x 8 cm x 2.0 cm (up to the capability of the experimental facility) were routinely produced. The first goal was achieved.

The dried gel monoliths were partially densified in an ambient air furnace up to 860°C. The characterization of these partially densified silica gels was performed by use of (1) structural information tests (x-ray diffraction, BET), (2) Optical information tests (refractive index, FTIR, UV-VIS-NIR), (3) thermal information tests (DSC, DTA, TGA, TMA), (4) mechanical information tests (flexural strength, compressive strength, microhardness, toughness, density).

The results of structural information tests showed that the gels were an amorphous phase with high a volume, and tremendous surface area of uniform open pores throughout the entire body with chemisorbed hydroxyl groups being a function of temperature.

The conclusion of optical information test proves that the index of refraction is a function of sintering temperature and the index has a linear relationship with density as predicted by the Lorentz-Lorenz equation. The -OH absorption bands and UV cut-off is also a function of sintering temperature.

The thermal information tests indicate that the decomposition and evaporation weight losses due to loss of residual organic compounds and water take place below 450°C. Dimensional shrinkage occurs throughout the entire heating program.

The results of mechanical information tests show that the compressive strength, maximum strain to fracture, flexural strength, Young's modulus, and microhardness are linearly proportional to the gel density. These values show a tendency to approach the values of fused silica as the gel densification temperature increases. The K_{IC} /density data obtained show the 160°C gel has a greater toughness than the value for fused silica proving the fibrillar gel structure can absorb higher impact energy than fused silica before cracking.

The second major difficulty to be overcome in producing large monolithic gel glass for optical components was the surface silanol groups inside the porous silica gel which terminated the -O-Si-O- bridging bonds and degenerated the optical performance significantly. A dehydration thermal treatment using carbon tetrachloride was accomplished. Monolithic samples of fully dehydrated and densified monolithic pure silica gel-glass were routinely reproduced.

The tests of the dehydrated densified gel-silica monoliths yielded very important results. A very high optical transmission was achieved throughout the entire spectral range between 165 nm and 4400 nm in the VUV-UV-VIS-NIR spectra. The vuv cut-off wavelength was at 162 nm. These results were equivalent to the very best Type IV commercial silicas. The CTE data of the gel-silica had almost three times lower (2.0×10^{-7}) values than that of Corning 7940 pure silica (5.5×10^{-7}). Thus, the monolithic gel-silica glass greatly improved the optical transmission and significantly lowered thermal expansion of traditional Type I-IV silica glasses. Equivalent or superior levels of homogeneity, strain, bubbles and striae were also achieved. The second goal of this study was reached.

Applications are nearly unlimited for use of the silica sol-gel technology developed herein. The possibility of using the porous gel monoliths for second phase doping was the third goal pursued. Monolithic partially densified optical silica-gel filters impregnated with transition-metal ions (i.e., Cu^{+2} , Ni^{+2} , and Co^{+2} ions) were successfully made. Color changes of these transition-metal ion doped gels that resulted from different densification temperature were interpreted using ligand field and molecular orbital theories. The third goal in this study was achieved.

The highest quality of pure silica made in the world today is that of optical fibers fabricated by vapor phase plasma reaction of ultrapure oxygen with ultrapure silicon tetrachloride (Type IV silica). This process results in fibers of ultralow loss (about 1.0 dB/Km to 5.0 dB/Km) in the 900 nm to 1300 nm range. It is already shown in this study that the fully dehydrated, completely densified, gel-glass monoliths are of such a quality as to compare with the best Type IV optical silica fibers. However, the temperature of densification has been reduced to 1150°C. The sol-gel silica process has the additional advantage that net shape casting of optical components is very simple, also localized densification can be achieved yielding a new approach for producing waveguides in a pure silica matrix (i.e., integrated optics)

The vuv cut-off at 162 nm indicates that the gel-glass is not yet an ideal silica glass. Test data from neutron activation analysis showed that the impurity levels in the first generation silica gel-glass were reduced to several ppb or even better than that of Type IV silica. However, a significant chlorine content, at a value 0.1 wt%, was present which caused a serious problem of the increasing of index of refraction and foaming of a sintered gel-glass above 1300°C. In addition, chlorine terminates the bridging oxygen bond, limits the theoretical silica performance, and create a possible optical absorption center in high energy electromagnetic radiation fields (e.g., x-ray, gamma ray). Elimination of the chlorine impurity is the most important subject for improvements in sol-gel processing if the ultimate performance in silica glass is required.

There is no difficulty for the sol-gel process to prepare an extremely intimate and chemically homogeneous sol to form a molecularly uniform gel. The optical homogeneity problem due to localized density and chlorine fluctuations could be improved by developing further optimization of the thermal dehydration densification process. This will require modification of the atmosphere control system of the furnace.

Use of the chemical doping technique for porous gel-silica could lead to produce a new category of multicomponent glasses. For instance, a colorful and fascinating world in the transition-metal and rare earth elements doped gel-glasses is waiting for further exploration. Oxidation states and ligand fields can be stabilized within the gel-silica matrix that are not possible using traditional high temperature melt derived glasses.

REFERENCES

1. B. Jirgensons and M. E. Straumanis, Colloid Chemistry, Macmillan Co., New York, 1962.
2. Ralph K. Iler, The Colloid Chemistry of Silica and Silicates, Cornell University Press, Ithaca, New York, 1955.
3. P. J. Flory, Gels. A Introduction Lecture, Faraday Discussions of the Chemical Society, Vol. 57, 1974, p. 7-18.
4. Ralph K. Iler, The Chemistry of Silica, John Wiley & Sons, Inc., New York, 1979.
5. R. H. Doremus, Chemical Durability of Glass, in Treatise on Materials Science and Technology Volume 17, Glass II, Miknoru Tomozawa and Robert H. Doremus, eds., Academic Press, Inc., New York, 1979, p. 41-69.
6. C. J. Brinker, K. D. Keefer, D. W. Schaefer and C. S. Ashley, Sol-Gel Transition in Simple Silicate, Journal of Non-Crystalline Solids, Vol. 48, 1982, p. 47-64.
7. L. C. Klein, Sol-Gel Glass Technology. A Review, Glass Ind., 1981, p. 14-16.
8. J. D. Mackenzie, Fusion of Quartz and Cristobalite, Journal of the American Ceramic Society, Vol. 43, 1960, p. 615-620.
9. Martin Grayson, ed., Encyclopedia of Glass, Ceramics, and Cement, John Wiley & Sons, Inc., New York, 1985, p. 837-845.
10. N. J. Kreidl, Inorganic Glass-Forming Systems, Part I: Vitreous Silica, in Glass: Science and Technology Vol. 1: Glass-Forming Systems, Academic Press, Inc., New York, 1983, p.107-121.
11. J. D. Mackenzie, Glasses from Melts and Glasses from Gels. A Comparison, Journal of Non-Crystalline Solids, Vol. 48, 1982, p. 1-10.
12. L. L. Hench, Concepts of Ultrastructure Processing, in Ultrastructure Processing of Ceramics, Glasses and Composites, L. L. Hench and D. R. Ulrich, eds., John Wiley & Sons, Inc., New York, 1984, p. 3-5.
13. Sumio Sakka, Gel Method for Making Glass, in Treatise on Materials Science and Technology Volume 22, Glass III, Miknoru Tomozawa and Robert H. Doremus, eds., Academic Press, Inc., New York, 1982, p. 129-169.
14. I. Artaki, M. Bradley, T. Zerda, Jiri Jonas, G. Orzel, and L. L. Hench, NMR, Raman Study of the Effect of Formamide on the Sol-Gel Process, in Science of Ceramic Chemical Processing, L. L. Hench and D. R. Ulrich, eds. John Wiley & Sons, Inc., New York, 1986, pp. 73-80.

15. L. L. Hench, Use of Drying Control Chemical Additives (DCCAs) in Controlling Sol-Gel Processing, in Science of Ceramic Chemical Processing, L. L. Hench and D. R. Ulrich, eds., John Wiley & Sons, Inc., New York, 1986, p. 52-63.
16. G. Ortel and L. L. Hench, Effect of the Use of a Drying-Control Chemical Additive (DCCA) on the Crystallization and Thermal Behavior of Soda Silicate and Soda Borosilicate, Proceedings of the 8th Annual Conference on Composites and Advanced Ceramic Materials, Cocoa Beach, Florida, January 15-18, 1984.
17. S. Wallace and L. L. Hench, Metal Organic Derived 20L Gel Monoliths, Proceedings of the 8th Annual Conference on Composites and Advanced Ceramic Materials, Cocoa Beach, Florida, January 15-18, 1984.
18. Donald R. Ulrich, Chemical Science's Impact on Future Glass Research, Ceramic Bulletin, Vol. 64, No. 11, 1985, p. 1444-1448.
19. S. H. Wang and L. L. Hench, Drying Control Additives for Rapid Production of Large Sol-Gel Monoliths Containing Transition and Rare Earth Elements, patent pending, Serial No. 704917, 1985.
20. Gerard Ortel and L. L. Hench, Effect of Formamide Additive on the Chemistry of Silica Sol-Gels, Journal of Non-Crystalline Solids, Vol. 79, 1986, p. 177-194.
21. J. Lyklema, The Determination of the IEP and the PZC in Silicic Solution, Faraday Discussions of the Chemical Society, No. 52, 1971, p. 318-325.
22. R. L. Mozzi and B. E. Warren, Structure of Vitreous Silica, Journal of Appl. Cryst., Vol. 2, 1969, p.164 -172 .
23. W. D. Kingery, H. K. Bowen and D. R. Uhlmann, Introduction to Ceramics, 2nd ed., John Wiley & Sons, Inc., New York, 1976, p. 95-108.
24. D. E. Clark, C. G. Pantano and L. L. Hench, Corrosion of Glass, Books for Industry, Div. of Magazines for Industry, New York, 1979.
25. M. Prassas, J. Phalippou and J. Zarzycki, Sintering of Monolithic Silica Aerogels, In Science of Ceramic Chemical Processing, L. L. Hench and D. R. Ulrich, eds., John Wiley & Sons, Inc., New York, 1986, p. 156-167.
26. J. Wong and C. A. Angell, Glass Structure by Spectroscopy, Marcel Dekker, Inc., New York, 1976.
27. Michael L. Hair, Infrared Spectroscopy in Surface Chemistry, Marcel Dekker, Inc., New York, 1967.
28. E. M. Rabinovich, D. L. Wood, D. W. Johnson Jr, D. A. Fleming, S. M. Vincent and J. B. MacChesney, Elimination of Cl₂ and H₂O in Gel Glasses, Journal of Non-Crystalline Solids, Vol. 82, 1986, p. 42-49.
29. B. N. Figgis, Introduction to Ligand Fields, John Wiley & Sons, Inc., New York, 1966.

30. L. C. Klein and G. J. Garvey, Monolithic Dried Gels, *Journal of Non-Crystalline Solids*, Vol. 48, 1982, p. 97-104.
31. M. Decottignies, J. Phalippou and J. Zarzycki, Synthesis of Glasses by Hot-Pressing of Gels, *Journal of Materials Science*, Vol. 13, 1978, p. 2605-2618.
32. J. Phalippou, M. Prassas and J. Zarzycki, Crystallization of Gels and Glasses Made from Hot-Pressed Gels, *Journal of Non-Crystalline Solids*, Vol. 48, 1982, p. 17-30.
33. R. Roy, Gel Route to Homogeneous Glass Preparation, *Journal of American Ceramic Society*, Vol. 52, 1969, p. 344-345.
34. B. E. Yoldas, Monolithic Glass Formation by Chemical Polymerization, *Journal of Materials Science*, Vol. 14, 1979, p. 1843-1849.
35. G. Carturan, V. Gottardi and M. Graziani, Physical and Chemical Evolutions Occurring in Glass Formation from Alkoxides of Silicon, Aluminum and Sodium, *Journal of Non-Crystalline Solids*, Vol. 29, 1978, p. 41-47.
36. M. Yamane, S. Aso, S. Okano and T. Sakaino, Preparation of a Gel from Metal Alkoxide and Its Properties as A Precursor of Oxide Glass. *Journal of Materials Science*, Vol. 13, 1978, p. 865-871.
37. L. L. Hench and Gerard Orcel, Physical-Chemical and Biochemical Factors in Silica Sol-Gels, *Journal of Non-Crystalline Solids*, Vol. 82, 1986, p. 1-10.
38. Gerard Orcel, The Chemistry of Silica Sol-Gel, Ph. D. Dissertation, University of Florida, Gainesville, Florida, 1987.
39. Z. Z. Vysotskii and D. N. Strazhesko, The Role of Polymerization and Depolymerization Reactions of Silicic Acid, etc., in D. N. Strazhesko, ed., Adsorption and Adsorbents, John Wiley & Sons, Inc., New York, 1974, p. 55-75.
40. C. Okkerse, Chapter 5: Porous Silica, in Physical and Chemical Aspects of Adsorbents and Catalysts, B. G. Linsen, ed., Academic, New York, 1970, p. 214-219.
41. S. G. De Bussetti, M. Tschapek, and A. K. Helmy, Calorimetric Determination of the Point of Zero Charge, *Journal of Electroanalytical Chemistry and Interfacial Electrochemistry*, Vol. 36, 1972, p. 507-511.
42. Ralph K. Iler, Polymerization of Silica Acid: Retarding Effect of Chromate Ion, *Journal of Physical Chemistry*, Vol. 56, 1952, p. 678-679.
43. Ralph K. Iler, Chapter 2: Dissolution and Polymerization of Silica, in Surface and Colloid Science, Vol. 6, E. Matijevic, ed., John Wiley & Sons, Inc., New York, 1973, p. 4-15.
44. Michael D. Sacks and Rong-Sheng Sheu, Rheological Characterization During the Sol-Gel Transition, in Science of Ceramic Chemical Processing, L. L. Hench and D. R. Ulrich, eds. John Wiley & Sons, Inc., New York, 1986, p.100-107.

45. Paul J. Flory, Condensation Polymerization and Constitution of Condensation Polymers, in R. E. Burk and Oliver Grummitt, eds., High Molecular Weight Organic Compounds (Frontiers in Chemistry, Vol. VI), Interscience Publishers, New York, 1949, p. 211-283.
46. Paul J. Flory, Fundamental Principles of Condensation Polymerization, Chemical Reviews, Vol. 39, 1946, p. 137-197.
47. Ralph K. Iler, Inorganic Colloids for Forming Ultrastructures, in Science of Ceramic Chemical Processing, L. L. Hench and D. R. Ulrich, eds., John Wiley & Sons, Inc., New York, 1986, p. 3-20.
48. J. Zarzycki, Monolithic Xero- and Aerogels for Gel-Glass Processes, in Ultrastructure Processing of Ceramics, Glasses and Composites, L. L. Hench and D. R. Ulrich, eds., John Wiley & Sons, Inc., New York, 1984, p. 27- 42.
49. David R. Gaskell, Introduction to Metallurgical Thermodynamics, 2nd ed. McGraw-Hill Book Co., New York, 1981.
50. J. F. Goodman and S. J. Gregg, The Production of Active Solids by Thermal Decomposition, Part X: Heat Treatment of the Xerogels of Silica, Journal of the Chemical Society, Vol. 1, 1959, p. 694-698.
51. S. Sakka and K. Kamiya, The Sol-Gel Transition in the Hydrolysis of Metal Alkoxides in Relation to the Formation of Glass Fibers and Films, Journal of Non-Crystalline Solids, Vol. 48, 1982, p. 31-46.
52. B. E. Yoldas, Effect of Molecular Separation on the Hydrolytic Polycondensation of $\text{Si}(\text{OC}_2\text{H}_5)_4$, Journal of Non-Crystalline Solids, Vol. 82, 1986, p. 11-23.
53. Michel Prassas and L. L. Hench, Physical Chemical Factors in Sol-Gel Processing, in Ultrastructure Processing of Ceramics, Glasses and Composites, L. L. Hench and D. R. Ulrich, eds., John Wiley & Sons, Inc., New York, 1984, p. 100-125.
54. T. Kawaguchi, H. Hishikura, J. Iura, and Y. Kokubu, Monolithic Dried Gels and Silica Glass Prepared by the Sol-Gel Process, Journal of Non-Crystalline Solids, Vol. 63, 1984, p. 61-69.
55. S. P. Mukherjee, Sol-Gel Processes in Glass Science and Technology, Journal of Non-Crystalline Solids, Vol. 42, 1980, p. 477-488.
56. Iwao Matsuyama, Kenzo Susa, and Tsuneo Suganuma, Syntheses of High-Purity Silica Glass by the Sol-Gel Method, American Ceramic Society Bulletin, Vol. 63, No. 11, 1984, p. 1408-1411.
57. C. J. Brinker, E. P. Roth, D. R. Tallant, and G. W. Scherer, Relationships Between Sol to Gel to Glass Conversions: Structure of Gels During Densification, in Science of Ceramic Chemical Processing, L. L. Hench and D. R. Ulrich, eds., John Wiley & Sons, Inc., New York, 1986, p. 37-51.

58. Gerard OrceI, J. Phalippou, and L. L. Hench, Structural Changes of Silica Xerogels During Low Temperature Dehydration, *Journal of Non-Crystalline Solids*, Vol. 88, 1986, p. 114-130.
59. T. Izawa and S. Sudo, Optical Fibers: Materials and Fabrication, KTK Scientific Publishers, sold by Kluwer Academic Publishers, Norwell, Massachusetts, 1987, p. 33.
60. D. C. Havard and R. Wilson, Pore Measurements on the SCI/IUPAC/NPL Meso-Porous Silica Surface Area Standard, *Journal of Colloid and Interface Science*, Vol. 57, 1976, p. 276-288.
61. Clarence L. Babcock, Refractive Index and Dispersion, in Silicate Glass Technology Methods, John Wiley & Sons, Inc., New York, 1977, p. 87-114.
62. Du Pont Company, Du Pont 1090 Thermal Analysis System Manual, Du Pont Co., Wilmington, Delaware, 1983.
63. D. G. Holloway, The Physical Properties of Glass, Wykeham Publications Ltd., London, 1973, p. 143-149.
64. G. R. Anstis, P. Chantikul, B. R. Lawn, and D. B. Marshall, A Critical Evaluation of Indentation Techniques for Measuring Fracture Toughness: I and II, Direct Crack Measurements, *Journal of American Ceramic Society*, Vol. 64, 1981, p. 533-543.
65. Perkin-Elmer Company, Perkin-Elmer Lambda 9 UV/VIS/NIR Spectrometer Manual, Perkin-Elmer Co., West Germany, 1986.
66. Quantachrome Corporation, Autosorb-6 Manual, Quantachrome Corp., Syosset, New York, 1985.
67. E. P. Barrett, L. G. Joyner and P. P. Halenda, The Determination of Pore Volume and Area Distributions in Porous Substances, I: Computations from Nitrogen Isotherms, *Journal of the American Chemical Society*, Vol. 73, 1951, p. 373-380.
68. Jenkins and White, Fundamental of Optics, 3rd ed., McGraw-Hill, New York, 1957.
69. ASTM D790M-84, in Annual Book of ASTM Standards, 1986.
70. ASTM C158-80, in Annual Book of ASTM Standards, 1986.
71. D. B. Keck, R. D. Maurer and P. C. Schultz, On the Ultimate Low Limit of Attenuation in Glass Optical Waveguides, *Applied Physics Letters*, Vol. 22, 1973, p. 307-309.
72. G. H. Sigel, Ultraviolet Spectra of Silica Glasses: A Review of Some Experimental Evidence, *Journal of Non-Crystalline Solids*, Vol.13, 1973/1974, p. 378-398.

73. J. Phalippou, T. Woignier, and J. Zarzycki, Behavior of Monolithic Silica Aerogels at Temperatures Above 1000°C, in Ultrastructure Processing of Ceramics, Glasses and Composites, L. L. Hench and D. R. Ulrich, eds., John Wiley & Sons, Inc., New York, 1984, p. 70-87.
74. B. D. Cullity, Elements of X-Ray Diffraction, 2nd ed., Addison-Wesley Publishing Co., Inc., Reading, Massachusetts, 1978, p. 99-105.
75. C. A. Mulder, J. G. Van Lierop and G. Frens, Densification of SiO₂-Xerogels to Glass by Ostwald Ripening, *Journal of Non-Crystalline Solids*, Vol. 82, 1986, p. 92-96.
76. Dynasil Corporation of America, Catalog 302-M of Dynasil Synthetic Fused Silica, Dynasil Corp. of America, Berlin, New Jersey, 1987.
77. S. Palmqvist, Occurrence of Crack Formation During Vickers Indentation as a Measure of the Toughness of Hard Metals, *Arch. Eisenhüttenwes.*, Vol. 33, No. 6, 1962, p. 629-633.
78. F. Orgaz and H. Rawson, Characterization of Various Stages of the Sol-Gel Process, *Journal of Non-Crystalline Solids*, Vol. 82, 1986, p. 57-68.
79. J. B. Peri and A. L. Hensley, Jr., The Surface Structure of Silica Gel, *Journal of Physical Chemistry*, Vol. 72, [8], 1968, p. 2926-2933.
80. George H. Sigel, Jr., Interaction with Electromagnetic Radiation, in Treatise on Materials Science and Technology Volume 12-Glass I, Miknoru Tomozawa and Robert H. Doremus, eds., Academic Press, Inc., New York, 1977, p. 14.
81. M. Ali Omar, Elementary Solid State Physics, Addison-Wesley Publishing Co., Inc., Reading, Massachusetts, 1975, p. 86-133.
82. Allen H. Cherin, Fabrication of Optical Fibers, in An Introduction to Optical Fibers, McGraw-Hill Book Co., New York, 1983, p. 147-153.
83. Siemens, Fiber Optic Cables, John Wiley & Sons, Inc., New York, 1987, p. 32.
84. Michael L. Hair and William Hertl, Reactions of Chlorosilanes with Silica Surfaces, *Journal of Physical Chemistry*, Vol. 72, 1968, p. 2372-2378.
85. A. V. Kiselev and V. I. Lygin, Infrared Spectra of Surface Compounds, Keter Publishing House Jerusalem Ltd., John Wiley & Sons, Inc., New York, 1975.
86. L. R. Snyder and J. W. Ward, The Surface Structure of Porous Silicas, *Journal of Physical Chemistry*, Vol. 70, 1966, p. 3941-3952.
87. G. J. Young, Interaction of Water Vapor with Silica Surface, *Journal of Colloid Science*, Vol. 13, 1958, p. 67-85.
88. H. A. Benesi and A. C. Jones, An Infrared Study of the Water-Silica Gel System, *Journal of Physical Chemistry*, Vol. 63, 1957, p. 179-182.

89. J. A. Hockey and B. A. Pethica, Surface Hydration of Silicas, Transactions of Faraday Society, Vol. 57, 1961, p. 2247-2262.
90. A. V. Kiselev, Structure and Properties of Porous Materials, Colston Papers, Vol. 10, Butterworth, London, 1958, p. 195.
91. R. S. McDonald, Surface Functionality of Amorphous Silica by Infrared Spectroscopy, Journal of Physical Chemistry, Vol. 62, 1958, p. 1168-1178.
92. J. H. Anderson Jr. and K. A. Wickersheim, Near Infrared Characterization of Water and Hydroxyl Groups on Silica Surfaces, Surface Science, Vol. 2, 1964, p. 252-259.
93. J. B. Peri, Infrared Study of OH and NH₂ Groups on the Surface of a Dry Silica Aerogel, Journal of Physical Chemistry, Vol. 70, 1966, p. 2937-2945.
94. N. W. Cant and L. H. Little, The Infrared Spectrum of Ammonia Adsorbed on Cab-O-Sil Silica Powder, Canadian Journal of Chemistry, Vol. 43, 1965, p. 1252-1254.
95. N. W. Cant and L. H. Little, An Infrared Study of the Absorption of Ammonia on Porous Vycor Glass, Canadian Journal of Chemistry, Vol. 42, 1964, p. 802-809.
96. M. L. Hair and I. D. Chapman, Surface Composition of Porous Glass, Journal of the American Ceramic Society, Vol. 49, 1966, p. 651-654.
97. T. H. Elmer, I. D. Chapman and M. E. Nordberg, Changes in Length and Infrared Transmittance During Thermal Dehydration of Porous Glass at Temperatures Up to 1200°C, Journal of Physical Chemistry, Vol. 66, 1962, p. 1517-1519.
98. M. R. Basila, Hydrogen Bonding Interaction between Absorbate Molecules and Surface Hydroxyl Groups on Silica, Journal of chemical physics, Vol. 35, 1961, p. 1151-1158.
99. V. Y. Davydov, L. T. Zhuravlev and A. V. Kiselev, Study of the Surface and Bulk Hydroxyl Groups of Silica by Infrared Spectra and D₂O-Exchange, Transactions of Faraday Society, Vol. 60, 1964, p. 2254-2264.
100. Jurgen R. Meyer-Arendt, Introduction to Classical and Modern Optics, Prentice-Hall, Inc., New Jersey, 1984.
101. Ivan Fanderlik, Optical Properties of Glass. Glass Science and Technology 5, Elsevier, New York, 1983.
102. Kurt Nassau, Part II: Color Involving Vibrations and Simple Excitations, in The Physics and Chemistry of Color-The Fifteen Causes of Color, Wiley-Interscience Publication John Wiley & Sons, Inc., New York, 1983, p. 65-76.
103. G. William Tasker and William G. French, Low-Loss Optical Waveguides with Pure Fused SiO₂ Cores, IEEE, Vol. 62, 1974, p. 1281-1282.

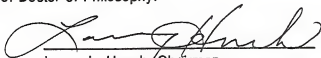
104. K. Susa, S. Satoh, I. Matsuyama, and T. Suganuma, New Optical Fiber Fabrication Method, Electron. Lett., Vol.18, No. 12, 1982, p. 499-500.
105. Table of Periodic Properties of the Elements, Sargent-Welch Scientific Co., Skokie, Illinois.
106. Kenzo Susa, Iwao Matsuyama, Shin Satoh and Tsuneo Suganuma, Reduction of Chlorine Content in Sol-Gel Derived Silica Glass, Journal of Non-Crystalline Solids, Vol.79, 1986, p. 165-176.
107. Handbook of Chemistry and Physics, 64th ed., CRC Press, Inc., Boca Raton, Florida, 1983-1984, p. B-135.
108. Neutron Activation Analysis of Trace Elements, Department of Nuclear Engineering North Carolina State University, Raleigh, North Carolina.
109. C.S. Vikram, D. K. Agrawal, R. Roy and H. A. McKinstry, A Simple Laser Speckle Dilatometer for Thermal Expansion Measurements, Material Letters, Vol. 3, No. 12, 1985, p. 482-484.
110. ASTM C-730, in Annual Book of ASTM Standards, 1976.
111. Naval Publications and Forms Center, Departments and Agencies of the Department of Defense, Military Specification, Glass, Optical, MIL-G-174, Amendment 2, Philadelphia, 25 June 1974.
112. A. Paul, Coloured Glasses, in Chemistry of Glasses, Chapman and Hall Ltd., New York, 1982, p. 204-270.
113. S. Hufner, Chapter 1, in Optical Spectra of Transparent Rare Earth Compounds, Academic Press, New York, 1978, p. 1-13.
114. L. E. Orgel, Introduction to Transition Metal Chemistry Ligand Field Theory, John Wiley & Sons, Inc., New York, 1960.
115. W. A. Weyl, Coloured Glasses, Society of Glass Technology, Sheffield, England 1951.
116. T. Bates, Ligand Field Theory and Absorption Spectra of Transition-Metal Ions in Glasses, in Modern Aspects of the Vitreous State, Vol. 2, J. D. Mackenzie ed., Butterworth, Inc., Washington DC, 1962, p. 195-254.
117. Foster L. Harding, The Development of Colors in Glass, Brockway Glass Co., Inc., Brockway, Pennsylvania.
118. F. A. Cotton and C. Wilkinson, Advanced Inorganic Chemistry, 4th ed., John Wiley & Sons, Inc., New York, 1980.
119. P. C. Schultz, Optical Absorption of the Transition Elements in Vitreous Silica, Journal of the American Ceramic Society, Vol. 57, July 1974, p. 309-313.
120. O. G. Holmes and D. S. McClure, Optical Spectra of Hydrated Ions of the Transition Metals, Journal of Chemical Physics, Vol. 26, 1957, p. 1686-1694.

BIOGRAPHICAL SKETCH

Shi-Ho Wang received a B. S. in mineral and petroleum engineering from the National Cheng Kung University, Tainan, Taiwan, in 1976. Upon graduation, he was required to serve the nation two years by law as a politics and science instructor lieutenant in Guantiarn Soldier Training Center, Army, Tainan, Taiwan. After serving in the Army, he was first employed as engineer and promoted to vice manager of the Engineering Department at Jong Mei Mineral Prospecting & Foundation Co., Taipei, Taiwan, in 1978. His duties involved quantitative analysis of mineral components and sampling design and engineering. Then he accepted a position as assistant engineer at the Department of Mines, Ministry of Economic Affairs, Taipei, Taiwan, in 1980 where his duties involved resolving the conflicts between domestic coke manufacturers and Japanese coke import agents, as well as issuing mining rights.

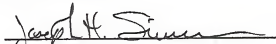
For seeking a higher education, he was admitted to the Materials Science and Engineering Department of University of Florida as a graduate student in the spring semester of 1982. With his advisor Dr. Hench's encouragement, he passed the doctoral qualifying examination in the Fall semester, 1985. One year later he was a consultant and later chief research and development scientist at GelTech Inc., Alachua, Florida. Since September 1987 he has devoted full time as a graduate associate to completing his doctoral degree in materials science and engineering.

I certify that I have read this study and that in my opinion it conforms to acceptable standards of scholarly presentation and is fully adequate, in scope and quality, as a dissertation for the degree of Doctor of Philosophy.



Larry L. Hench, Chairman
Graduate Research Professor of
Materials Science and Engineering

I certify that I have read this study and that in my opinion it conforms to acceptable standards of scholarly presentation and is fully adequate, in scope and quality, as a dissertation for the degree of Doctor of Philosophy.



Joseph H. Simmons
Professor of Materials Science
and Engineering

I certify that I have read this study and that in my opinion it conforms to acceptable standards of scholarly presentation and is fully adequate, in scope and quality, as a dissertation for the degree of Doctor of Philosophy.



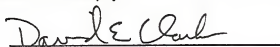
Vellayan Ramaswamy
Professor of Electrical Engineering

I certify that I have read this study and that in my opinion it conforms to acceptable standards of scholarly presentation and is fully adequate, in scope and quality, as a dissertation for the degree of Doctor of Philosophy.



Gholamreza J. Abbaschian
Professor of Materials
Science and Engineering

I certify that I have read this study and that in my opinion it conforms to acceptable standards of scholarly presentation and is fully adequate, in scope and quality, as a dissertation for the degree of Doctor of Philosophy.



David E. Clark
Professor of Materials
Science and Engineering

This dissertation was submitted to the Graduate Faculty of the College of Engineering and to the Graduate School and was accepted as partial fulfillment of the requirements for the degree of Doctor of Philosophy.

April 1988



Dean, College of Engineering

Dean, Graduate School

